

AFIT/GE/ENG/97D-12

EFFECTS OF NEAR-FIELD SCATTERERS
ON
SPACE-TIME ADAPTIVE PROCESSING

THESIS
Jonathan W. Fitton
Captain, USAF

AFIT/GE/ENG/97D-12

Approved for public release; distribution unlimited

19980128 101

DTIC QUALITY INSPECTED 3

The views expressed in this thesis are those of the author and do not reflect the official policy or position of the Department of Defense or the United States Government.

AFIT/GE/ENG/97D-12

EFFECTS OF NEAR-FIELD SCATTERERS
ON
SPACE-TIME ADAPTIVE PROCESSING

THESIS

Presented to the Faculty of the School of Engineering
of the Air Force Institute of Technology
Air University
In Partial Fulfillment of the
Requirements for the Degree of
Master of Science in Electrical Engineering

Jonathan W. Fitton, B.S.E.E.
Captain, USAF

December, 1997

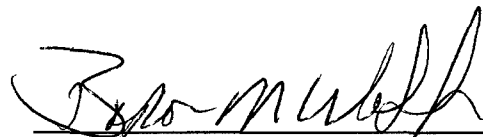
Approved for public release; distribution unlimited

EFFECTS OF NEAR-FIELD SCATTERERS
ON
SPACE-TIME ADAPTIVE PROCESSING

Jonathan W. Fitton, B.S.E.E.

Captain, USAF

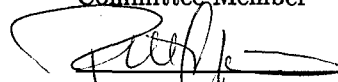
Approved:



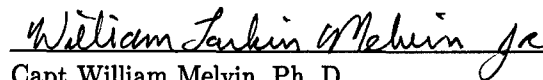
Dr. Byron Welsh
Thesis Advisor
Date 29 Oct 97



Maj Mike Temple, Ph. D.
Committee Member
Date 29 Oct 97



Capt Pete Collins, Ph. D.
Committee Member
Date 29 Oct 97



Capt William Melvin, Ph. D.
Committee Member
Date 29 OCT 97

Acknowledgements

I would like to thank my advisor, Dr. Byron Welsh, for introducing me to space-time adaptive processing and for his assistance in preparing this thesis. I would also like to thank my sponsor, Capt. Bill Melvin of Rome Labs, for suggesting this topic. I would like to thank my committee members, Maj. Pete Collins and Maj. Mike Temple, for their inputs in preparing this thesis. And finally, I would like to thank Maj. Scott Berger for helping me find the sign error in my derivation that had me going in circles for weeks.

Jonathan W. Fitton

Table of Contents

	Page
Acknowledgements	iii
List of Figures	vii
List of Tables	x
Abstract	xi
I. Introduction	1
II. Multidimensional Signal Processing	3
2.1 Introduction	3
2.2 Multidimensional Signals	3
2.3 Beamforming	5
2.3.1 Weighted Delay-and-Sum Beamformer	6
2.3.2 Filter-and-Sum Beamforming	11
2.3.3 Frequency-Domain Beamforming	13
2.4 Discrete Time Beamforming	14
2.5 Total Antenna Pattern	17
2.6 Summary	19
III. Space-Time Adaptive Processing	20
3.1 Introduction	20
3.2 Radar System	20
3.3 Target	23
3.4 Noise	28
3.5 Jamming	29

	Page
3.6 Clutter	31
3.6.1 Effects of Platform Motion on Clutter	34
3.6.2 Rank of the Clutter Covariance Matrix	36
3.6.3 Intrinsic Clutter Motion	40
3.7 Fully Adaptive Space-Time Adaptive Processing (STAP)	43
3.8 Signal-to-Interference-plus-Noise Ratio	46
3.9 Summary	46
IV. Near-Field Scatterers	49
4.1 Introduction	49
4.2 Radar System	52
4.3 Scattered Target Signal	54
4.4 Scattered Jammer Signal	57
4.5 Scattered Clutter Signal	59
4.6 Fully Adaptive Processing in the Presence of Near-field Scatterers	61
4.7 Summary	64
V. Results	69
5.1 Test Plan	69
5.2 Results	69
5.2.1 No External Interference	69
5.2.2 External Interference Present	86
VI. Conclusions	101
6.1 Conclusions	101
6.2 Suggestions for Future Research	102
Appendix A. Notational Conventions and Matrix Operations	103

	Page
Appendix B. Supplemental Figures	106
Bibliography	114
Vita	115

List of Figures

Figure		Page
1.	Loci of points in (\mathbf{k}, f)	5
2.	Bandpass filter in wavenumber-frequency space.	6
3.	Block diagram for the weighted delay-and-sum beamformer. .	6
4.	Lowpass Filtering of a misaligned signal.	9
5.	Array pattern for a 10 element linear array with no time delays.	10
6.	Effect of grating lobes in (\mathbf{k}, f) -space.	11
7.	Bandpass filter in wavenumber-frequency space.	15
8.	Quantized Steering Delays.	16
9.	Effect of steering delay quantization on array pattern.	17
10.	Radar system and antenna array geometries	21
11.	Radar CPI datacube	22
12.	Relationship between wavenumber vector, spatial frequency, wave- length, and element spacing.	24
13.	Clutter Geometry	31
14.	Clutter covariance matrix ($\beta = 1$), showing the Toeplitz-block- Toeplitz structure.	35
15.	Clutter ridges for different values of β	37
16.	Clutter ridges for different misalignment angles	38
17.	Clutter ridges for different combinations of ϕ_a and β	38
18.	Clutter eigenspectra.	39
19.	Effective array positions for successive pulses.	40
20.	Clutter eigenspectra different misalignment angles.	41
21.	The adapted pattern in the presence of interference	45
22.	Four possible scattering paths with a near-field scatterer . . .	50
23.	Geometry of the radar system including the near-field scatterer.	51

Figure		Page
24.	Location of the near-field scatterers relative to the array. . . .	61
25.	Clutter covariance matrix in the presence of seven near-field scatterers.	62
26.	Upper left corner of the clutter covariance matrix.	63
27.	The adapted pattern in the presence of interference and near-field scatterers	65
28.	Near-field scatterer orientations.	70
29.	SNR for 5 NFS, orientation A	71
30.	SNR for 7 NFS, orientation A	72
31.	SNR for 8 NFS, orientation A	73
32.	SNR for 15 NFS, orientation A	74
33.	Effect of eight NFS on the direct-path wavefront perceived by a fifteen element array.	75
34.	Signal-to-noise ratio for orientation A, no interference	77
35.	Signal-to-noise ratio for orientation B, no interference	78
36.	Signal-to-noise ratio for orientation C, no interference	79
37.	Signal-to-noise ratio for orientation D, no interference	80
38.	Signal-to-noise ratio for orientation E, no interference	81
39.	Signal-to-noise ratio for orientation F, no interference	82
40.	Adapted antenna pattern as a function of azimuth angle, $\phi_t = 0^\circ$.	83
41.	Adapted antenna pattern as a function of azimuth angle, $\phi_t = 20^\circ$	84
42.	Adapted antenna pattern as a function of azimuth angle, $\phi_t = 40^\circ$	85
43.	Eigenvalues of the clutter covariance matrix for different orientations.	87
44.	Adapted antenna pattern for orientation A, $\phi_t = 0^\circ$	89
45.	Adapted antenna pattern for orientation B, $\phi_t = 0^\circ$	90
46.	Adapted antenna pattern for orientation C, $\phi_t = 0^\circ$	91

Figure		Page
47.	Adapted antenna pattern for orientation D, $\phi_t = 0^\circ$	92
48.	Adapted antenna pattern for orientation E, $\phi_t = 0^\circ$	93
49.	Adapted antenna pattern for orientation F, $\phi_t = 0^\circ$	94
50.	SINR for orientation A, $\phi_t = 20^\circ$	95
51.	SINR for orientation B, $\phi_t = 20^\circ$	96
52.	SINR for orientation C, $\phi_t = 20^\circ$	97
53.	SINR for orientation D, $\phi_t = 20^\circ$	98
54.	SINR for orientation E, $\phi_t = 20^\circ$	99
55.	SINR for orientation F, $\phi_t = 20^\circ$	100
56.	Angle-Doppler pattern with no scatterers.	107
57.	Angle-Doppler pattern for orientation A.	108
58.	Angle-Doppler pattern for orientation B.	109
59.	Angle-Doppler pattern for orientation C.	110
60.	Angle-Doppler pattern for orientation D.	111
61.	Angle-Doppler pattern for orientation E.	112
62.	Angle-Doppler pattern for orientation F.	113

List of Tables

Table		Page
1.	Symbols for Radar System Parameters	27
2.	Parameters used to generate Fig. 21	44
3.	Symbols for near-field scatterer	53
4.	Definition of orientations	69
5.	Rank of the clutter covariance matrix for each orientation and number of scatterers S	86

Abstract

Near-field scatterers, such as the wing of an airplane, can affect the ability of the processor to null out clutter and jammer signals. Target, clutter and jammer signals will reflect off the near-field scatterers into the array and appear to be coming from a direction different from their true sources. In many analyses, it is assumed that the signals entering the array are plane waves. This assumption will not hold for the scattered signals, which will need to be treated as spherical waves, further complicating the computations.

This thesis develops a theoretical model similar to that in [8], but including the effects of near-field scatterers. The optimum weight vector, normally computed using the steering vector to the target and the covariance matrix of the undesired signals, must now include the effects of the scattered signals as well. This thesis shows that the space-time steering vector for the scattered signal can be written in a form similar to the direct path signal. The total space-time snapshot of a signal is the sum of the direct path and scattered path steering vectors associated with that signal.

The near-field scatterers cause more signal energy to enter the array than would be the case without the scatterers. When the scatterers are more than a half-wavelength apart, they create grating lobes in the adapted antenna pattern and a loss of signal-to-interference-plus-noise ratio (SINR). When the scatterers are less than a half wavelength apart, they tend to reduce the sidelobe level and increase the SINR. The rank of the clutter covariance matrix, which is an indicator of the number of degrees of freedom required to eliminate the clutter return, increases dramatically when near-field scatterers are present.

EFFECTS OF NEAR-FIELD SCATTERERS ON SPACE-TIME ADAPTIVE PROCESSING

I. Introduction

Space-time adaptive processing (STAP) is a technique to enhance the target detection capability of a radar array by adjusting the parameters of the array receivers to produce antenna pattern nulls in the direction of undesired signals, such as clutter and jamming, while placing the main lobe of the pattern in the direction of the target. The receiver parameters also control how different Doppler frequencies are processed. Because the characteristics of the target and undesired signals are unknown, they must be determined from the received signals. Then the receiver parameters are adjusted adaptively to form the desired beam pattern. This adaptive beamforming in the spatial and temporal domains is the essence of STAP.

The fundamentals of adaptive beamforming were first published by Applebaum [1] and Widrow [9]. In 1973, Brennan and Reed [5] published the first work describing optimal space-time filtering using adaptive arrays. At that time, the computational complexity of space-time adaptive processing was beyond the capability of the technology that existed to be implemented effectively. Advances in digital signal processing since that time, along with the development of new algorithms, have made implementation of STAP in real-time applications more feasible. In 1994, Ward [8] published a theoretical development of space-time adaptive processing. In his report, he presents models for each of the signals received by an airborne radar array and shows how they are processed using optimal, fully adaptive processing. He also presents several suboptimal processing methods.

Most works published on STAP assume the array is in free space. They do not account for the effect the airframe carrying the array has on the received signal. Specifically, how does a scatterer in the near-field of the array affect the received signal and the ability of the processor to null out interference. In [4], the authors show, through simulation, how a near-field scatterer can decrease target detectability by causing clutter returns at the same Doppler frequency as the target to appear to be coming from the same direction as the target. Others, such as Yu *et al.* [10], have developed computer simulations combining the geometrical theory of diffraction (GTD) with finite element modeling (FEM) to compute the pattern of an array mounted on a specific airframe. However, there has not been a theoretical development similar to Ward's which accounts for a near-field scatterer, and this development is the purpose of this thesis.

The next chapter develops the fundamentals of beamforming, following the development presented in [6]. Chapter 3 traces through Ward's development of fully adaptive space-time adaptive processing. Chapter 4 extends Ward's derivation to account for a near-field scatterer. Chapter 5 presents simulation results and Chapter 6 presents the conclusions of this thesis. Throughout this thesis, matrix notation is used to simplify expressions. Appendix A describes the notation and conventions used in this thesis.

II. Multidimensional Signal Processing

2.1 Introduction

The purpose of space-time adaptive processing (STAP) is to adjust an array so that an incoming desired signal can be detected while at the same time suppressing undesired signals from jammers, clutter and other sources. The first step in the development of space-time adaptive processing is an introduction to multidimensional signal processing and array beamforming. This chapter introduces the concepts of multidimensional signal processing and filtering in the wavenumber-frequency domain. It then develops expressions for different types of beamformers, and concludes with a discussion of the effect of digital implementation of these beamformers.

This chapter closely follows the development in Chapter 6 of [6].

2.2 Multidimensional Signals

A space-time signal can be described as a four-dimensional (4-D) function $s(\mathbf{x}, t)$, where \mathbf{x} is a three dimensional vector indicating position and t is time. This function can be analyzed as a four-dimensional Fourier transform. The function

$$S(\mathbf{k}, f) \triangleq \int_{-\infty}^{\infty} \int_{-\infty}^{\infty} s(\mathbf{x}, t) \exp[-j2\pi(ft - \mathbf{k}^T \mathbf{x})] d\mathbf{x} dt \quad (1)$$

is the wavenumber-frequency spectrum of the signal. The variable f is the temporal frequency of the signal, and \mathbf{k} is the wavenumber vector. The wavenumber vector represents the spatial frequency of the signal, or the number of wavelengths of the signal per unit distance in each of the three orthogonal spatial directions. The term $\mathbf{k}^T \mathbf{x}$ is the inner product of the wavenumber vector $\mathbf{k} \triangleq (k_x, k_y, k_z)^T$ and the position vector \mathbf{x} . The inverse transformation is defined as

$$s(\mathbf{x}, t) \triangleq \frac{1}{(2\pi)^2} \int_{-\infty}^{\infty} \int_{-\infty}^{\infty} S(\mathbf{k}, f) \exp[j2\pi(ft - \mathbf{k}^T \mathbf{x})] d\mathbf{k} df. \quad (2)$$

A propagating plane wave is represented by an elemental signal of the form

$$e(\mathbf{x}, t) \triangleq \exp[j2\pi(f_0 t - \mathbf{k}_0^T \mathbf{x})]. \quad (3)$$

An alternate way of writing Eqn. (3) is

$$e(\mathbf{x}, t) = \exp[j2\pi f_0(t - \boldsymbol{\alpha}_0^T \mathbf{x})], \quad (4)$$

where

$$\boldsymbol{\alpha}_0 \triangleq \frac{\mathbf{k}_0}{f_0}. \quad (5)$$

From this definition, it can be seen that $e(\mathbf{x}, t)$ represents a plane wave propagating in the direction $\boldsymbol{\alpha}_0$ with a speed equal to $1/|\boldsymbol{\alpha}_0|$. The vector $\boldsymbol{\alpha}_0$ is referred to as the *slowness vector* because its magnitude is equal to the inverse of the propagation speed. The slowness vector is a convenient way to describe both the frequency and direction of propagation of a signal.

Taking the Fourier transform of (4) produces

$$E(\mathbf{k}, f) = \delta(\mathbf{k} - \mathbf{k}_0)\delta(f - f_0) \quad (6)$$

which represents a four-dimensional impulse function in (\mathbf{k}, f) -space at the point $\mathbf{k}=\mathbf{k}_0$ and $f = f_0$. Thus, every point in (\mathbf{k}, f) -space corresponds to a plane wave in (\mathbf{x}, t) -space with a particular orientation and frequency. In Fig. 1, various loci of points are shown for three dimensions (k_x, k_y, f) . (The k_z component is omitted to simplify the figures.) Figure 1(a) shows that all signals with the same frequency lie in a plane normal to the f axis. All signals coming from the same direction will lie in a half-plane normal to the (k_x, k_y) plane, as shown in Fig. 1(b). Figure 1(c) represents all signals with the same propagation speed. These signals lie on a cone given by $|\mathbf{k}| = f/c$. Generally, it will be assumed the speed of propagation is a constant equal to c , the speed of light in free space.

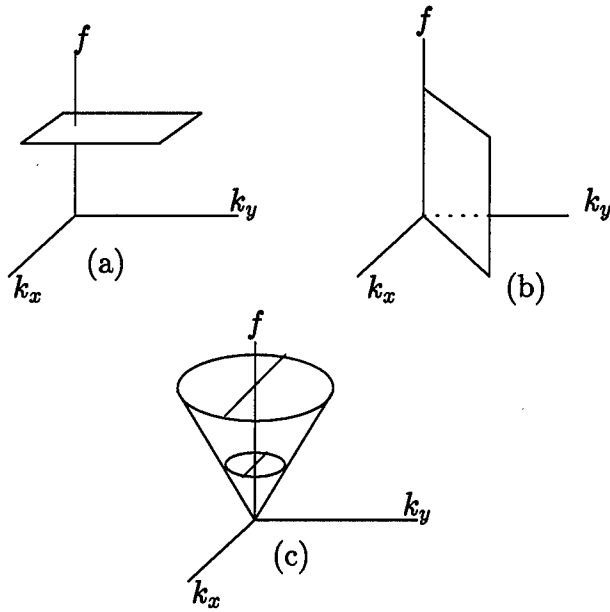


Figure 1 Loci of points occupied in (\mathbf{k}, f) -space by plane waves with the same (a) frequency f , (b) direction of propagation \mathbf{k} , and (c) velocity of propagation $1/|\alpha_0|$.

Given a signal $s(\mathbf{x}, t)$, the response $f(\mathbf{x}, t)$ of a linear, shift-invariant filter $h(\mathbf{x}, t)$ is given by the 4-D convolution integral

$$f(\mathbf{x}, t) = \int_{-\infty}^{\infty} \int_{-\infty}^{\infty} h(\mathbf{x} - \boldsymbol{\xi}, t - \tau) s(\boldsymbol{\xi}, \tau), d\boldsymbol{\xi} d\tau. \quad (7)$$

Transforming this expression to the wavenumber-frequency domain produces

$$F(\mathbf{k}, f) = H(\mathbf{k}, f)S(\mathbf{k}, f). \quad (8)$$

The task is to design the filter $H(\mathbf{k}, f)$ such that it passes signals from the desired regions of (\mathbf{k}, f) -space while eliminating signals from other regions.

2.3 Beamforming

Figure 2 shows how a 3-D bandpass filter might be represented. Signals with frequencies in the range of Δf and directions of arrival within the range of angles

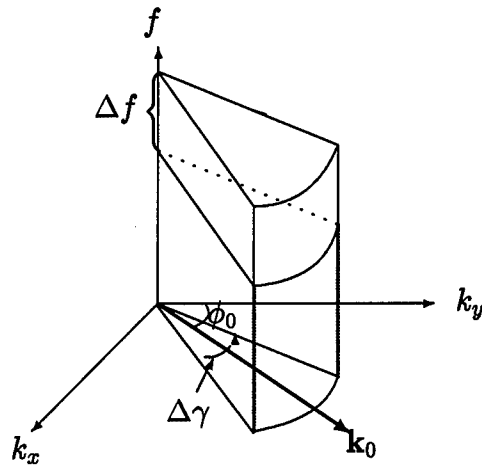


Figure 2 Bandpass filter in wavenumber-frequency space.

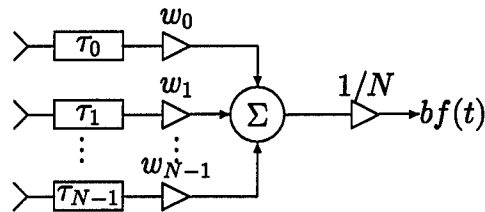


Figure 3 Block diagram for the weighted delay-and-sum beamformer.

$\Delta\gamma$ would be allowed to pass through the filter; all other signals would be filtered out. The process by which this is accomplished is called *beamforming*. To achieve this effect, an array of N elements is arranged in space such that the n th element is located at $\mathbf{x}_n (n = 0, 1, \dots, N - 1)$. Since the relative position of the elements is fixed, they sample the signal $s(\mathbf{x}, t)$ spatially. The signal from the n th receiver will be given by $r_n(t) = s(\mathbf{x}_n, t)$, and these signals can be processed by various methods in either the time or frequency domain.

2.3.1 Weighted Delay-and-Sum Beamformer. The weighted delay-and-sum beamformer of Fig. 3 is one of the simplest beamforming systems. The output $bf(t)$ is the average of the weighted and delayed receiver signals

$$bf(t) \triangleq \frac{1}{N} \sum_{n=0}^{N-1} w_n r_n(t - \tau_n), \quad (9)$$

where $r_n(t)$ is the signal received by the n th receiver w_n and τ_n are respectively the weight and relative delay of the n th receiver. Adjusting the delays τ_n has the effect of “steering” the center of the beamformer’s passband to the desired orientation in (\mathbf{k}, f) -space. The receiver outputs due to a signal from the desired direction will be added together in phase, while receiver outputs due to signals from other directions will be out of phase and will tend to cancel each other out. To pass plane waves with a slowness vector $\boldsymbol{\alpha}_0$, the delays should be set equal to

$$\tau_n = -\boldsymbol{\alpha}_0^T \mathbf{x}_n. \quad (10)$$

Suppose a plane wave $s(\mathbf{x}, t)$ has a slowness vector $\boldsymbol{\alpha}$ such that $s(\mathbf{x}, t) = \exp[j2\pi f(t - \boldsymbol{\alpha}^T \mathbf{x})]$. When the beam is steered towards $\boldsymbol{\alpha}_0$, the output from the beamformer due to $s(\mathbf{x}, t)$ is given by the following:

$$\begin{aligned} bf(t) &= \frac{1}{N} \sum_{n=0}^{N-1} w_n r_n(t - \tau_n) \\ &= \frac{1}{N} \sum_{n=0}^{N-1} w_n s(\mathbf{x}_n, t + \boldsymbol{\alpha}_0^T \mathbf{x}_n) \\ &= \frac{1}{N} \sum_{n=0}^{N-1} w_n \exp[j2\pi f(t + \boldsymbol{\alpha}_0^T \mathbf{x}_n - \boldsymbol{\alpha}^T \mathbf{x}_n)] \\ &= \left(\frac{1}{N} \sum_{n=0}^{N-1} w_n \exp[-j2\pi f(\boldsymbol{\alpha} - \boldsymbol{\alpha}_0)^T \mathbf{x}_n] \right) \exp(j2\pi ft) \\ &= W(f(\boldsymbol{\alpha} - \boldsymbol{\alpha}_0)) \exp(j2\pi ft) \\ &= W(\mathbf{k} - \mathbf{k}_0) \exp(j2\pi ft), \end{aligned} \quad (11)$$

where

$$W(\mathbf{k}) \triangleq \frac{1}{N} \sum_{n=0}^{N-1} w_n \exp(-j2\pi \mathbf{k}^T \mathbf{x}_n) \quad (12)$$

is called the *array pattern*. The array pattern indicates how a signal with a wavenumber vector $\mathbf{k} = f\boldsymbol{\alpha}$ will be attenuated when the beam is steered in the direction of $\boldsymbol{\alpha}_0$. Using the expression for $s(\mathbf{x}, t)$ from Eqn. (2) and the definition of the array pattern from Eqn. (12), the beamformer output can be written as

$$bf(t) = \frac{1}{N} \int_{-\infty}^{\infty} \int_{-\infty}^{\infty} S(\mathbf{k}, f) W(\mathbf{k} - f\boldsymbol{\alpha}_0) \exp(j2\pi ft) d\mathbf{k} df. \quad (13)$$

This equation gives the wideband response of the weighted delay-and-sum beamformer and shows how signals from different directions and at different frequencies are attenuated before being combined to produce the beamformer output.

As a special case, consider a waveform $v(t)$, which may be a single signal or combination of signals propagating in the same direction. Then $s(\mathbf{x}, t)$ can be written as

$$s(\mathbf{x}, t) = v(t - \boldsymbol{\alpha}^T \mathbf{x}) \quad (14)$$

and its wavenumber-frequency spectrum is given by

$$S(\mathbf{k}, f) = V(f) \delta(\mathbf{k} - f\boldsymbol{\alpha}), \quad (15)$$

where $V(f)$ is the Fourier transform of $v(t)$ and $\delta(\mathbf{k})$ is the 3-D impulse function. Then Eqn. (13) becomes

$$bf(t) = \int_{-\infty}^{\infty} V(f) W(f(\boldsymbol{\alpha} - \boldsymbol{\alpha}_0)) \exp(j2\pi ft) df. \quad (16)$$

If the direction of propagation of $v(t)$ coincides with the direction to which the beamformer is being steered, then $\boldsymbol{\alpha} = \boldsymbol{\alpha}_0$ and the signal waveform will not be attenuated.

If $\boldsymbol{\alpha} \neq \boldsymbol{\alpha}_0$, the term $f(\boldsymbol{\alpha} - \boldsymbol{\alpha}_0)$ grows linearly with frequency, causing the higher-frequency components to be attenuated more than lower-frequency components. This effect can be seen in Fig. 4. Signals from the \mathbf{k}_0 direction will be passed

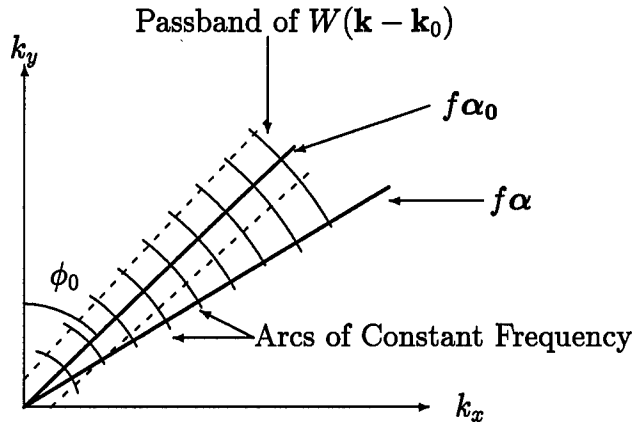


Figure 4 Lowpass Filtering of a misaligned signal.

unattenuated at all frequencies, while signals originating from other directions will have their high-frequency components filtered out.

It is possible to interpret Eqn. (13) as a 4-D filtering operation. Applying the convolution theorem to Eqn. (7) yields

$$f(\mathbf{x}, t) = \frac{1}{(2\pi)^2} \int_{-\infty}^{\infty} \int_{-\infty}^{\infty} H(\mathbf{k}, f) S(\mathbf{k}, f) \exp[j2\pi(ft - \mathbf{k}^T \mathbf{x})] d\mathbf{k} df. \quad (17)$$

Equation (13) is equivalent to Eqn. (17) evaluated at $\mathbf{k} = \mathbf{0}$. Therefore, the wavenumber-frequency response is given by

$$H(\mathbf{k}, f) = W(\mathbf{k} - f\boldsymbol{\alpha}_0). \quad (18)$$

Evaluating the array pattern evaluated at $\mathbf{k} - f\boldsymbol{\alpha}_0$ will produce the complex amplitude of the response of the filter used to process the space-time signal $s(\mathbf{x}, t)$.

The simplest type of antenna array consists of N identical receiver elements arranged in a line with equal spacing d between elements. This configuration is called a *uniform linear array*. For now, equal weights $w_n = 1$ will be assumed for each element. If the array is oriented along the x -axis, the position of the n th element is given by $\mathbf{x}_n = (nd, 0, 0)$ ($n = 0, 1, \dots, N - 1$) and the expression for the

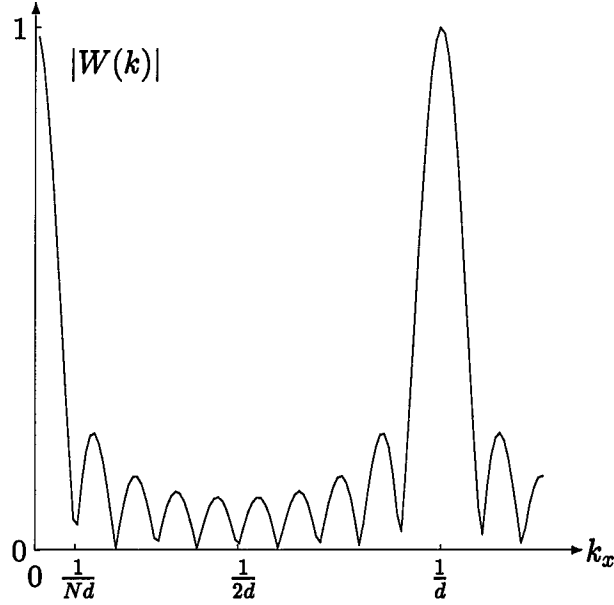


Figure 5 Array pattern for a 10 element linear array with no time delays.

array pattern in Eqn. (12) becomes

$$\begin{aligned}
 W(\mathbf{k}) &= \frac{1}{N} \sum_{n=0}^{N-1} \exp[-j2\pi \mathbf{k}^T \mathbf{x}_n] \\
 &= \frac{1}{N} \sum_{n=0}^{N-1} \exp[-j2\pi k_x n d] \\
 &= \frac{1}{N} \sum_{n=0}^{N-1} (\exp[-j2\pi k_x d])^n \\
 &= \frac{1}{N} \frac{1 - \exp[-j2\pi N k_x d]}{1 - \exp[-j2\pi k_x d]} \\
 &= \frac{1}{N} \frac{\exp[j\pi N k_x d] - \exp[-j\pi N k_x d]}{\exp[j\pi k_x d] - \exp[-j\pi k_x d]} \frac{\exp[-j\pi N k_x d]}{\exp[-j\pi k_x d]} \\
 &= \frac{\sin(\pi N k_x d)}{N \sin(\pi k_x d)} \exp[-j\pi(N-1)k_x d], \tag{19}
 \end{aligned}$$

where $k_x = |\mathbf{k}| \sin(\phi_0) = \sin(\phi_0)/\lambda$ and ϕ_0 is as shown in Fig. 4. The magnitude of this array pattern is shown in Fig. 5 for $N = 10$. The pattern repeats with period $k_x = 1/d$. The repeated main lobes are called *grating lobes*. These grating lobes can allow signals to enter the beamformer from directions and frequencies other than those for which the beamformer is designed. This effect is illustrated in Fig. 6.

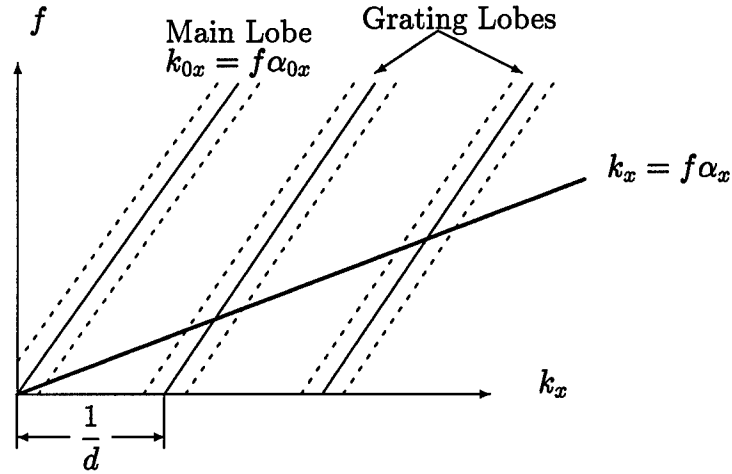


Figure 6 Effect of grating lobes in (k, f) -space. Components of k_x which lie within the grating lobes will enter the beamformer unattenuated.

A signal with a wavenumber vector $k_{0x} = f\alpha_{0x}$ will lie entirely within the main lobe. A signal with wavenumber vector $k_x = f\alpha$ will cross the grating lobes, and components of this signal which lie within the main lobe or grating lobes will enter the beamformer unattenuated. The existence of grating lobes indicates the spatial sampling interval d is too large in relation to the wavelengths of the incoming signals. This effect is equivalent to the aliasing which results when time varying signals are not sampled at a high enough rate. To avoid aliasing when sampling time varying signals, the sample rate must be at least twice the maximum frequency contained in the signal. Similarly, to avoid the spatial frequency aliasing which results in grating lobes, the interelement distance d must meet the criterion

$$d \leq \frac{\lambda_{\min}}{2}, \quad (20)$$

where λ_{\min} is the minimum wavelength in the received signal.

2.3.2 Filter-and-Sum Beamforming. The weighted delay-and-sum beamformer discussed above can be extended to allow the receiver weights to be a function of frequency, so that signal components at different frequencies are weighted differ-

ently. Then, at a specific frequency, Eqn. (9) can be rewritten as

$$bf(t, f) = \frac{1}{N} \sum_{n=0}^{N-1} W_n(f) r_n(t - \tau_n), \quad (21)$$

where $r_n(t)$ is the inverse Fourier transform of the signal spectrum incident on the n th receiver,

$$r_n(t) = \int_{-\infty}^{\infty} R_n(f) \exp(j2\pi ft) df. \quad (22)$$

For a single frequency $f = f_0$, Eqn. (22) reduces to

$$r_n(t) = R_n(f_0) \exp(j2\pi f_0 t), \quad (23)$$

and Eqn. (21) can be rewritten as

$$bf(t, f_0) = \frac{1}{N} \sum_{n=0}^{N-1} W_n(f_0) R_n(f_0) \exp[j2\pi f_0(t - \tau_n)]. \quad (24)$$

Integrating this expression over all frequencies gives the filter-and-sum beamformer output

$$\begin{aligned} fs(t) &\triangleq \int_{-\infty}^{\infty} bf(t, f) df \\ &= \frac{1}{N} \sum_{n=0}^{N-1} \int_{-\infty}^{\infty} W_n(f) R_n(f) \exp[j2\pi f(t - \tau_n)] df. \end{aligned} \quad (25)$$

To simplify the notation, define the signal

$$q_n(t) \triangleq \int_{-\infty}^{\infty} W_n(f) R_n(f) \exp[j2\pi ft] df. \quad (26)$$

Then Eqn. (25) can be written as

$$fs(t) = \frac{1}{N} \sum_{n=0}^{N-1} q_n(t - \tau_n). \quad (27)$$

From Eqn. (26), it can be seen that $q_n(t)$ is the convolution of $w_n(t)$ with $r_n(t)$, where $w_n(t)$ is the inverse Fourier transform of the weighing function $W_n(f)$. The function $w_n(t)$ can be viewed as the impulse response of a filter that operates on the receiver signal $r_n(t)$. The filtered signal $q_n(t)$ which results is then used to shape the beam.

2.3.3 Frequency-Domain Beamforming. It is possible to write expressions for the outputs of the weighted delay-and-sum and filter-and-sum beamformers in the frequency domain by computing their Fourier transform as follows

$$BF(f) = \frac{1}{N} \sum_{n=0}^{N-1} w_n R_n(f) \exp(-j2\pi f \tau_n) \quad (28)$$

$$FS(f) = \frac{1}{N} \sum_{n=0}^{N-1} W_n(f) R_n(f) \exp(-j2\pi f \tau_n). \quad (29)$$

The output of each beamformer at a specific frequency f is obtained by multiplying the above expressions by $\exp(j2\pi ft)$, and the complete beamformer output is obtained by integrating over all frequencies

$$bf(t) = \int_{-\infty}^{\infty} BF(f) \exp(j2\pi ft) df \quad (30)$$

$$fs(t) = \int_{-\infty}^{\infty} FS(f) \exp(j2\pi ft) df. \quad (31)$$

Since computing the signal spectrum $R_n(f)$ in Eqns. (28) and (29) would require integrating the signal over all time, it is necessary to approximate the spectrum by computing the Fourier transform of a segment of the time signal. This is done by applying a finite-extent window to the signal

$$\hat{R}_n(t, f) \triangleq \int_{-\infty}^{\infty} p_T(t - \tau) r_n(\tau) \exp(-j2\pi f \tau) d\tau, \quad (32)$$

where $p_T(t - \tau)$ is the window function centered at time τ with width T .

Using this definition in Eqn. (28) gives the frequency-domain beamformer output of the weighted delay-and-sum beamformer as

$$fd(t, f) \triangleq \frac{1}{N} \sum_{n=0}^{N-1} w_n \hat{R}_n(t, f) \exp[j2\pi f(t - \tau_n)]. \quad (33)$$

Integrating this expression over all frequencies will give an approximation to the beamformer output signal. A similar expression results if Eqn. (29) is used.

Using Eqns. (1), (10), (12) and defining

$$r_n(t) \triangleq s(\mathbf{x}_n, t) \quad (34)$$

$$P(f) \triangleq \int_{-\infty}^{\infty} p_T(t) \exp(-j2\pi ft) dt, \quad (35)$$

it is possible to write the frequency domain beamformer output as

$$fd(t, f) = \frac{1}{(2\pi)^2} \int_{-\infty}^{\infty} \int_{-\infty}^{\infty} W(\mathbf{k} - f\boldsymbol{\alpha}_0) P(\theta - f) S(\mathbf{k}, \theta) \exp(j\theta t) d\mathbf{k} d\theta. \quad (36)$$

If the array pattern $W(\mathbf{k} - f\boldsymbol{\alpha}_0)$ is considered to be zero except near $\mathbf{k} = f\boldsymbol{\alpha}_0$ and the window spectrum $P(\theta - f)$ is considered to be zero except near $\theta = f$, the factor $W(\mathbf{k} - f\boldsymbol{\alpha}_0)P(\theta - f)$ will represent the passband of the system. The beamformer will attenuate all signals in (\mathbf{k}, θ) -space except those near $\mathbf{k} = f\boldsymbol{\alpha}_0$ and $\theta = f$. The passband is illustrated in Fig. 7.

2.4 Discrete Time Beamforming

Until this point, all signals have been treated as continuous time signals. However, most beamformers are implemented digitally, requiring the received signals to be sampled in time. In this section, the effects of using discrete time signals will be examined. The same notation will be used as with the continuous time case, but now the variable t will represent an integer multiple k of the sampling period T , such

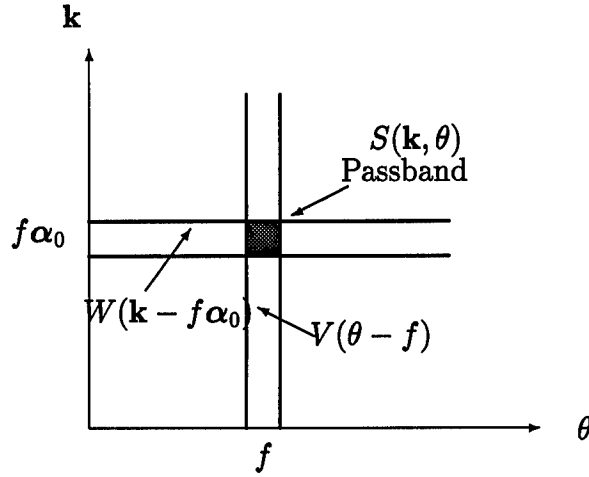


Figure 7 Bandpass filter in wavenumber-frequency space. The shaded region represents the passband.

that $t = kT$. Thus, $r_n(t)$ will denote a discrete-time signal. It is assumed that the sampling rate is high enough to avoid aliasing.

The discrete-time version of the weighted delay-and-sum beamformer is given by

$$bf(kT) = \frac{1}{N} \sum_{n=0}^{N-1} w_n r_n(kT - k_n T), \quad (37)$$

where $k_n T$ is the quantized steering delay for the n th sensor. Since k_n is an integer, the quantized steering delays will generally not be equal to the ideal delay τ_n . The quantization error in the n th delay is given by

$$\Delta\tau_n = k_n T - \tau_n. \quad (38)$$

This error must be accounted for in the response of the beamformer to a plane wave with slowness vector α_0 . The new expression is

$$H(\mathbf{k}, f) = \frac{1}{N} \sum_{n=0}^{N-1} w_n \exp[-j2\pi(\mathbf{k} - f\alpha_0)^T \mathbf{x}_n] \exp(-j2\pi f t \Delta\tau_n). \quad (39)$$

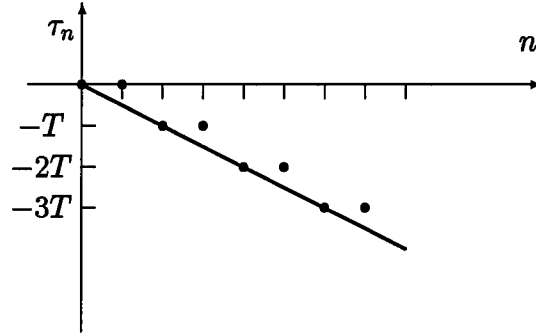


Figure 8 Quantized Steering Delays. Dots indicate the quantized steering delays, the line indicates the ideal delay.

As a simple example to illustrate the effect of quantizing error, consider a uniform linear array oriented along the x -axis. If the beam is steered such that $\alpha_{0x} = T/2d$, then the ideal delay is $\tau_n = -nT/2$. However, the delay applied must be an integer multiple of the sample period. Therefore, the actual delay will be $k_n T$, where k_n is the largest integer less than or equal to $n/2$. The quantized steering error will be

$$\Delta\tau_n = \begin{cases} \frac{T}{2} & \text{for } n \text{ odd} \\ 0 & \text{for } n \text{ even} \end{cases} \quad (40)$$

as shown in Fig. 8. For this case, the frequency response can be written as

$$\begin{aligned} H(\mathbf{k}, f) &= \frac{1}{N} \sum_{n=0}^{N/2-1} \exp \left[-j2\pi \left(k_x - \frac{fT}{2d} \right) 2nd \right] \\ &\quad + \frac{1}{N} \sum_{n=0}^{N/2-1} \exp \left[-j2\pi \left(k_x - \frac{fT}{2d} \right) (2n+1)d - j2\pi \frac{fT}{2} \right] \\ &= \left\{ \frac{1}{N} \sum_{n=0}^{N/2-1} \exp[-j2\pi n(2k_x d - ft)] \right\} [1 + \exp(-j2\pi k_x d)] \\ &= H_1(\mathbf{k}, f) H_2(\mathbf{k}, f), \end{aligned} \quad (41)$$

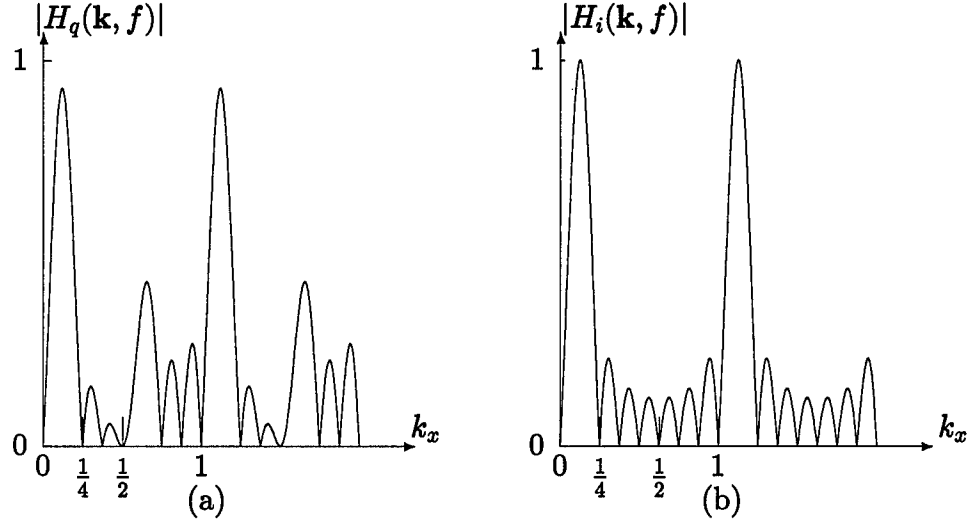


Figure 9 Effect of steering delay quantization on array pattern: $N = 8$, $d = 1$, $T = 1$, $f = 1/4$. (a) Quantized beamformer [Eqn. (41)], (b) Ideal beamformer [Eqn. (19)].

where

$$\begin{aligned}
 H_1(\mathbf{k}, f) &= \frac{2}{N} \sum_{n=0}^{N/2-1} \exp[-j2\pi n(2k_x d - ft)] \\
 &= \frac{\sin[(\pi N)(k_x d - fT/2)]}{(\pi N) \sin(k_x d - fT/2)} \exp \left[-j2\pi \left(\frac{N}{2} - 1 \right) \left(k_x d - \frac{fT}{2} \right) \right] \quad (42)
 \end{aligned}$$

$$\begin{aligned}
 H_2(\mathbf{k}, f) &= \frac{1}{2} [1 + \exp(-j2\pi k_x d)] \\
 &= \exp(-j\pi k_x d) \cos(\pi k_x d). \quad (43)
 \end{aligned}$$

An example of the magnitude $|H(\mathbf{k}, f)|$ is shown in Fig. 9 for both the quantized and ideal cases. For the quantized case, the main lobe peak is lower and some of the side lobes are higher than for the ideal case. The ideal response is given by $|H_i(\mathbf{k}, f)| = |W(k_x d - fT/2)|$, where $W(\mathbf{k})$ is as defined in Eqn. (19).

2.5 Total Antenna Pattern

To compute the total antenna pattern for a given array, the array pattern computed using Eqn. (19) must be multiplied by the element pattern. For a small dipole, the element pattern will be a cosine function, with the angle measured from

the normal to the element. Substituting $k_x = \sin(\phi)/\lambda$ into the equation for the array pattern in Eqn. (19) and multiplying by the element pattern, the magnitude of total antenna voltage pattern can be computed as a function of angle as

$$AP_v(\phi) = \frac{\sin(\pi Nd \sin(\phi)/\lambda)}{N \sin(\pi d \sin(\phi)/\lambda)} \cos(\phi). \quad (44)$$

The antenna power pattern is found by squaring Eqn. (44),

$$AP_p(\phi) = \left[\frac{\sin(\pi Nd \sin(\phi)/\lambda)}{N \sin(\pi d \sin(\phi)/\lambda)} \cos(\phi) \right]^2. \quad (45)$$

The gain of the array is equal to the inverse of the average radiation intensity. The radiation intensity of the array is given by [2:276-278]

$$U(\phi) = [AF_v]^2 = \left[\frac{\sin(\pi Nd \sin(\phi)/\lambda)}{N \sin(\pi d \sin(\phi)/\lambda)} \right]^2. \quad (46)$$

The average radiation intensity of the array, U_0 , is given by

$$U_0 = \frac{1}{2} \int_{-\pi/2}^{\pi/2} \left[\frac{\sin(\pi Nd \sin(\phi)/\lambda)}{N \sin(\pi d \sin(\phi)/\lambda)} \right]^2 \cos(\phi) d\phi. \quad (47)$$

By letting $\psi = 2\pi d \sin(\phi)/\lambda$, the average radiation intensity can be expressed as

$$U_0 = \frac{1}{2\pi} \int_{-\pi}^{\pi} \left[\frac{\sin(N\psi/2)}{N \sin(\psi/2)} \right]^2 d\psi, \quad (48)$$

and the array gain $G_a(\phi) = 1/U_0$. If the spacing between array elements is equal to a half wavelength, the array gain is approximately equal to the number of elements. To find the total antenna transmit gain, $G_t(\phi)$, the array gain is multiplied by the element gain, $g(\phi)$.

2.6 Summary

This chapter has presented some of the fundamentals of beamforming with a linear array. Expressions were derived for the weighted delay-and-sum beamformer and the filter-and-sum beamformer in both the time and frequency domains. The effects of quantization error introduced by a digital implementation of a weighted delay-and-sum beamformer were also examined. Finally, an expression for the gain of a linear array was presented. The next chapter presents a theoretical development of space-time adaptive processing, which is an extension of the beamforming techniques presented in this chapter. It will be assumed there is no quantization error.

III. Space-Time Adaptive Processing

3.1 Introduction

Now that we have the basics of multidimensional signal processing, we will begin studying the signals in more detail to understand how they are composed and how they can be analyzed. In this chapter, models are developed for the radar system and signals from the target, jammers, and clutter. The chapter concludes with a discussion of fully adaptive STAP. This discussion closely follows that in [8].

3.2 Radar System

The system being analyzed is assumed to be mounted on an airborne platform and utilizing a pulsed Doppler waveform. The platform is at a height h_a and traveling with a constant velocity, \mathbf{v}_a . The variables ϕ and θ are the azimuth and elevation angles measured with respect to the normal to the array. The unit vector $\hat{\mathbf{k}}$ indicates the direction to the point of interest and may be represented in Cartesian coordinates as

$$\hat{\mathbf{k}}(\phi, \theta) = \cos(\theta) \sin(\phi) \hat{\mathbf{x}} + \cos(\theta) \cos(\phi) \hat{\mathbf{y}} + \sin(\theta) \hat{\mathbf{z}}. \quad (49)$$

Figure 10 depicts the scenario. The antenna is assumed to be a uniform linear array of N identical elements separated by a distance d and oriented along the x -axis. The vector $\mathbf{d} = d\hat{\mathbf{x}}$ will be used to represent the array spacing and orientation. Each element has the same radiation voltage pattern $f(\phi, \theta)$ and power pattern $g(\phi, \theta) = |f(\phi, \theta)|^2$. The radar transmits a coherent burst of M pulses on a carrier frequency $f_0 = c/\lambda_0$ and at a constant pulse repetition frequency (PRF), $f_r = 1/T_r$, where T_r is the pulse repetition interval (PRI). The time interval over which the waveform returns are collected is equal to MT_r and is called the *coherent processing interval* (CPI).

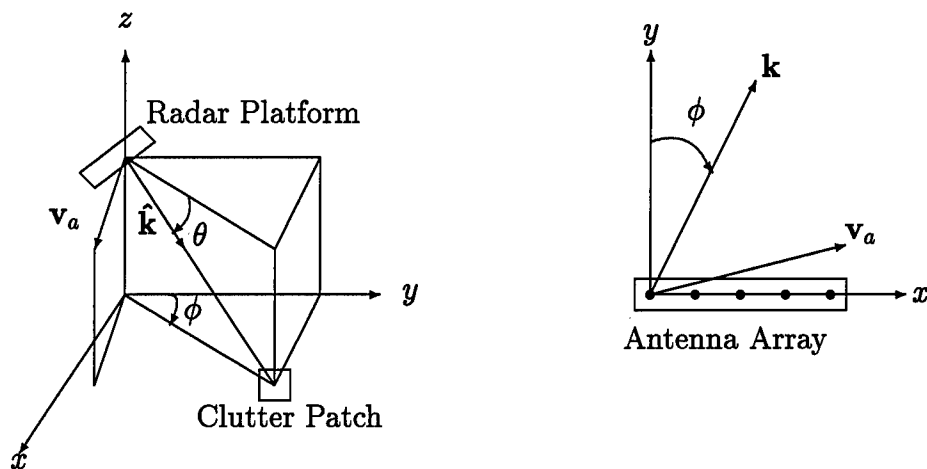


Figure 10 Radar system and antenna array geometries

The radar array has a transmit pattern $G_t(\phi, \theta)$ which is determined by the number and spacing of the elements. Each element is connected to its own receiver, consisting of a down-converter, matched filter, and A/D converter. The receiver bandwidth B is taken to be equal to the transmitted pulse bandwidth. The output from each element's A/D converter is sent to the processor, where the total signal is analyzed. For each PRI, L time samples are collected to cover the range interval of interest. If the array has N receivers and transmits M pulses, the received data during a single CPI will consist of LMN complex samples. The data can be conveniently represented as a $L \times M \times N$ cube of complex samples referred to as the *CPI datacube*, as illustrated in Fig. 11.

For the l th range gate, $\mathbf{x}_{m,l}$ is an $N \times 1$ vector of all the receiver element outputs for the m th pulse. This vector is called a spatial snapshot. The matrix \mathbf{X}_l is an $N \times M$ matrix consisting of the spatial snapshots from all pulses. By stacking the columns of \mathbf{X}_l on top of each other, this matrix is reshaped into an $MN \times 1$ vector $\boldsymbol{\chi}_l = \text{vec}(\mathbf{X}_l)$ called the *space-time snapshot*. The remainder of the analysis will assume the returns from only one range gate are being studied, and the l subscript will be dropped. Therefore, $\boldsymbol{\chi}$ will be the space-time snapshot at the

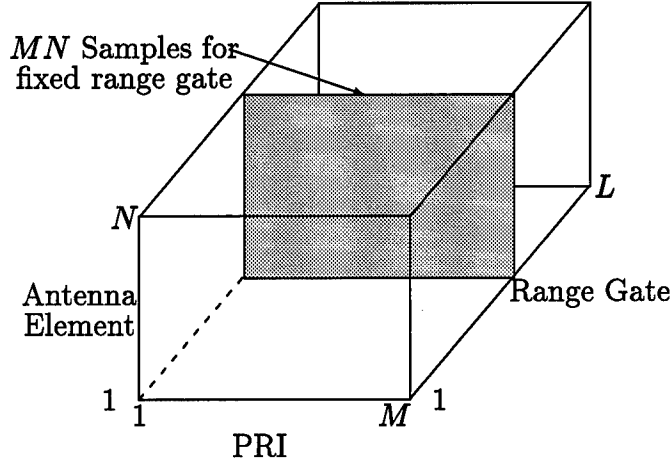


Figure 11 Radar CPI datacube

range of interest, and \mathbf{x}_m will represent the spatial snapshot from the m th PRI at this range.

The space-time snapshot has two components, the target return and the undesired signal,

$$\mathbf{x} = \mathbf{x}_t + \mathbf{x}_u = \alpha_t \mathbf{v}_t + \mathbf{x}_u, \quad (50)$$

where α_t is the complex amplitude of the target return, \mathbf{v}_t is the system response to a target of unit amplitude, and $\mathbf{x}_u = \mathbf{x}_c + \mathbf{x}_j + \mathbf{x}_n$ represents undesired signals, due to clutter return, jamming and noise. If no target is present, $\alpha_t = 0$ and the space-time snapshot consists entirely of the undesired signals. The presence of a target causes a shift in the mean of the data, but does not affect the covariance of the data. Assuming the clutter, jamming and noise signals to be mutually uncorrelated, the covariance matrix of the total undesired signal is the sum of the covariance matrices of each component:

$$\begin{aligned} \mathbf{R}_u = E[\mathbf{x}_u \mathbf{x}_u^H] &= E[(\mathbf{x}_c + \mathbf{x}_j + \mathbf{x}_n)(\mathbf{x}_c + \mathbf{x}_j + \mathbf{x}_n)^H] \\ &= E[\mathbf{x}_c \mathbf{x}_c^H] + E[\mathbf{x}_j \mathbf{x}_j^H] + E[\mathbf{x}_n \mathbf{x}_n^H] \\ &= \mathbf{R}_c + \mathbf{R}_j + \mathbf{R}_n, \end{aligned} \quad (51)$$

where the subscripts c , j , and n indicate clutter, jammer, and noise interference respectively. The following sections develop a model for each component of the space-time snapshot.

3.3 Target

The return from a target at a given range, R_t , is a function of the target's azimuth angle, ϕ , depression angle, θ , closing velocity with respect to the radar, v_t , and radar cross-section (RCS), σ_t . The received signal can be derived by defining the transmitted signal and applying the filtering that produces the samples of the space-time snapshot. The transmitted coherent burst of pulses from the array is represented by

$$\tilde{s}(t) = a_t u(t) e^{j2\pi f_0 t} e^{j\psi}, \quad (52)$$

where

$$u(t) = \sum_{m=0}^{M-1} u_p(t - mT_r) \quad (53)$$

is the complex envelope of the signal, T_r is the PRI, and $u_p(t)$ is the complex envelope of a single pulse of width T_p and having unit energy. The transmitted signal has amplitude a_t and a random phase ψ . The signal received from the target by the n th element is given by

$$\tilde{s}_n(t) = a_r u(t - \tau_n) \exp[j2\pi(f_0 + f_t)(t - \tau_n)] e^{j\psi}, \quad (54)$$

where a_r is the amplitude of the returned signal and $f_t = 2v_t/\lambda_0$ is the target Doppler frequency. The target delay to the n th element has two components: $\tau_n = \tau_t + \tau'_n$, where $\tau_t = 2R_t/c$ is the time for the signal to travel from the array to the target and back, and

$$\tau'_n = -\frac{n\hat{\mathbf{k}}(\phi_t, \theta_t) \cdot \mathbf{d}_n}{c} = -n\frac{d}{c} \cos \theta_t \sin \phi_t \quad (55)$$

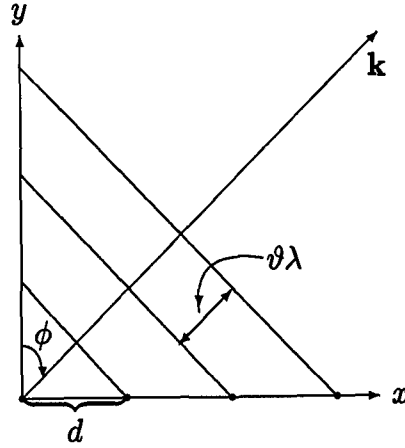


Figure 12 Illustration of relationship between wavenumber vector \mathbf{k} , spatial frequency ϑ , wavelength λ , and element spacing d .

is the relative delay measured from the phase reference to the n th element. The target *spatial frequency* will be defined as

$$\vartheta_t = \frac{\hat{\mathbf{k}}(\phi_t, \theta_t) \cdot \mathbf{d}}{\lambda_0} = \frac{d}{\lambda_0} \cos \theta_t \sin \phi_t. \quad (56)$$

Figure 12 shows how the spatial frequency relates to the wavelength, array spacing, and wavenumber vector. The phase delay to the n th element can now be given by $-\omega_0 \tau'_n = n2\pi\vartheta_t$. Assuming a narrowband transmitted waveform, the relative delay term τ'_n in the envelope $u(t - \tau_n)$ of Eqn. (54) is insignificant. The received signal can be expressed as

$$\begin{aligned} \tilde{s}_n(t) &= a_r u(t - \tau_t) e^{j\psi} \exp[j2\pi(f_0 t + f_t t - f_0 \tau_n - f_t \tau_n)] \\ &= a_r u(t - \tau_t) e^{j\psi} \exp[j2\pi(f_0 t + f_t t - f_0 \tau_t - f_0 \tau'_n - f_t \tau_t - f_t \tau'_n)] \\ &= a_r u(t - \tau_t) e^{j\psi} e^{(jn2\pi\vartheta_t)} e^{(j2\pi f_t t)} e^{(j2\pi f_0 t)}, \end{aligned} \quad (57)$$

where ψ now contains several of the fixed frequency terms. The signal is downconverted to baseband, removing the carrier frequency term, and then passed through a matched filter with a response given by $h(t) = u_p^*(-t)$. The output of the matched

filter for the n th channel is found from the convolution of the signal with the filter,

$$\begin{aligned}
x_n(t) &= \tilde{s}_n(t) * h(t) \\
&= \int_{-\infty}^{\infty} a_r u(\beta - \tau_t) e^{j\psi} e^{jn2\pi\vartheta_t} e^{j2\pi f_t \beta} u_p^*(\beta - t) d\beta \\
&= a_r e^{j\psi} e^{jn2\pi\vartheta_t} \int_{-\infty}^{\infty} \sum_{m=0}^{M-1} u_p(\beta - \tau_t - mT_r) u_p^*(\beta - t) e^{j2\pi f_t \beta} d\beta. \quad (58)
\end{aligned}$$

Letting $\gamma = \beta - \tau_t - mT_r$ and interchanging the integration and summation operations gives

$$\begin{aligned}
x_n(t) &= a_r e^{j\psi} e^{jn2\pi\vartheta_t} \sum_{m=0}^{M-1} \int_{-\infty}^{\infty} u_p(\gamma) u_p(\gamma - t + \tau_t + mT_r) e^{j2\pi f_t (\gamma + \tau_t + mT_r)} d\gamma \\
&= a_r e^{j\psi} e^{jn2\pi\vartheta_t} e^{j2\pi f_t \tau_t} \sum_{m=0}^{M-1} e^{jm2\pi f_t T_r} \int_{-\infty}^{\infty} u_p(\gamma) u_p^*(\gamma - t + \tau_t + mT_r) e^{jw\pi f_t \gamma} d\gamma. \quad (59)
\end{aligned}$$

The term $e^{j2\pi f_t \tau_t}$ represents a fixed frequency and can be absorbed into the random phase term. The integral can be recognized as the ambiguity function [7:411-412],

$$\chi(\tau, f) = \int_{-\infty}^{\infty} u_p(\gamma) u_p^*(\gamma - \tau) e^{j2\pi f \gamma} d\gamma. \quad (60)$$

At this time it will be convenient to normalize the target Doppler frequency to the PRF. The *normalized Doppler frequency* is defined as

$$\varpi_t = \frac{f_t}{f_r} = f_t T_r. \quad (61)$$

With these two definitions, Eqn. (59) can be written as

$$x_n(t) = a_r e^{j\psi} e^{jn2\pi\vartheta_t} \sum_{m=0}^{M-1} e^{jm2\pi\varpi_t} \chi(t - \tau_t - mT_r, f_t). \quad (62)$$

For the range gate containing the target, $t_m = \tau_t + mT_r$ ($m = 0, 1, \dots, M - 1$) represents the sample times from each PRI at this range gate. The target samples are given by

$$x_{mn} = x_n(t_m) = a_r e^{j\psi} e^{jn2\pi\vartheta_t} e^{jm2\pi\omega_t} \chi(0, f_t). \quad (63)$$

Because the pulse waveform is normalized, $\chi(0, 0) = 1$. It is also assumed the pulse waveform is insensitive to the target Doppler, such that $\chi(0, f) \approx 1$. Therefore, Eqn. (63) can be written as

$$x_{mn} = \alpha_t e^{jn2\pi\vartheta_t} e^{jm2\pi\omega_t}, \quad \begin{array}{l} n=0, 1, \dots, N-1 \\ m=0, 1, \dots, M-1 \end{array}, \quad (64)$$

where $\alpha_t = a_r e^{j\psi}$ is the complex random amplitude of the signal. The target amplitude can be calculated from the radar range equation as follows. The single pulse signal-to-noise ratio (SNR) for a single element is given by

$$\xi_t = \frac{P_t T_p G_t(\theta_t, \phi_t) g(\theta_t, \phi_t) \lambda_0^2 \sigma_t}{(4\pi)^3 N_0 L_s R_t^4}, \quad (65)$$

where the terms are as defined in Table 1. The target power is computed from

$$E \{ |\alpha_t|^2 \} = \sigma_n^2 \xi_t, \quad (66)$$

where σ_n^2 is the thermal noise power per element. The target amplitude is then given by $a_r = \sqrt{\sigma_n^2 \xi_t}$.

At this time, it will be convenient to define the spatial and temporal steering vectors. The *spatial steering vector* is an $N \times 1$ vector given by

$$\mathbf{a}(\phi, \theta) = [1; e^{j2\pi \frac{d}{\lambda} \cos \theta \sin \phi}; \dots; e^{j(N-1)2\pi \frac{d}{\lambda} \cos \theta \sin \phi}], \quad (67)$$

Table 1 Symbols for Radar System Parameters

N	number of elements in array
M	number of pulses in CPI
L	number of range samples per PRI
f_0	radar operating frequency
λ_0	radar operating wavelength
d	interelement spacing
T_r	pulse repetition interval (PRI)
f_r	pulse repetition frequency (PRF)
P_t	peak transmit power
T_p	transmit pulse width
B	instantaneous bandwidth
$G_t(\theta, \phi)$	full array transmit power gain
$f(\theta, \phi)$	element pattern (voltage)
$g(\theta, \phi)$	element pattern (power)
L_r	system losses on receive
L_t	system losses on transmit
L_s	total system losses
N_0	receiver noise power spectral density
R_t	target range
σ_t	target RCS
h_a	platform height
v_a	platform velocity

or

$$\mathbf{a}(\vartheta) = [1; e^{j2\pi\vartheta}; \dots; e^{j(N-1)2\pi\vartheta}], \quad (68)$$

The *temporal steering vector* $\mathbf{b}(\varpi)$ is an $M \times 1$ vector given by

$$\mathbf{b}(\varpi) = [1; e^{j2\pi\varpi}; \dots; e^{j(M-1)2\pi\varpi}], \quad (69)$$

where ϑ and ϖ are as defined in Eqns. (56) and (61). The $MN \times 1$ *space-time steering vector* will be defined as

$$\mathbf{v} = \mathbf{v}(\vartheta, \varpi) = \mathbf{b}(\varpi) \otimes \mathbf{a}(\vartheta), \quad (70)$$

where (\otimes) indicates the Kronecker product. With these conventions, the space-time snapshot of the target data can be written as

$$\chi_t = \alpha_t \mathbf{b}(\varpi_t) \otimes \mathbf{a}(\vartheta_t) = \alpha_t \mathbf{b}_t \otimes \mathbf{a}_t = \alpha_t \mathbf{v}_t, \quad (71)$$

which is the target component of the total space-time snapshot of Eqn. (50). The space-time steering vector of the target \mathbf{v}_t is also referred to as the *target steering vector*.

3.4 Noise

Noise is be present in each of the receiver elements. Since each element has its own receiver, it is assumed the noise processes on each of the N element will be mutually uncorrelated. It is also be assumed that the M noise samples on a given element separated by a nonzero multiple of the PRI are temporally uncorrelated. These two assumptions may be expressed as

$$E \{ x_{n_1, m} x_{n_2, m}^* \} = \sigma_n^2 \delta_{n_1 - n_2} \quad (72)$$

$$E \{ x_{n, m_1} x_{n, m_2}^* \} = \sigma_n^2 \delta_{m_1 - m_2}, \quad (73)$$

where $\sigma_n^2 = N_0 B$ is the noise power per element and δ_m is the Kronecker delta function defined as

$$\delta_m = \begin{cases} 1 & , \quad m = 0 \\ 0 & , \quad m \neq 0 \end{cases} . \quad (74)$$

The noise component of the space-time covariance matrix can then be expressed as

$$\mathbf{R}_n = E \{ \boldsymbol{\chi}_n \boldsymbol{\chi}_n^H \} = \sigma_n^2 \mathbf{I}_M \otimes \mathbf{I}_N = \sigma_n^2 \mathbf{I}_{MN} . \quad (75)$$

The noise power will be normalized to $\sigma_n^2 = 1$ so that all signal levels can be referenced by their SNR per element and pulse.

3.5 Jamming

For this analysis, only barrage noise jamming from a source at a long range and an angle different from that of the target will be considered. The jammer bandwidth will be assumed to be much larger than the pulse bandwidth, and the radar PRF will be assumed to be much smaller than the instantaneous bandwidth. The jammer signal will be correlated spatially across the array, but temporally uncorrelated from pulse to pulse. Therefore, the jammer signal will appear like thermal noise in the time domain, but as a point source in the spatial domain.

For a jammer at range R_j , elevation θ_j , and azimuth ϕ_j with effective radiated power density S_j , the jammer power spectral density J_0 received by one element is given by

$$J_0 = \frac{S_j g(\theta_j, \phi_j) \lambda_0^2}{(4\pi)^2 R_j^2 L_r} . \quad (76)$$

The jammer-to-noise ratio (JNR) at the element is given by $\xi_j = J_0/N_0$. The jammer space-time snapshot is given by

$$\boldsymbol{\chi}_j = \boldsymbol{\alpha}_j \otimes \mathbf{a}_j, \quad (77)$$

where α_j is a $M \times 1$ vector of the random jammer amplitudes during each PRI and $\mathbf{a}_j = \mathbf{a}(\phi_j, \theta_j)$ is the jammer steering vector. Assuming the jamming signal is stationary over a CPI, the jammer space-time covariance matrix can be calculated as

$$\begin{aligned}
\mathbf{R}_j &= E \{ \chi_j \chi_j^H \} = E \{ (\alpha_j \otimes \mathbf{a}_j)(\alpha_j \otimes \mathbf{a}_j)^H \} \\
&= E \{ (\alpha_j \otimes \mathbf{a}_j)(\alpha_j^H \otimes \mathbf{a}_j^H) \} \\
&= E \{ (\alpha_j \alpha_j^H) \otimes (\mathbf{a}_j \mathbf{a}_j^H) \} \\
&= \sigma_n^2 \xi_j \mathbf{I}_M \otimes (\mathbf{a}_j \mathbf{a}_j^H) \\
&= \mathbf{I}_M \otimes (\sigma_n^2 \xi_j \mathbf{a}_j \mathbf{a}_j^H) \\
&= \mathbf{I}_M \otimes \Phi_j,
\end{aligned} \tag{78}$$

where Φ_j is the jammer spatial covariance matrix.

This result can be generalized to multiple jamming sources. If there are J jammer sources, the spatial covariance matrix is given by

$$\Phi_j = \mathbf{A}_j \Xi_j \mathbf{A}_j^H, \tag{79}$$

where

$$\mathbf{A}_j = [\mathbf{a}(\theta_1 \phi_1), \mathbf{a}(\theta_2 \phi_2), \dots, \mathbf{a}(\theta_J \phi_J)] \tag{80}$$

is the $N \times J$ jammer spatial steering matrix. If the jammer waveforms are mutually uncorrelated, the jammer source covariance matrix Ξ_j will be a $J \times J$ diagonal matrix of the jammer powers, From Eqn. (78) it can be seen that the jammer space-time covariance matrix will be block diagonal, with each non-zero block consisting of the jammer spatial covariance matrix. If the J jammer steering vectors are linearly independent and no two jamming signals are perfectly coherent, then the rank of Φ_j will be equal to J , and \mathbf{R}_j will have rank MJ .

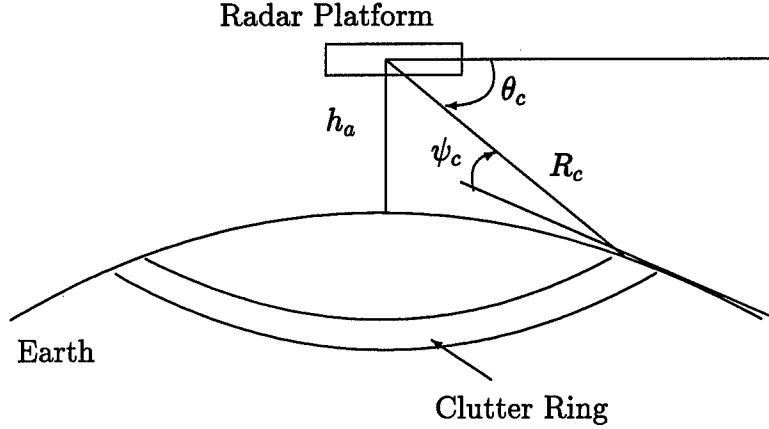


Figure 13 Clutter Geometry

3.6 Clutter

Clutter is defined as the radar return from the ground. It is the most complicated source of interference because it is distributed in angle, range, and Doppler. It exists over all azimuth angles and all elevation angles below the horizon. The clutter range returns extend from the platform altitude to the radar horizon, and the Doppler returns cover a range of frequencies corresponding to $-v_a$ to $+v_a$.

Figure 13 depicts a clutter ring at a range R_c . A $4/3$ effective radius is assumed to model the curvature of the earth, so the effective earth radius $a_e = (4/3)r_e$. The elevation angle to the clutter ring is given by

$$\theta_c = \theta_c(R_c) = -\sin^{-1} \left(\frac{R_c^2 + h_a(h_a + 2a_e)}{2R_c(a_e + h_a)} \right) \approx -\sin^{-1} \left(\frac{R_c}{2a_e} + \frac{h_a}{R_c} \right) \quad (81)$$

and the grazing angle is given by

$$\psi_c = \psi_c(R_c) = -\sin^{-1} \left(\frac{R_c^2 - h_a(h_a + 2a_e)}{2R_c a_e} \right) \approx -\sin^{-1} \left(\frac{R_c}{2a_e} - \frac{h_a}{R_c} \right). \quad (82)$$

The grazing angle is the angle between the vector from the antenna to the clutter patch and the tangent at the clutter patch.

The radar horizon range is given by $R_h = \sqrt{2a_e h_a + h_a^2}$ and the radar's unambiguous range is given by $R_u = c/2f_r$. If $R_u > R_h$, the clutter will be unambiguous in range and the return in the l th range gate will contain clutter from at most one range. If $R_u < R_h$, the clutter will be range ambiguous and some or all of the range gates will contain clutter returns from multiple ranges. At this time, the assumption will be made that the clutter is unambiguous in range, and that the clutter return in a particular range gate is from a single clutter ring. The clutter return will be modeled as the superposition of N_c independent clutter sources evenly distributed in azimuth.

The location of a particular clutter patch will be described by its azimuth angle ϕ_k and its range R_c (or elevation angle θ_c). The spatial frequency for the k th clutter patch is given by

$$\vartheta_k = \frac{\hat{\mathbf{k}}^T(\theta_c, \phi_k)\mathbf{d}}{\lambda_0} = \frac{d}{\lambda_0} \cos \theta_c \sin \phi_k \quad (83)$$

and the normalized Doppler frequency is represented by ϖ_k . The clutter component of the space-time snapshot is given by

$$\chi_c = \sum_{k=1}^{N_c} \alpha_k \mathbf{v}_k = \sum_{k=1}^{N_c} \alpha_k \mathbf{b}_k \otimes \mathbf{a}_k, \quad (84)$$

where α_k is the complex random amplitude from the k th clutter patch and $\mathbf{v}_k = \mathbf{v}(\vartheta_k, \varpi_k)$ is the space-time steering vector to the k th clutter patch, as defined in Eqn. (70).

Each clutter patch represents an effective area bounded by the radar's resolution in azimuth, $\Delta\phi = 2\pi/N_c$, and range, $\Delta R = c/2B$. The effective RCS of a clutter patch at range R_c is given by

$$\sigma_k = \sigma_0(\theta_c, \phi_k) \times \text{PatchArea} = \sigma_0(\theta_c, \phi_k) R_c \Delta\phi \Delta R \sec \psi_c, \quad (85)$$

where σ_0 is the area reflectivity of the ground at the k th clutter patch. It will be assumed that the reflectivity at a given range is uniform in azimuth, so $\sigma_0 = \gamma \sin \psi_c$, where γ depends on the terrain. With these definitions, the clutter-to-noise ratio (CNR) is defined as

$$\xi_k = \frac{P_t T_p G_t(\theta_c, \phi_k) g(\theta_c, \phi_k) \lambda_0^2 \sigma_k}{(4\pi)^3 N_0 L_s R_c^4}. \quad (86)$$

The amplitude of the clutter from the k th clutter patch is given by $E\{|\alpha_k|^2\} = \sigma_n^2 \xi_k$. If the returns from different clutter patches are uncorrelated, then

$$E[\alpha_k \alpha_l^*] = \sigma_n^2 \xi_k \delta_{k-l}. \quad (87)$$

Using Eqns. (84) and (87), the space-time covariance matrix for the clutter is given by

$$\begin{aligned} \mathbf{R}_c &= E[\boldsymbol{\chi}_c \boldsymbol{\chi}_c^H] = \sigma_n^2 \sum_{k=1}^{N_c} \xi_k \mathbf{v}_k \mathbf{v}_k^H \\ &= \sigma_n^2 \sum_{k=1}^{N_c} \xi_k \mathbf{b}_k \mathbf{b}_k^H \otimes \mathbf{a}_k \mathbf{a}_k^H, \end{aligned} \quad (88)$$

where $\mathbf{b}_k = \mathbf{b}(\varpi_k)$ and $\mathbf{a}_k = \mathbf{a}(\vartheta_k)$. The clutter spatial and temporal covariance matrices are coupled because the clutter Doppler is a function of angle. The clutter space-time covariance matrix can also be expressed as a product of matrices:

$$\mathbf{R}_c = \mathbf{V}_c \boldsymbol{\Xi}_c \mathbf{V}_c^H, \quad (89)$$

where $\mathbf{V}_c = [\mathbf{v}_1, \mathbf{v}_2, \dots, \mathbf{v}_{N_c}]$ is an $MN \times N_c$ matrix of the clutter space-time steering vectors, and

$$\boldsymbol{\Xi}_c = \sigma_n^2 \text{diag}[\xi_1, \xi_2, \dots, \xi_{N_c}] \quad (90)$$

contains the clutter power distributions. Due to the assumptions of an ideal uniform linear array and mutually uncorrelated clutter patches, the clutter space-time covariance matrix has a special structure referred to as Toeplitz-block-Toeplitz. This

structure can be seen in Fig. 14. All blocks along a diagonal are identical, and within each block, all elements along a diagonal are equal. The blocks correspond to the M pulses, and the elements within each block correspond to the N antenna elements.

3.6.1 Effects of Platform Motion on Clutter. The above derivation assumed the array was stationary while the data was being collected. When the array is moving, as it would be on an airborne platform, the clutter develops a special structure due to the dependence of the Doppler frequency on angle. Assume the platform is moving such that the velocity vector of the array is given by $\mathbf{v}_a = v_a(\cos \phi_a \hat{\mathbf{x}} + \sin \phi_a \hat{\mathbf{y}})$, where ϕ_a is the *misalignment angle* between the velocity vector of the array and the array axis, as shown in Fig. 10. This may occur when the aircraft is "crabbing" to compensate for a crosswind. The clutter Doppler frequency of a specific clutter patch is then given by

$$f_k(\theta_c, \phi_k + \phi_a) = \frac{2v_a}{\lambda_0} \cos \theta_c \sin(\phi_k + \phi_a). \quad (91)$$

The clutter spatial frequency and normalized Doppler will be, respectively,

$$\vartheta_k = \eta \sin \phi_k \quad (92)$$

$$\varpi_k = \beta \eta \sin(\phi_k + \phi_a) \quad (93)$$

where $\beta = 2v_a T_r / d$ and $\eta = d \cos \theta_c / \lambda_0$.

Equations (92) and (93) can be shown to satisfy the standard equation of an ellipse in (ϑ, ϖ) -space,

$$\beta^2 \vartheta_c^2 - (2\beta \cos \phi_a) \vartheta_c \varpi_c + \varpi_c^2 - \beta^2 \eta^2 \sin^2 \phi_a = 0. \quad (94)$$

The elliptical shape of the clutter results from returns entering the receiver through the back lobe of the antenna. The ellipse will be rotated clockwise from the positive

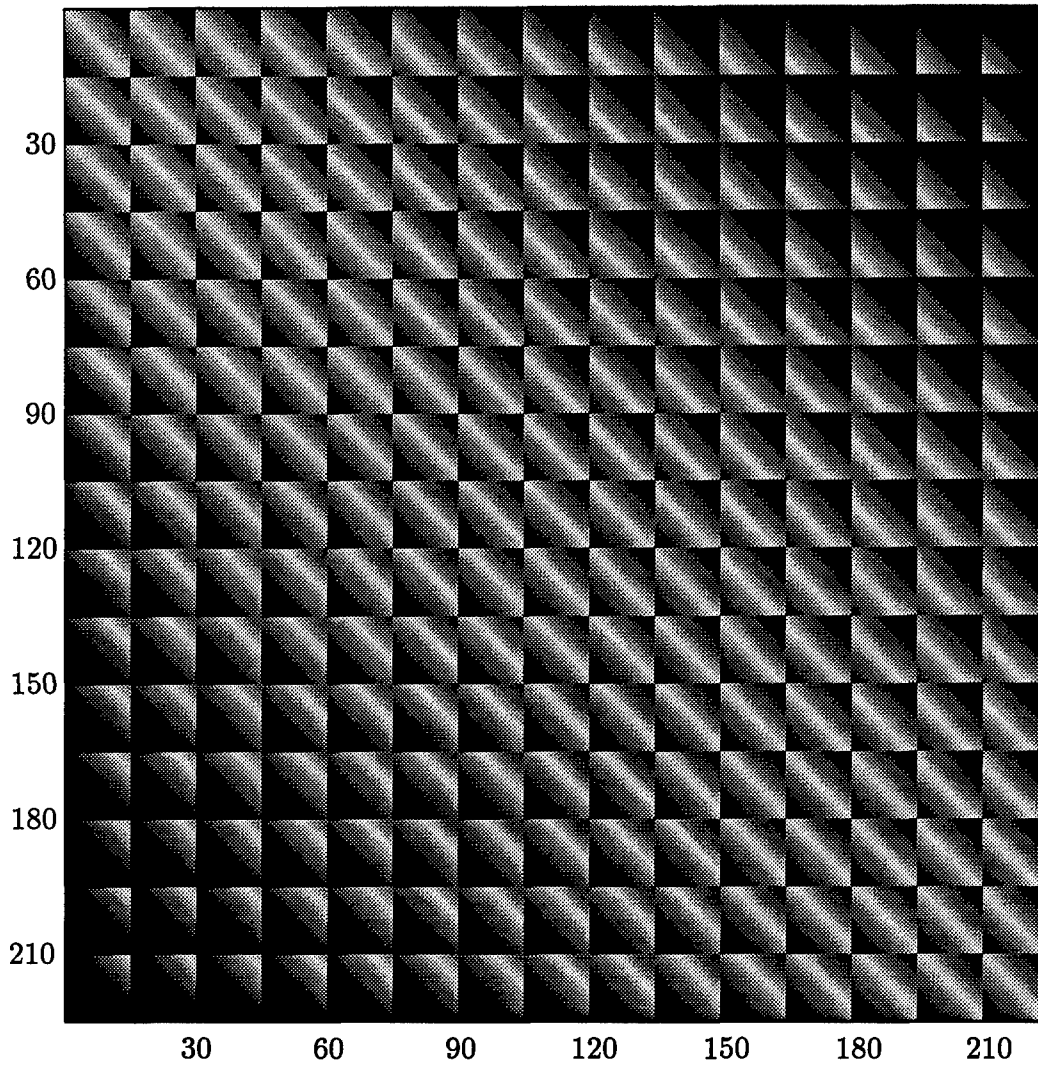


Figure 14 Clutter covariance matrix ($\beta = 1$), showing the Toeplitz-block-Toeplitz structure.

ϖ -axis by an angle ψ_a such that [8]

$$\cot 2\psi_a = \frac{1 - \beta^2}{2\beta \cos \phi_a} \quad (95)$$

and will have semimajor and semiminor axes given respectively by

$$a = \beta\eta \sin \phi_a \left(\frac{1}{2}(\beta^2 + 1) + |c| \right)^{-1/2} \quad (96)$$

$$b = \beta\eta \sin \phi_a \left(\frac{1}{2}(\beta^2 + 1) - |c| \right)^{-1/2}, \quad (97)$$

where c is given by

$$c = \frac{1}{2}(\beta^2 - 1) \cos 2\psi_a - \beta \cos \phi_a \sin 2\psi_a. \quad (98)$$

In the case where the velocity vector of the platform is aligned with the axis of the array, $\phi_a = 0$, and Eqn. (94) reduces to the equation of a line of clutter.

$$\varpi_c = \beta\vartheta_c. \quad (99)$$

The back lobe return is still present, but directly overlays the front lobe return. When $\beta < 1$, there will be a range of normalized Doppler frequencies which will be free from clutter return. For values of $\beta > 1$, the clutter return will be ambiguous in Doppler. Figures 15 through 17 show the plots of the clutter ridges for various values of β and different misalignment angles ϕ_a as functions of the spatial frequency and normalized Doppler frequency.

3.6.2 Rank of the Clutter Covariance Matrix. The severity of the clutter scenario and the number of degrees of freedom needed to effectively cancel the clutter are indicated by the rank of the clutter covariance matrix. The rank, r_c , can be estimated from Brennan's rule:

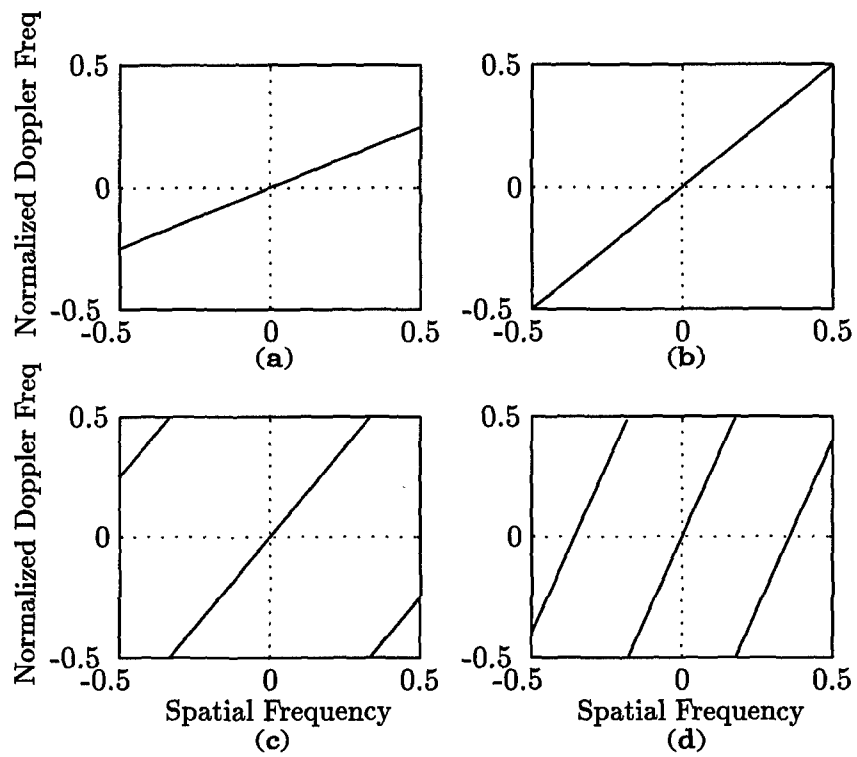


Figure 15 Clutter ridges for different values of β , $\phi_a = 0$, (a) $\beta = 0.5$, (b) $\beta = 1.0$, (c) $\beta = 1.5$, (d) $\beta = 2.8$. (The solid line represents the front lobe and the dashed line represents the back lobe.)

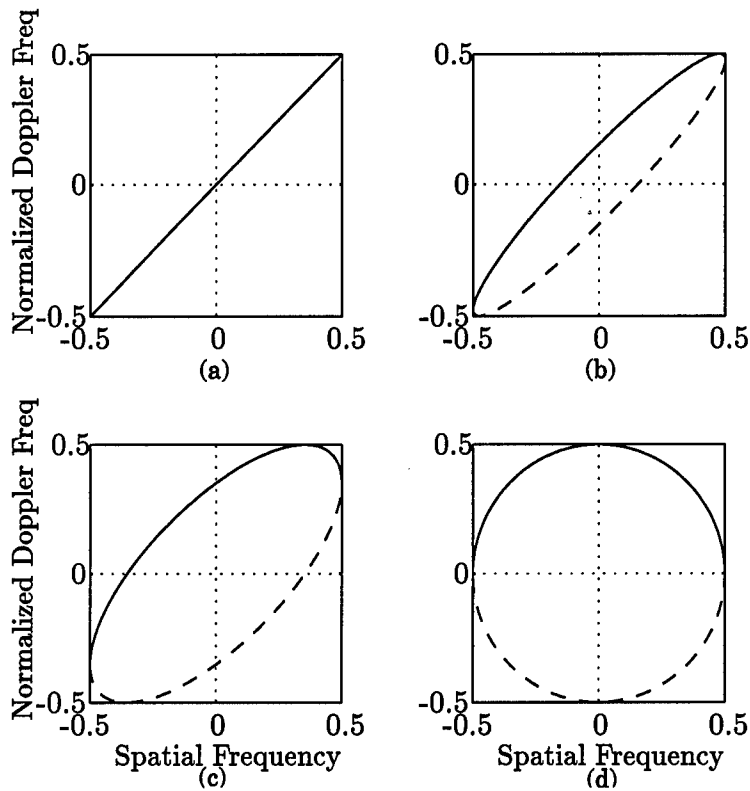


Figure 16 Clutter ridges for different misalignment angles, $\beta = 1$, (a) $\phi_a = 0^\circ$, (b) $\phi_a = 10^\circ$, (c) $\phi_a = 45^\circ$, (d) $\phi_a = 90^\circ$. (The solid line represents the front lobe and the dashed line represents the back lobe.)

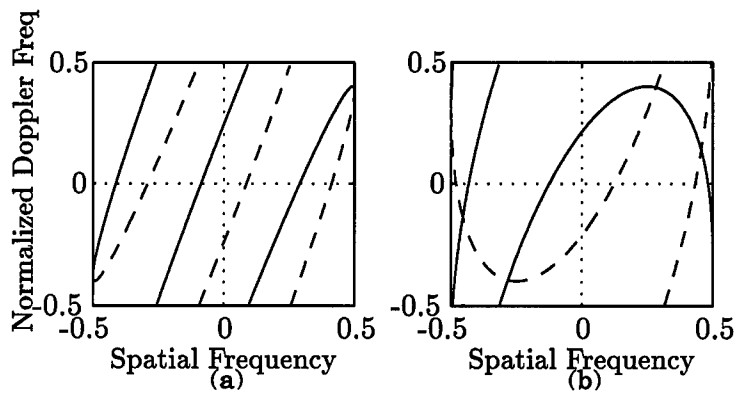


Figure 17 Clutter ridges for different combinations of ϕ_a and β . (a) $\beta = 2.8, \phi_a = 10^\circ$, (b) $\beta = 2.8, \phi_a = 60^\circ$

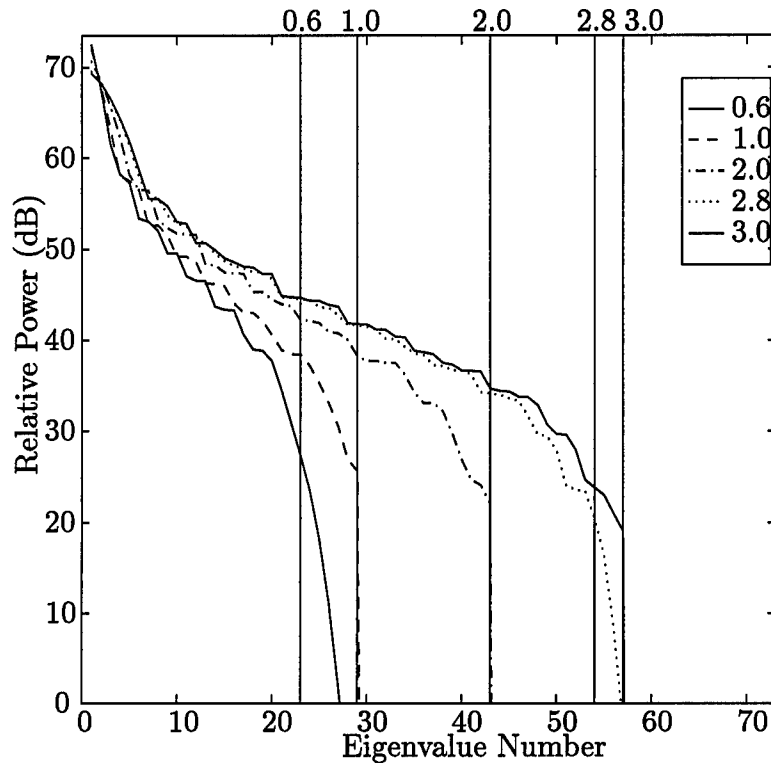


Figure 18 Clutter eigenspectra. Values of β are indicated at the top.

Theorem 1 (Brennan's Rule) *The rank of the clutter covariance matrix is approximately given by*

$$r_c \approx \lfloor N + (M - 1)\beta \rfloor \quad (100)$$

where $\beta = 2v_a T_r / d$ is the number of half-interelement-spacings traveled by the platform during one PRI. (The brackets ($\lfloor \cdot \rfloor$) indicate rounding down to the nearest integer.)

When the eigenvalues of the clutter covariance matrix are calculated, r_c predicts where the plot of the eigenspectrum will begin to roll off. The sharpness of the roll-off depends on the platform speed v_a , misalignment angle ϕ_a , back lobe level, and the existence of intrinsic clutter motion (see Section 3.6.3). A plot of the eigenspectrum for various values of β is shown in Fig. 18. In the special case where the misalignment angle $\phi_a = 0^\circ$, β is an integer, and there is no intrinsic clutter motion, the approximation in Eqn. (100) can be replaced by an equality. The eigenspectrum

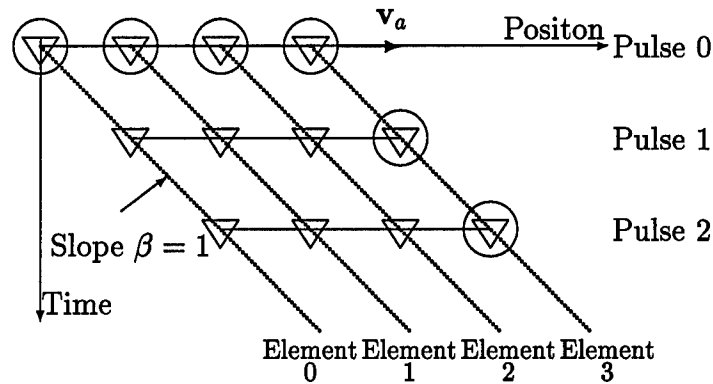


Figure 19 Effective array positions for successive pulses. Circles indicate independent measurements.

will consist of exactly r_c nonzero eigenvalues. As an illustration of why Brennan's rule holds, consider Fig. 19, for which $N = 4$, $M = 3$, and $\beta = 1$. The location of the second element during the first pulse is the same as the location of the first element on the second pulse. Assuming the clutter does not change from pulse to pulse, the two measurements will be the same. Since the two measurements are not linearly independent, the rank of the clutter covariance matrix will be reduced. For this example there are six distinct measurements, which is equal to the rank predicted by Brennan's rule. Plots of the eigenspectra under various misalignment angles are shown in Fig. 20. The amount of misalignment has little effect on the clutter eigenspectrum. Any nonzero misalignment effectively doubles the rank of the clutter covariance matrix. This is as expected, since, once the misalignment angle deviates from zero, there are two distinct clutter ridges present, one from the front lobe and another from the back lobe.

3.6.3 Intrinsic Clutter Motion. Intrinsic clutter motion (ICM) is a result of variations in the clutter reflectivity from pulse to pulse. The variations result from movement of the clutter source, such as trees moving in the wind or waves on the ocean. Pulse-to-pulse instabilities of the radar system have a similar effect and are included as part of the ICM.

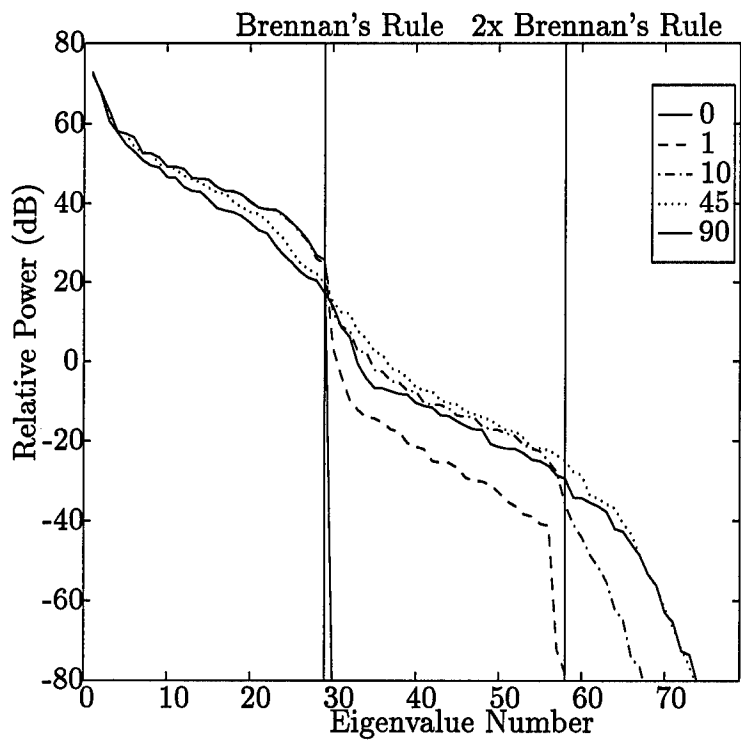


Figure 20 Clutter eigenspectra for misalignment angles of $\phi_a = 0^\circ, 1^\circ, 10^\circ, 45^\circ,$ and 90° .

From Eqn. (84), the clutter space time snapshot was given by

$$\chi_c = \sum_{k=1}^{N_c} \alpha_k \mathbf{v}_k = \sum_{k=1}^{N_c} \alpha_k \mathbf{b}_k \otimes \mathbf{a}_k.$$

When intrinsic clutter motion is present, the scalar α_k must be replaced with an $M \times 1$ vector $\boldsymbol{\alpha}_k = [\alpha_{k,0}; \alpha_{k,1}; \dots; \alpha_{k,M-1}]$, where $\alpha_{k,m}$ is the random amplitude from the k th clutter patch during the m th PRI. The space-time snapshot is now given by

$$\chi_c = \sum_{k=1}^{N_c} (\boldsymbol{\alpha}_k \odot \mathbf{b}_k) \otimes \mathbf{a}_k. \quad (101)$$

The fluctuations of the clutter will be modeled as a wide-sense-stationary process with a Gaussian Doppler spectrum. The temporal autocorrelation of the clutter fluctuations will then be given by

$$\gamma_c(m) \triangleq E \{ \alpha_{l+m} \alpha_l^* \} = \sigma_n^2 \xi_k \exp \left(-\frac{\kappa_c^2 T_r^2}{2} m^2 \right) \quad (102)$$

and the $M \times M$ covariance matrix of the fluctuations will be given by

$$\boldsymbol{\Gamma}_k = E \{ \boldsymbol{\alpha}_k \boldsymbol{\alpha}_k^H \} = \text{Toeplitz}[\gamma_c(0); \gamma_c(1); \dots; \gamma_c(M-1)], \quad (103)$$

The spectral standard deviation κ_c is generally expressed in terms of a velocity standard deviation σ_v as

$$\kappa_c = \frac{4\pi\sigma_v}{\lambda_0} \quad (104)$$

The velocity standard deviation is a measured quantity for various conditions and types of clutter. With these definitions, the clutter covariance matrix can be written as

$$\mathbf{R}_c = \sum_{k=1}^{N_c} (\boldsymbol{\Gamma}_k \odot \mathbf{b}_k \mathbf{b}_k^H) \otimes \mathbf{a}_k \mathbf{a}_k^H. \quad (105)$$

3.7 Fully Adaptive Space-Time Adaptive Processing (STAP)

A fully adaptive space-time adaptive processor computes and applies a new adaptive weight for every antenna element and every pulse. Thus, the weight vector is of size MN . The data space-time snapshot at a particular range is given by

$$\boldsymbol{\chi} = \alpha_t \mathbf{v}_t + \boldsymbol{\chi}_u, \quad (106)$$

where \mathbf{v}_t is the target space-time steering vector and $\boldsymbol{\chi}_u$ is the interference-plus-noise component of the data. The optimum weight vector can be calculated from [5]

$$\mathbf{w} = c \mathbf{R}_u^{-1} \mathbf{v}_t, \quad (107)$$

where c is a constant and \mathbf{R}_u is the interference-plus-noise covariance matrix as given in the preceding sections. This weight vector is optimum in the sense that it maximizes the signal-to-interference-plus-noise ratio (SINR) and the probability of detection for a given probability of false alarm, and, with the proper choice of c , minimizes the the output power subject to a gain constraint in the target direction. [8]

Once the weight vector is computed, the adapted pattern can be determined from

$$P_{\mathbf{w}}(\vartheta, \varpi) = \left| \mathbf{w}^H \mathbf{v}(\vartheta, \varpi) \right|^2. \quad (108)$$

Figure 21 shows a sample array pattern of the beamformer. The values of the parameters used are given in Table 2.

Table 2 Parameters used to generate Fig. 21

Number of elements	N	15
Number of pulses/CPI	M	15
Number of clutter patches	N_c	360
Transmitter peak power	P_t	200 kW
Operating frequency	f_0	450 MHz
Pulse width	T_p	200 μ s
PRF	f_r	300 Hz
Antenna transmit gain	G_t	15 dB
Element gain	g	4 dB
Element pattern	$g(\theta, \phi)$	Cosine
Instantaneous Bandwidth	B	4 MHz
Noise figure	N_0	3 dB
System Losses	L_s	4 dB
Platform height	h_a	9000 m
Platform velocity	v_a	50 m/s
Velocity misalignment angle	ϕ_a	0°
Target azimuth	ϕ_t	10°
Target Doppler	f_t	100 Hz
Target range	R_t	130 km
Target RCS	σ_t	2 m ²
Clutter terrain parameter	γ	-3 dB
Number of jammers	J	2
Jammer ERP	S_j	1000 W/Hz
Jammer range	R_j	370 km
Jammer azimuth angles	ϕ_j	-35°, 25°
Jammer elevation angles	θ_j	0°, 0°

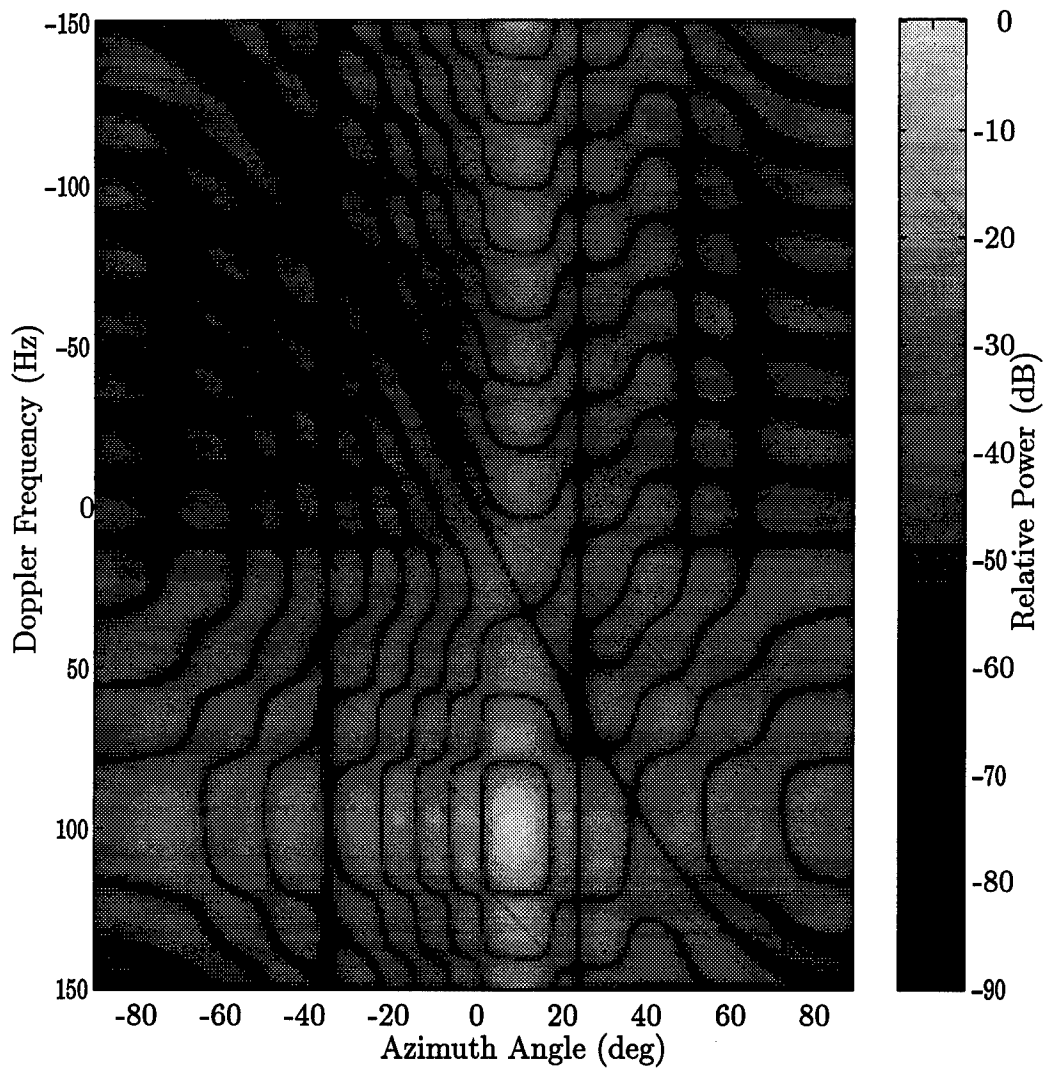


Figure 21 The adapted pattern in the presence of a target at 10° , 100 Hz, two jammers at 25° and -35° , and clutter.

3.8 Signal-to-Interference-plus-Noise Ratio

A common measure of performance is the output signal-to-interference-plus-noise ratio (SINR). The output signal from the beamformer is given by

$$z = \alpha_t \mathbf{w}^H \mathbf{v}_t + \mathbf{w}^H \boldsymbol{\chi}_u, \quad (109)$$

where the first term is due to the target signal and the second term is due to the undesired signals. Computing the power in each signal and finding the ratio give the SINR,

$$SINR = \frac{\xi_t |\mathbf{w}^H \mathbf{v}_t|^2}{\mathbf{w}^H \mathbf{R}_u \mathbf{w}}. \quad (110)$$

If the optimum weight vector is used, this expression reduces to

$$SINR_{opt} = \xi_t \mathbf{v}_t^H \mathbf{R}^{-1} \mathbf{v}_t. \quad (111)$$

By letting $\mathbf{v}_t(\varpi) = \mathbf{b}(\varpi) \otimes \mathbf{a}(\vartheta_t)$, the SINR can be computed as a function of target Doppler from

$$SINR(\varpi) = \xi_t \mathbf{v}_t(\varpi)^H \mathbf{R}^{-1} \mathbf{v}_t(\varpi). \quad (112)$$

Similarly, the SINR can be calculated as a function of target azimuth as

$$SINR(\vartheta) = \xi_t(\vartheta) \mathbf{v}_t(\vartheta)^H \mathbf{R}^{-1} \mathbf{v}_t(\vartheta), \quad (113)$$

where $\xi_t(\vartheta)$ depends on the gain of the antenna when steered in the direction of interest.

3.9 Summary

In this chapter, we have presented a theoretical development of the signals involved in space-time adaptive processing. For a linear array of N elements which transmits a coherent burst of M pulses, the spatial and temporal steering vectors

are defined to be

$$\begin{aligned}\mathbf{a}(\vartheta) &= [1; e^{j2\pi\vartheta}; \dots; e^{j(N-1)2\pi\vartheta}] \\ \mathbf{b}(\varpi) &= [1; e^{j2\pi\varpi}; \dots; e^{j(M-1)2\pi\varpi}],\end{aligned}$$

and the space-time steering vector is defined as the Kronecker product of these two vectors,

$$\mathbf{v}(\vartheta, \varpi) = \mathbf{b}(\varpi) \otimes \mathbf{a}(\vartheta).$$

The target space-time snapshot is found by multiplying the target space-time steering vector by the complex amplitude of the target return,

$$\boldsymbol{\chi}_t = \alpha_t \mathbf{b}_t \otimes \mathbf{a}_t.$$

The space-time snapshot of the noise internal to the receiver is modeled as a random vector, and the covariance matrix of the noise was represented as a $MN \otimes MN$ identity matrix. The jammer signal is modeled as a random vector $\boldsymbol{\alpha}_j$, of length M . The space-time snapshot for the jammer is the Kronecker product of this signal vector with the jammer steering vector,

$$\boldsymbol{\chi}_j = \boldsymbol{\alpha}_j \otimes \mathbf{a}_j.$$

The jammer covariance matrix is given by

$$\mathbf{R}_j = \mathbf{I}_M \otimes (\mathbf{A}_j \boldsymbol{\Xi}_j \mathbf{A}_j^H),$$

where \mathbf{A}_j is a matrix of the spatial steering vectors for all the jammers, and $\boldsymbol{\Xi}_j$ is a diagonal matrix of the jammer powers. The clutter space-time snapshot is the sum

of the space-time snapshots of all the clutter patches,

$$\boldsymbol{\chi}_c = \sum_{k=1}^{N_c} \alpha_k \mathbf{b}_k \otimes \mathbf{a}_k.$$

The clutter covariance matrix is given by

$$\mathbf{R}_c = \mathbf{V}_c \boldsymbol{\Xi}_c \mathbf{V}_c^H,$$

where \mathbf{V}_c is a matrix of the space-time steering vectors to each clutter patch and $\boldsymbol{\Xi}_c$ is a diagonal matrix of the clutter power distribution.

The total covariance matrix is the sum of the covariance matrices of the noise, jammer, and clutter signal. The optimum weight vector is found by inverting the covariance matrix of the undesired signals and multiplying by the target spatial steering vector,

$$\mathbf{w} = \mathbf{R}_u^{-1} \mathbf{v}_t.$$

The adapted angle-Doppler pattern of the antenna is found from

$$P_{\mathbf{w}}(\vartheta, \varpi) = \left| \mathbf{w}^H \mathbf{v}(\vartheta, \varpi) \right|^2.$$

The SINR is used as a measure of the processor. If the optimum weight vector is used, the SINR is given by

$$SINR = \xi_t \mathbf{v}_t^H \mathbf{R}_u^{-1} \mathbf{v}_t.$$

The following chapter extends these results to include the effects of near-field scatterers.

IV. Near-Field Scatterers

4.1 Introduction

To this point in the analysis of space-time adaptive processing, we have assumed the array is in free space. This is clearly not a realistic situation. The array must be mounted on a platform of some type. Depending on the position of the array, parts of the platform, such as the wing or the tail, may be in the field of view of the array. The signals from the target, jammers and clutter will reflect off these *near-field scatterers* (NFS) into the array, increasing the complexity of the total signal received by the array.

Yu, Burnside, and Gilreath [10] developed a geometrical theory of diffraction (GTD) model of the signals which will enter an antenna mounted on the surface of an airframe. Their model included the effects of reflections off the airframe waves which strike the airframe at a tangent and propagate along the surface of the airframe to the antenna. Barile et al. [3] describe the effect of a near-field scatterer on a two-element displaced phase center antenna (DPCA). Figure 22 illustrates the four paths by which a signal transmitted by the first element can travel to the target and back to the array. Figure 22(a) shows the direct path for the transmitted and received signals. This is the same as in Chapter III. Figure 22(b) shows the case in which the transmitted signal follows the direct path to the target and reflects off the NFS on return before entering the array. Figure 22(c) shows the transmitted signal reflecting off the NFS before traveling to the target and following the direct path to return to the array. Figure 22(d) shows the double-bounce case, in which the both the transmit and received signals reflect off the NFS. Each combination of antenna element and near-field scatterer will produce a similar set of signal paths. For the purpose of this analysis, the signals which scatter off the NFS more than once, as in Figure 22(d), will be assumed to have negligible power compared to the direct path and

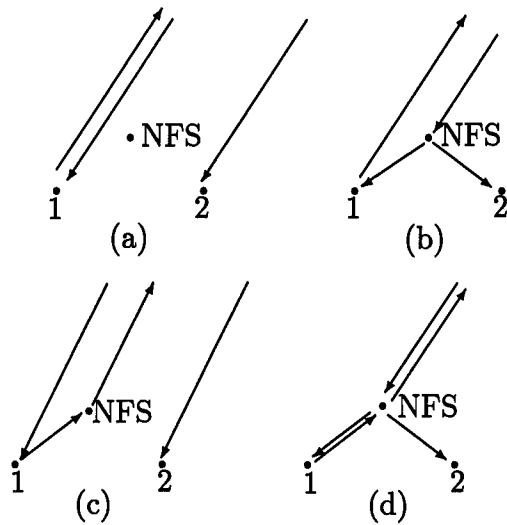


Figure 22 Four possible paths for a signal transmitted from the first element to travel to the target and return to the array: (a) direct path to and from target, (b) Path B, direct path to target, scattering path on return, (c) Path C, scattering path to target, direct path on return, (d) Path D, scattering path to and from target.

single bounce paths. In the case of multiple NFS, this assumption will also eliminate signals which bounce off two or more different scatterers.

In a later paper [4], Barile et al. discuss the effect of a near-field scatterer on the signal incident on an array in the presence of range ambiguous clutter. Each range ambiguity will contain a component plane wave with the same Doppler frequency as the target. When this component scatters off the NFS into the array, part of the scattered wave will have the same horizontal wavenumber and Doppler frequency as the target return, but a different vertical wavenumber. A linear array like the one discussed in Section 3.2, which is only adaptive in azimuth, will not be able to distinguish between the target and the interference. Fully adaptive STAP with a two-dimensional array which is adaptive in both azimuth and elevation will accurately null out the signal from the NFS, but at significant cost in processing time. In [4], the authors propose preadaptive near-field nulling to reduce the processing required with a two-dimensional array. The NFS is assumed to be at a fixed, measurable

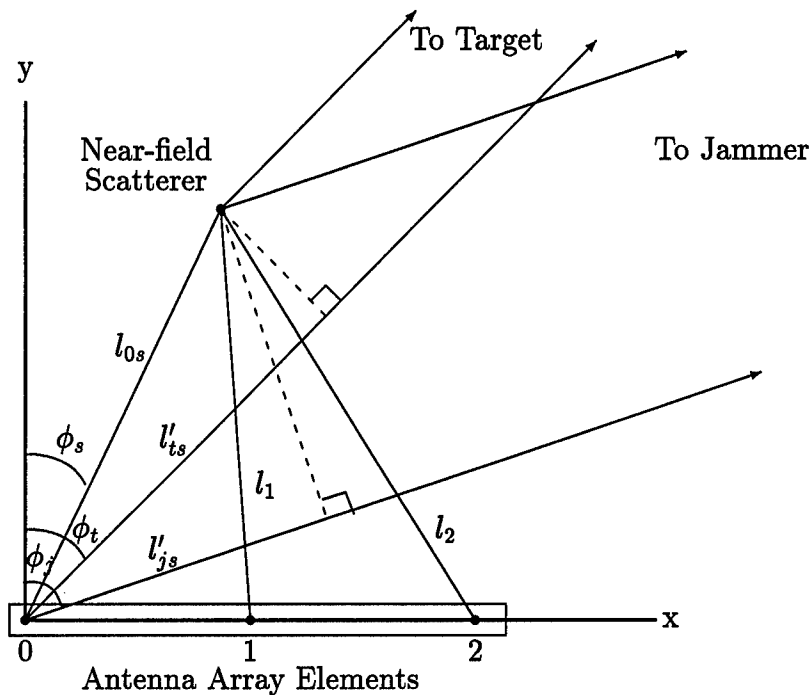


Figure 23 Geometry of the radar system including the near-field scatterer.

location relative to the array. The receiver weights required to place a null in the direction of the NFS are precomputed for each column of the array. The adaptive processor then weights the rows of the array to null out clutter and jamming signals in azimuth. This procedure reduces the degrees of freedom available to the processor, but also reduces the complexity of the calculations required to shape the beam.

This chapter will parallel the derivation presented in Chapter 3, but include the effects of the near-field scatterer. The scatterers will be assumed to be point scatterers, from which the scattered wave pattern will be isotropic and independent of the direction of incidence. Because the scatterer is in the near-field of the array, the scattered waves must be treated as spherical, meaning each receiver in the array will detect a signal with different amplitude and direction of arrival.

4.2 Radar System

The geometry of the system is the same as described earlier, with the addition of the near-field scatterer (NFS), as illustrated in Fig. 23. To begin, a single near-field scatterer is located in polar coordinates at (l_{0s}, ϕ_{0s}) , where the origin is the 0th element of the array and the angle ϕ is measured from the normal to the array. The target signal originates from an angle ϕ_t , and a jammer signal is at ϕ_j . The antenna elements are identical and are equally spaced along the x -axis. The NFS is assumed to be a point scatterer close enough to the array to require the scattered wave to be treated as spherical. The NFS is assumed to have no effect on the temporal information in the plane wave, so the temporal steering vector \mathbf{b} is the same for the scattered and direct path waves. Because the scatterers are close to the array (within a few meters), the delay of the scattered signal is be small compared to the pulse width. Therefore, the scattered signal enters the array in the same PRI as the direct path signal.

The distance from the scatterer to the n th antenna element is given by

$$l_{ns} = [l_{0s}^2 + (nd)^2 - 2l_{0s}nd \sin(\phi_{ns})]^{1/2}. \quad (114)$$

For the case of multiple scatterers, the subscript s denotes the scatterer being referenced, so that l_{ns} is the distance from the n th antenna element to the s th scatterer. The projection of l_{0s} onto the direct path to the target is given by

$$l'_{ts} = l_{0s} \cos(\phi_t - \phi_{0s}). \quad (115)$$

For the direct path signal, the incident wave was assumed to be planar, so the signal received by each element contained the same amount of energy and the phase progression across the array was linear. The wave from a near-field scatterer is not planar. Each element receives a different amount of scattered energy, determined by its distance from the scatterer. The ratio of the power of the scattered signal received

Table 3 Symbols for near-field scatterer

ϕ_t	angle to target
ϕ_j	angle to jammer
ψ_d	phase shift imposed by NFS
ϕ_{ns}	angle from n th element to s th scatterer
S	number of near-field scatterers
l_{ns}	distance from n th element to s th scatterer $= [l_{0s}^2 + (nd)^2 - 2l_{0s}nd \sin(\phi_{ns})]^{1/2}$
l'_{ts}	projection of l_{0s} onto direct path $= l_{0s} \cos(\phi_t - \phi_{0s})$
σ_s	NFS bistatic radar cross section
ζ_{ns}	scattering loss $= \sigma_s / (4\pi l_{ns}^2)$

by the n th element to the power of the signal incident on the NFS will be referred to as the *scattering loss* and is given by $\zeta_{ns} = \sigma_s / (4\pi l_{ns}^2)$, where σ_s is the bistatic radar cross section (RCS) of the scatterer. For a point scatterer, σ_s is independent of incident angle and the scattered wave will be isotropic. The power of the signal from the scatterer incident on the n th antenna element is found by multiplying the power incident on the scatterer by the scattering loss.

Because the distance from the scatterer to each element in the antenna array has a nonlinear dependence on the interelement spacing, the phase progression of the steering vector is nonlinear. The relative phase shift at the n th element, referenced to the 0th element, will be given by $(2\pi/\lambda_0)(l_{0s} - l_{ns})$. There will also be a phase shift of $\psi_d = 180^\circ$ when the signal reflects off the NFS. The parameters related to the near-field scatterer are summarized in Table 3.

The space-time snapshot will be similar in form to Eqn. (50),

$$\tilde{\chi} = \tilde{\chi}_t + \tilde{\chi}_u, \quad (116)$$

where the tilde (\sim) indicates the presence of signals from the NFS. In addition to the direct path terms, the new target space-time snapshot will include terms due to

the scattered target signals, and the undesired signal component will include terms due to the scattered clutter and jammer signals.

The scattered target signal does not have the same spatial steering vector as the direct path signal, but the temporal steering vector is unaffected and the amplitude of the signal is still be deterministic. Therefore, the scattered target signal only shifts the mean of the space-time snapshot, leaving the covariance of the data unaffected. The total covariance matrix is now given by

$$\begin{aligned}\tilde{\mathbf{R}}_u &= E[(\tilde{\chi}_u \tilde{\chi}_u^H)] \\ &= E[(\tilde{\chi}_c + \tilde{\chi}_j + \chi_n)(\tilde{\chi}_c + \tilde{\chi}_j + \chi_n)^H].\end{aligned}\quad (117)$$

The direct path and scattered clutter returns are correlated, and therefore must be combined in the computation of the clutter covariance matrix. The same is true of the jammer signal. The clutter, jammer, and noise signals are assumed to be mutually uncorrelated, so the total covariance matrix can be written as

$$\begin{aligned}\tilde{\mathbf{R}}_u &= E[\tilde{\chi}_c \tilde{\chi}_c^H] + E[\tilde{\chi}_j \tilde{\chi}_j^H] + E[\chi_n \chi_n^H] \\ &= \tilde{\mathbf{R}}_c + \tilde{\mathbf{R}}_j + \mathbf{R}_n,\end{aligned}\quad (118)$$

where the tilde (\sim) indicates the covariance matrix includes the effects of signals from the near-field scatterer.

4.3 Scattered Target Signal

The signal received from the target by the n th antenna element is the sum of the direct and scattered paths. For the m th pulse, the direct path signal at the n th element is given by Eqn. (64) and is repeated here:

$$x_{mn} = a_r e^{j\psi} e^{jm2\pi\omega t} e^{jn2\pi\vartheta t} = \alpha_t e^{jm2\pi\omega t} e^{jn2\pi\vartheta t}.$$

The signal which travels the direct path to the target and bounces off the NFS on the return (Path B) is indicated by the minus (-) superscript and is given by

$$x_{mn}^- = \alpha_t a_{tns}^- e^{jm2\pi\omega t} e^{-j\frac{2\pi}{\lambda_0}(l_{ns}-l'_{ts})} e^{j\psi_d}, \quad (119)$$

where l'_{ts} is as defined in Eqn. (115) and

$$a_{tns}^- = \left[\frac{g(\phi)_{ns}}{g(\phi)_t} \zeta_{ns} \right]^{\frac{1}{2}}. \quad (120)$$

This expression is obtained by computing the single pulse signal-to-noise ratio (SNR) for the scattered signals,

$$\xi_{ts}^- = \frac{P_t T_p G_t(\phi_t) g(\phi_{ns}) \lambda_0^2 \sigma_t}{(4\pi)^3 N_0 L_s R_t^4} \zeta_{ns}, \quad (121)$$

and dividing the result by the SNR of the direct path signal given by Eqn. (65). All the terms will cancel except the element gains in the target and scatterer directions, $g(\phi_t)$ and $g(\phi_{ns})$, and the scattering loss, ζ_{ns} . Equation (120) represents the energy ratio of the scattered path signal to the direct path signal. The subscripts t, n and s represent respectively the target, the n th antenna element, and the s th near-field scatterer. By defining

$$d_{tns}^- = a_{tns}^- e^{-j\frac{2\pi}{\lambda_0}(l_{ns}-l'_{ts})} e^{j\psi_d}, \quad (122)$$

Eqn. (119) can be written as

$$x_{mn}^- = \alpha_t d_{tns}^- e^{jm2\pi\omega t}. \quad (123)$$

This expression is similar to Eqn. (64), with d_{tns}^- replacing $e^{n2\pi\vartheta t}$. The space-time snapshot of the signals which have followed the path of Fig. 22(b) can be written as

$$\chi_t^- = \alpha_t \mathbf{b}_t \otimes \mathbf{d}_{ts}^-, \quad (124)$$

where $\mathbf{d}_{ts}^- = [d_{t0s}^-; d_{t1s}^-; \dots; d_{t(N-1)s}^-]$ represents the spatial steering vector for the scattered target signal. Because each element is a different distance from the scatterer, each element of this vector has a different amplitude, and the phase progression across the elements is nonlinear.

The signal entering the n th receiver which bounced off the NFS before going to the target [Fig. 22(c)] is indicated by the plus (+) superscript. This signal is more complicated. Because each element is a different distance from the NFS, there will appear to be N pulses being transmitted from the NFS, each with a different amplitude and phase. The signal received by the n th element is the sum of these N pulses:

$$\begin{aligned}
x_{mn}^+ &= \alpha_t \left[a_{t0s}^+ e^{-j\frac{2\pi}{\lambda_0}(l_{0s}-l'_{ts})} + a_{t1s}^+ e^{-j\frac{2\pi}{\lambda_0}(l_{1s}-l'_{ts})} e^{-j2\pi\vartheta_t} + \dots \right. \\
&\quad \left. + a_{t(N-1)s}^+ e^{-j\frac{2\pi}{\lambda_0}(l_{(N-1)s}-l'_{ts})} e^{-j(N-1)2\pi\vartheta_t} \right] e^{jm2\pi\omega_t} e^{jn2\pi\vartheta_t} e^{j\psi_d} \\
&= \alpha_t e^{jm2\pi\omega_t} e^{jn2\pi\vartheta_t} e^{j\psi_d} \sum_{p=0}^{N-1} a_{tps}^+ e^{-j\frac{2\pi}{\lambda_0}(l_{ps}-l'_{ts})} e^{-jp2\pi\vartheta_t} \\
&= \alpha_t e^{jm2\pi\omega_t} e^{jn2\pi\vartheta_t} e^{j\psi_d} \sum_{p=0}^{N-1} d_{tps}^+ \\
&= \alpha_t e^{jm2\pi\omega_t} d_{tns}^+, \tag{125}
\end{aligned}$$

where

$$a_{tps}^+ = \left[\frac{g(\phi_{ps})}{G_t(\phi_t)} \zeta_{ps} \right]^{\frac{1}{2}} \tag{126}$$

$$d_{tps}^+ = a_{tps}^+ e^{-j\frac{2\pi}{\lambda}(l_{ps}-l'_{ts})} e^{-jp2\pi\vartheta_t} \tag{127}$$

$$d_{tns}^+ = e^{jn2\pi\vartheta_t} e^{j\psi_d} \sum_{p=0}^{N-1} d_{tps}^+. \tag{128}$$

The space-time snapshot due to the signals in Eqn. (125) can be written as

$$\chi_t^+ = \alpha_t \mathbf{b}_t \otimes \mathbf{d}_{ts}^+. \tag{129}$$

The total target space-time snapshot is found by adding Eqns. (124), (129), and (71)

$$\begin{aligned}
\tilde{\chi}_t &= \chi_t + \chi_t^- + \chi_t^+ \\
&= \alpha_t(\mathbf{b}_t \otimes \mathbf{a}_t) + \alpha_t(\mathbf{b}_t \otimes \mathbf{d}_{ts}^-) + \alpha_t(\mathbf{b}_t \otimes \mathbf{d}_{ts}^+) \\
&= \alpha_t \mathbf{b}_t \otimes (\mathbf{a}_t + \mathbf{d}_{ts}^- + \mathbf{d}_{ts}^+).
\end{aligned} \tag{130}$$

For multiple scatterers, Eqns. (122) and (128) must be summed over all scatterers, and Eqn. (130) becomes

$$\begin{aligned}
\tilde{\chi}_t &= \alpha_t \mathbf{b}_t \otimes \left[\mathbf{a}_t + \sum_{s=0}^{S-1} (\mathbf{d}_{ts}^- + \mathbf{d}_{ts}^+) \right] \\
&= \alpha_t \mathbf{b}_t \otimes \tilde{\mathbf{a}}_t.
\end{aligned} \tag{131}$$

The term $\tilde{\mathbf{a}}_t$ in Eqn. (131) can be considered the spatial steering vector of the target signal entering the array through both the direct and scattered paths. The Kronecker product of the temporal steering vector, \mathbf{b}_t , with this spatial steering vector gives the space-time steering vector for the target due to both the direct and scattered paths,

$$\tilde{\mathbf{v}}_t = \mathbf{b}_t \otimes \tilde{\mathbf{a}}_t. \tag{132}$$

This expression will be used later in the calculation of the ideal weight vector.

4.4 Scattered Jammer Signal

We will begin by considering a single jammer and single NFS. The parameter l'_{js} is similar to l'_{ts} given by Eqn. (115), except the angle to the jammer is used in place of the target angle,

$$l'_{js} = l_{0s} \cos(\phi_j - \phi_{0s}). \tag{133}$$

The total jammer signal contains two components: the direct path and the Jammer-NFS-array path. During the m th PRI, the signal received by the n th receiver which

has scattered off the NFS will be given by

$$\mathbf{x}_{mn}^- = \alpha_m \mathbf{a}_{jns}^- e^{-j\frac{2\pi}{\lambda_0}(l_{ns}-l'_{js})} e^{j\psi_d}, \quad (134)$$

where

$$\mathbf{a}_{jns}^- = \left[\frac{g(\phi_{ns})}{g(\phi_j)} \zeta_{ns} \right]^{\frac{1}{2}}. \quad (135)$$

From these expressions, the components of the spatial steering vector of the scattered jamming signal can be written as

$$\mathbf{d}_{jns}^- = \mathbf{a}_{jns}^- e^{-j\frac{2\pi}{\lambda_0}(l_{ns}-l'_{js})} e^{j\psi_d}. \quad (136)$$

By defining

$$\tilde{\mathbf{a}}_j = \mathbf{a}_j + \mathbf{d}_{jns}^-, \quad (137)$$

the jammer space-time snapshot is now given by

$$\tilde{\boldsymbol{\chi}}_j = \boldsymbol{\alpha}_j \otimes \tilde{\mathbf{a}}_j = \boldsymbol{\alpha}_j \otimes \mathbf{a}_j + \boldsymbol{\alpha}_j \otimes \mathbf{d}_j^- = \boldsymbol{\chi}_j + \boldsymbol{\chi}_{js}. \quad (138)$$

The jammer covariance matrix is computed as in Eqn. (78), with $\tilde{\mathbf{a}}_j$ replacing \mathbf{a}_j ,

$$\begin{aligned} \tilde{\mathbf{R}}_j &= E \{ \tilde{\boldsymbol{\chi}}_j \tilde{\boldsymbol{\chi}}_j^H \} = E \{ (\boldsymbol{\alpha}_j \otimes \tilde{\mathbf{a}}_j) (\boldsymbol{\alpha}_j \otimes \tilde{\mathbf{a}}_j)^H \} \\ &= E(\boldsymbol{\alpha}_j \boldsymbol{\alpha}_j^H) \otimes (\tilde{\mathbf{a}}_j \tilde{\mathbf{a}}_j^H) \\ &= \sigma_n^2 \xi_j \mathbf{I}_M \otimes (\tilde{\mathbf{a}}_j \tilde{\mathbf{a}}_j^H) \\ &= \mathbf{I}_M \otimes \tilde{\boldsymbol{\Phi}}_j. \end{aligned} \quad (139)$$

For J jammers, $\tilde{\boldsymbol{\Phi}}_j$ can be extended in the same manner as in Section 3.5,

$$\tilde{\boldsymbol{\Phi}}_j = \tilde{\mathbf{A}}_j \boldsymbol{\Xi}_j \tilde{\mathbf{A}}_j^H, \quad (140)$$

where

$$\begin{aligned}\tilde{\mathbf{A}}_j &= [\tilde{\mathbf{a}}_j(\phi_1), \tilde{\mathbf{a}}_j(\phi_2), \dots, \tilde{\mathbf{a}}_j(\phi_J)] \\ &= [\tilde{\mathbf{a}}_1, \tilde{\mathbf{a}}_2, \dots, \tilde{\mathbf{a}}_J].\end{aligned}\quad (141)$$

For S scatterers, \mathbf{d}_{js} in Eqn. (137) must be summed over all the scatterers,

$$\tilde{\mathbf{a}}_j = \mathbf{a}_j + \sum_{s=0}^{S-1} \mathbf{d}_{js}^-.\quad (142)$$

This expression can then be used in Eqn. (141).

4.5 Scattered Clutter Signal

The return from each clutter patch consists of a set of signals similar to the set of target signals. There is the direct path signal, the two single-bounce path signals, and a double-bounce path. As with the target signal, the double-bounce path will be ignored in computing the total clutter return. It is assumed there is no misalignment angle ($\phi_a = 0$) and no intrinsic clutter motion.

The direct path signal is, from Eqn. (84),

$$\chi_c = \sum_{k=1}^{N_c} \alpha_k \mathbf{v}_k = \sum_{k=1}^{N_c} \alpha_k (\mathbf{b}_k \otimes \mathbf{a}_k).$$

The signal which bounces off the NFS while returning from the k th clutter patch [Fig. 22(b)] is given by

$$\begin{aligned}x_{knm}^- &= \alpha_k a_{kn_s}^- e^{jm2\pi\varpi_k} e^{-j\frac{2\pi}{\lambda_0}(l_{ns} - l'_{ks})} e^{j\psi_d} \\ &= \alpha_k e^{jm2\pi\varpi_k} d_{kn_s}^-.\end{aligned}\quad (143)$$

The space-time snapshot for this set of signals is found by summing over all the near-field scatterers and all the clutter patches,

$$\boldsymbol{\chi}_c^- = \sum_{k=1}^{N_c} \alpha_k \left(\mathbf{b}_k \otimes \sum_{s=0}^{S-1} \mathbf{d}_{ks}^- \right) \quad (144)$$

The signal which bounces off the NFS before traveling to the k th clutter patch [Fig. 22(c)] is given by

$$\begin{aligned} x_{kmn}^+ &= \alpha_k \left[a_{k0s}^+ e^{-j\frac{2\pi}{\lambda_0}(l_{0s}-l_{ks})'} + a_{k1s}^+ e^{-j\frac{2\pi}{\lambda_0}(l_{1s}-l'_{ks})} e^{-j2\pi\vartheta_k} + \dots \right. \\ &\quad \left. + a_{k(N-1)s}^+ e^{-j\frac{2\pi}{\lambda_0}(l_{(N-1)s}-l'_{ks})} e^{-j(N-1)2\pi\vartheta_k} \right] e^{jm2\pi\omega_t} e^{jn2\pi\vartheta_k} e^{j\psi_d} \\ &= \alpha_k e^{jm2\pi\omega_t} e^{jn2\pi\vartheta_k} e^{j\psi_d} \sum_{p=0}^{N-1} a_{kps}^+ e^{-j\frac{2\pi}{\lambda_0}(l_{ps}-l'_{ks})} e^{-jp2\pi\vartheta_k} \\ &= \alpha_k e^{jm2\pi\omega_t} e^{jn2\pi\vartheta_k} e^{j\psi_d} \sum_{p=0}^{N-1} d_{kps}^+ \\ &= \alpha_k e^{jm2\pi\omega_t} d_{kns}^+. \end{aligned} \quad (145)$$

The space-time snapshot due to these signals is given by

$$\boldsymbol{\chi}_c^+ = \sum_{k=1}^{N_c} \alpha_k \left(\mathbf{b}_k \otimes \sum_{s=0}^{S-1} \mathbf{d}_{ks}^+ \right). \quad (146)$$

The total clutter space-time snapshot is found by adding Eqns. (144) and (146) to (84),

$$\begin{aligned} \tilde{\boldsymbol{\chi}}_c &= \boldsymbol{\chi}_c + \boldsymbol{\chi}_c^- + \boldsymbol{\chi}_c^+ \\ &= \sum_{k=1}^{N_c} \left[\alpha_k \mathbf{b}_k \otimes \mathbf{a}_k + \sum_{s=0}^{S-1} \left(\alpha_k \mathbf{b}_k \otimes \mathbf{d}_{ks}^- + \alpha_k \mathbf{b}_k \otimes \mathbf{d}_{ks}^+ \right) \right] \\ &= \sum_{k=1}^{N_c} \left(\alpha_k \mathbf{b}_k \otimes \left[\mathbf{a}_k + \sum_{s=0}^{S-1} \left(\mathbf{d}_{ks}^- + \mathbf{d}_{ks}^+ \right) \right] \right). \end{aligned} \quad (147)$$

By defining

$$\tilde{\mathbf{v}}_k = \mathbf{b}_k \otimes \left[\mathbf{a}_k + \sum_{s=0}^{S-1} \left(\mathbf{d}_{ks}^- + \mathbf{d}_{ks}^+ \right) \right] \quad (148)$$

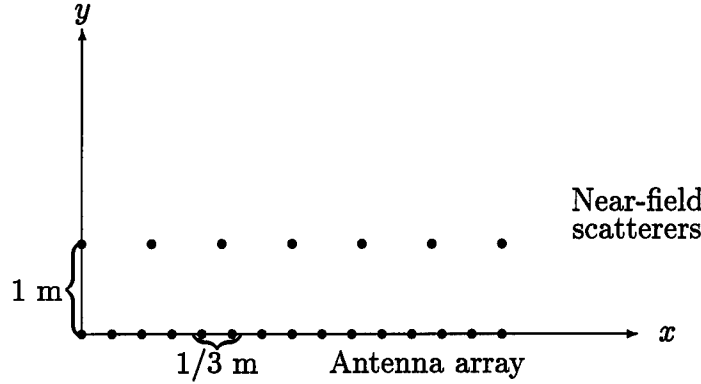


Figure 24 Location of the near-field scatterers relative to the array.

and

$$\tilde{\mathbf{V}}_c = [\tilde{\mathbf{v}}_1; \tilde{\mathbf{v}}_2; \cdots; \tilde{\mathbf{v}}_{N_c}], \quad (149)$$

the total clutter covariance matrix can be written in the same form as Eqn. (89),

$$\tilde{\mathbf{R}}_c = \tilde{\mathbf{V}}_c \Xi_c \tilde{\mathbf{V}}_c^H. \quad (150)$$

The clutter covariance matrix will not be Toeplitz-block-Toeplitz as in Section 3.6. The blocks within the matrix lose their Toeplitz structure when the near-field scatterers are introduced. Since the temporal information of the signal is not affected, the matrix will retain its block-Toeplitz structure. The clutter covariance matrix shown in Fig. 25 was generated for the same conditions as used in Fig. 14, but with the addition of seven near-field scatterers with a RCS of 0.5 m^2 , spaced equally, one meter in front of the array, as illustrated in Fig. 24. Figure 26 is a magnified view of the upper left corner of the covariance matrix

4.6 Fully Adaptive Processing in the Presence of Near-field Scatterers

As in Chapter 3, the total covariance matrix is the sum of the jammer, clutter, and noise covariance matrices. In the presence of near-field scatterers, Eqns. (139),

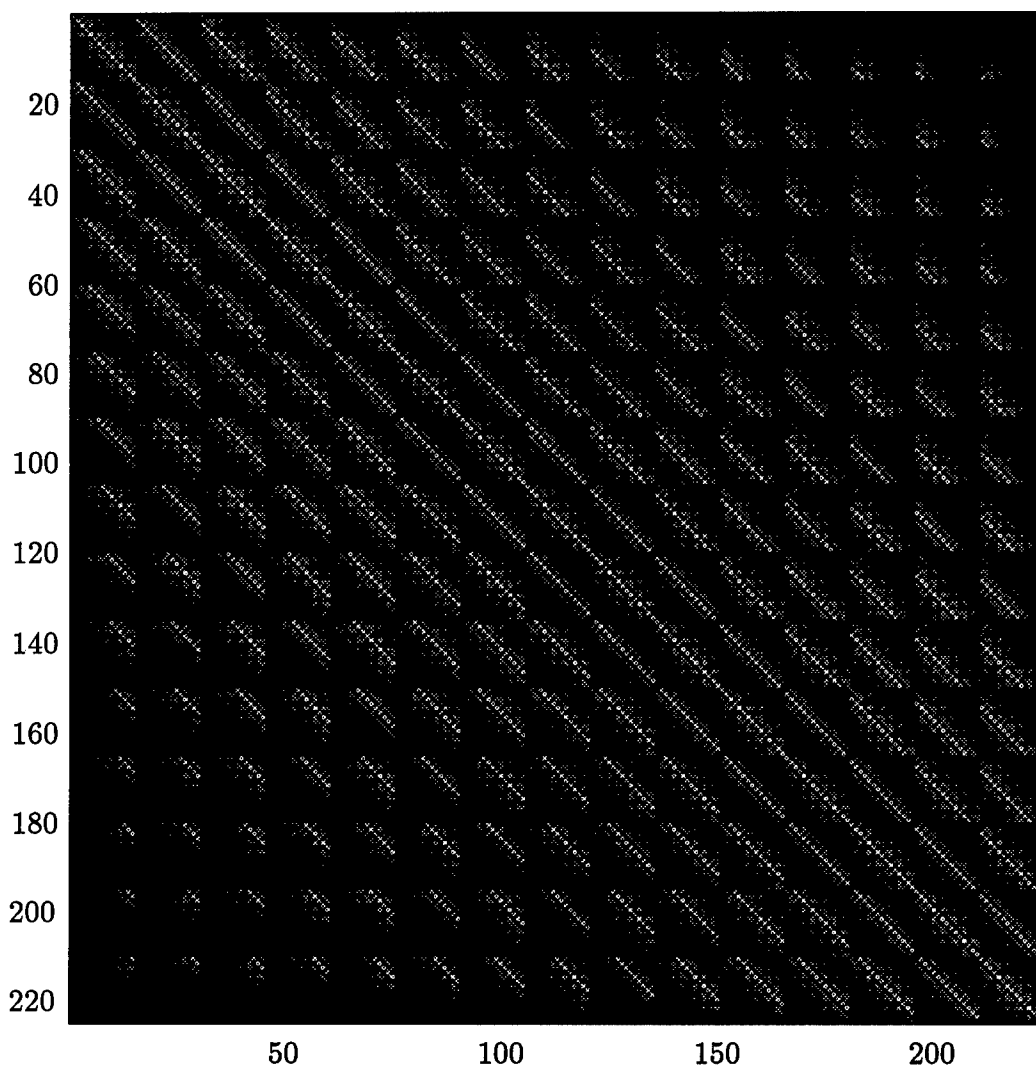


Figure 25 Clutter covariance matrix in the presence of seven near-field scatterers.

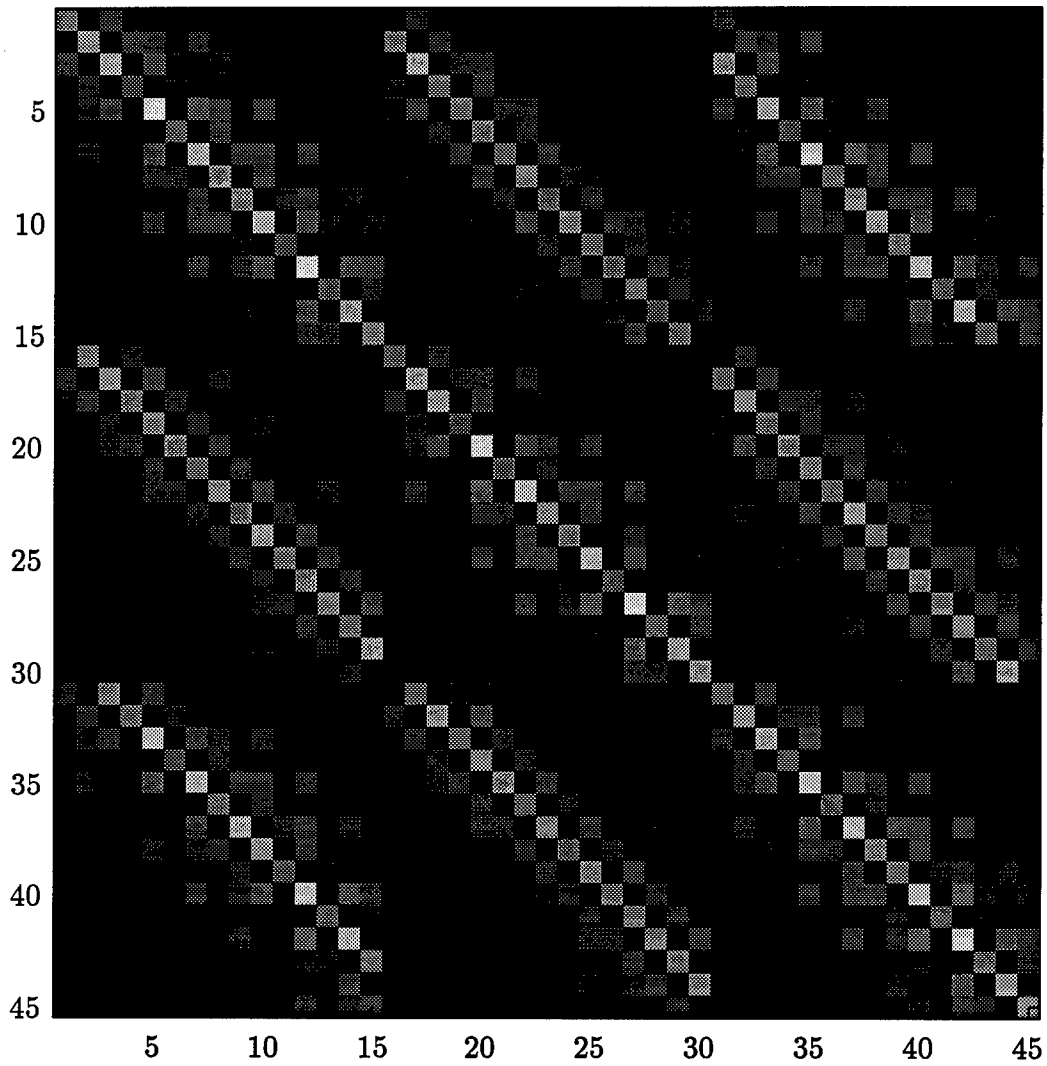


Figure 26 Upper left corner of the clutter covariance matrix in the presence of seven near-field scatterers.

(150), must be used in place of Eqns. (78) and (89),

$$\tilde{\mathbf{R}}_u = \tilde{\mathbf{R}}_j + \tilde{\mathbf{R}}_c + \mathbf{R}_n. \quad (151)$$

The form of the optimum weight vector is the same as Eqn. (107), but using the covariance matrix of Eqn. (151) and the target space-time steering vector of Eqn. (132).

The optimum weight vector is given by

$$\begin{aligned} \tilde{\mathbf{w}} &= \tilde{\mathbf{R}}_u^{-1} \tilde{\mathbf{v}}_t \\ \tilde{\mathbf{w}} &= \tilde{\mathbf{R}}_u^{-1} \left[\mathbf{b}_t \otimes \left(\mathbf{a}_t + \sum_{s=0}^{S-1} [\mathbf{d}_{ts}^- + \mathbf{d}_{ts}^+] \right) \right], \end{aligned} \quad (152)$$

where \mathbf{d}_{ts}^- and \mathbf{d}_{ts}^+ are as defined in Eqns. 4.3. This weight vector is then used to determine the adapted angle-Doppler pattern of the antenna as in Eqn. (108),

$$P_{\tilde{\mathbf{w}}}(\vartheta, \varpi) = \left| \tilde{\mathbf{w}}^H \tilde{\mathbf{v}}(\vartheta, \varpi) \right|^2. \quad (153)$$

The resulting adapted pattern is shown in Fig. 27. The same parameters were used as listed in Table 2, with the scatterer configuration shown in Fig. 24. Note how the sidelobe structure has been distorted in the presence of near-field scatterers. This distortion causes the clutter and jammer nulls to become blurred, allowing more energy from these sources to enter the receiver.

4.7 Summary

In this chapter, the theoretical development of space-time adaptive processing presented in Chapter 3 has been extended to include the effects of near-field scatterers. The near-field scatterers have no effect on the temporal steering vectors of the received signals; only the spatial steering vectors are affected. While the spatial steering vectors for the direct path of each signal have unit amplitude and a linear phase shift, the spatial steering vectors of the scattered signals have neither of

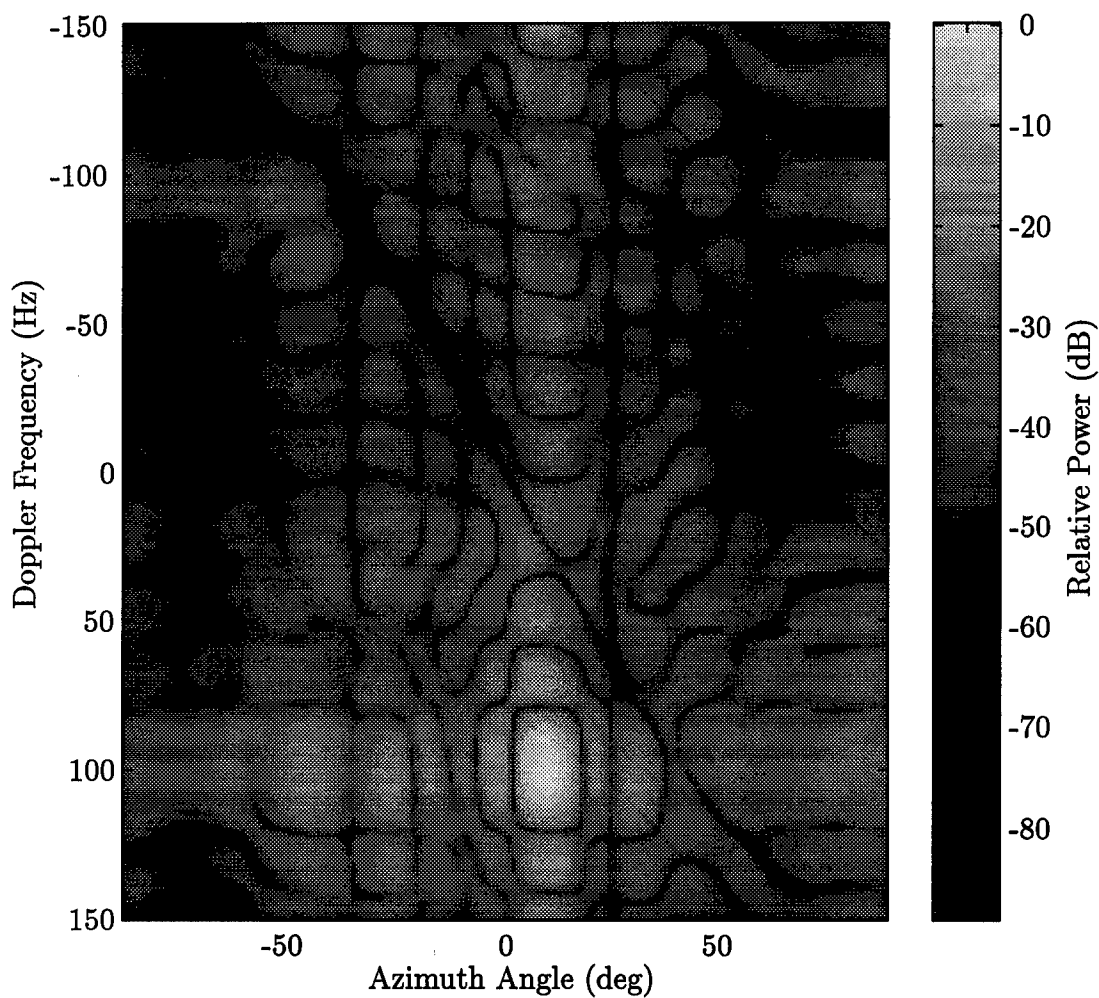


Figure 27 The adapted pattern for the same conditions as Fig. 21, with the addition of seven near-field scatterers, as illustrated in Fig. 24.

these qualities. Because each scatterer is a different distance from each element, the signals received by each element from a particular scatterer have a nonlinear phase progression. Also, since the scatterers are in the near-field of the array, the scattered wave must be treated as spherical, meaning the amplitude of the scattered signals received by each element is different.

To simplify the computations, signals which scatter off more than one near-field scatterer are ignored. For the path shown in Fig. 22(b), in which the signal bounces off the scatterer when returning to the array, the spatial steering vector is given by

$$\mathbf{d}_{ts}^- = [d_{t0s}^-; d_{t1s}^-; \cdots; d_{t(N-1)s}^-],$$

where

$$d_{tns}^- = a_{tns}^- e^{-j\frac{2\pi}{\lambda_0}(l_{ns}-l'_{ts})} e^{j\psi_d},$$

a_{tns} is the ratio of the amplitude of the direct path target signal to the scattered path target signal from the s th scatterer to the n th element, l_{ns} is the distance from the n th element to the s th scatterer, and l'_{ts} is the length of the projection of l_{ns} onto the target vector. The spatial steering vector of the signal which bounces off the scatterer before going to the target is given by

$$\mathbf{d}_{ts}^+ = [d_{t0s}^+; d_{t1s}^+; \cdots; d_{t(N-1)s}^+],$$

where

$$d_{tns}^+ = e^{jn2\pi\vartheta_t} e^{j\psi_d} \sum_{p=0}^{N-1} a_{tps} e^{-j\frac{2\pi}{\lambda_0}(l_{ps}-l'_{ts})} e^{-jp2\pi\vartheta_t}.$$

The total spatial steering vector for the target signal is the sum of the spatial steering vectors for the direct path and scattered paths for all the scatterers

$$\tilde{\mathbf{a}}_t = \mathbf{a}_t + \sum_{s=0}^{S-1} (\mathbf{d}_{ts}^- + \mathbf{d}_{ts}^+)$$

this expression is then used to compute the space-time steering vector and space-time snapshot of the target signal as in Chapter 3,

$$\tilde{\mathbf{v}}_t = \mathbf{b}_t \otimes \tilde{\mathbf{a}}_t.$$

The scattered jammer signal has the same form as the target signal which bounced off the scatterer while returning from the target. The components of the spatial steering vector of the scattered jammer signal are given by

$$d_{jns}^- = a_{jns}^- e^{-j\frac{2\pi}{\lambda_0}(l_{ns}-l'_{js})} e^{j\psi_d},$$

where a_{jns}^- and l'_{js} have the same form as for the target signal, but using the direction to the jammer. The total jammer steering vector is found by summing \mathbf{d}_{js}^- over all the scatterers and adding the direct path steering vector,

$$\tilde{\mathbf{a}}_j = \mathbf{a}_j + \sum_{s=0}^{S-1} \mathbf{d}_{js}^-.$$

The jammer covariance matrix is computed in the same manner as in Chapter 3, but using $\tilde{\mathbf{a}}_j$ in place of \mathbf{a}_j ,

$$\tilde{\mathbf{R}}_j = \mathbf{I}_M \otimes (\tilde{\mathbf{A}}_j \mathbf{\Xi}_j \tilde{\mathbf{A}}_j^H)$$

where $\tilde{\mathbf{A}}_j = [\tilde{\mathbf{a}}_1, \tilde{\mathbf{a}}_2, \dots, \tilde{\mathbf{a}}_J]$.

The steering vectors for the scattered clutter returns from the k th clutter patch have the same form as the target return,

$$\begin{aligned} d_{kns}^- &= a_{kns}^- e^{-j\frac{2\pi}{\lambda_0}(l_{ns}-l'_{ks})} e^{j\psi_d} \\ d_{kns}^+ &= e^{jn2\pi\vartheta_k} e^{j\psi_d} \sum_{p=0}^{N-1} a_{kps}^+ e^{-j\frac{2\pi}{\lambda_0}(l_{ps}-l'_{ks})} e^{jp2\pi\vartheta_k}. \end{aligned}$$

The total spatial steering vector for the k th clutter patch is the sum of the direct path steering vector with the sum of the scattered path steering vectors for all the scatterers,

$$\tilde{\mathbf{a}}_k = \mathbf{a}_k + \sum_{s=0}^{S-1} (\mathbf{d}_{ks}^- + \mathbf{d}_{ks}^+).$$

The total spatial steering vector for the k th clutter patch becomes

$$\tilde{\mathbf{v}}_k = \mathbf{b}_k \otimes \tilde{\mathbf{a}}_k,$$

and the clutter covariance can be computed as

$$\tilde{\mathbf{R}}_c = \tilde{\mathbf{V}}_t \Xi_c \tilde{\mathbf{V}}_c^H,$$

where $\tilde{\mathbf{V}}_c = [\tilde{\mathbf{v}}_1, \tilde{\mathbf{v}}_2, \dots, \tilde{\mathbf{v}}_{N_c}]$.

The total covariance matrix of the undesired signals is the sum of these two covariance matrices with the noise covariance matrix,

$$\tilde{\mathbf{R}}_u = \tilde{\mathbf{R}}_j + \tilde{\mathbf{R}}_c + \mathbf{R}_n.$$

The optimum weight vector, adapted antenna pattern, and SINR can be computed using these quantities,

$$\begin{aligned} \tilde{\mathbf{w}} &= \tilde{\mathbf{R}}_u^{-1} \tilde{\mathbf{v}}_t \\ P_{\tilde{\mathbf{w}}}(\vartheta, \varpi) &= |\tilde{\mathbf{w}}^H \tilde{\mathbf{v}}(\vartheta, \varpi)|^2 \\ SINR &= \xi_t \tilde{\mathbf{v}}_t^H \tilde{\mathbf{R}}_u^{-1} \tilde{\mathbf{v}}_t. \end{aligned}$$

V. Results

5.1 Test Plan

To determine the effects of the near-field scatterers on space-time adaptive processing, several test cases were examined. The number of scatterers varied from two to fifteen and the RCS of the scatterers varied from 0.01 to 0.5 m². Six different orientations were used, which are shown in Fig. 28. For orientations A through E, the scatterers are linearly spaced between the endpoints. Orientation F is similar to orientation A, but the positions of the scatterers are allowed to vary by ± 0.1 m in both the x and y directions. Table 4 describes the orientations in more detail. In all cases, the positions of the scatterers are with respect to the left end of the array.

5.2 Results

5.2.1 No External Interference. For the first three sets of figures, the jammer and clutter signals were ignored. In the absence of external interference, the signal-to-noise ratio (SNR) does not depend on the Doppler frequency.

Figures 29 through 32 show how changing the RCS of the scatterers affects the SNR. The scatterers were arranged in orientation A. Figure 29 shows the SNR as a function of azimuth angle and scatterer RCS for five near-field scatterers. The

Table 4 Definition of orientations

Orientation	Location of first scatterer (x_1, y_1) (m)	Location of second scatterer (x_2, y_2) (m)
A	$(0, 1)$	$(l^a, 1)$
B	$(l/2, 1)$	$(l/2, l + 1)$
C	$(0, 1)$	$(0, l)$
D	$(0, 1)$	$(l, l + 1)$
E	$(0, 1)$	$(l, l/2 + 1)$
F	$(0 \pm 0.1, 1 \pm 0.1)$	$(l \pm 0.1, l + 1 \pm 0.1)$

^a l is the length of the array

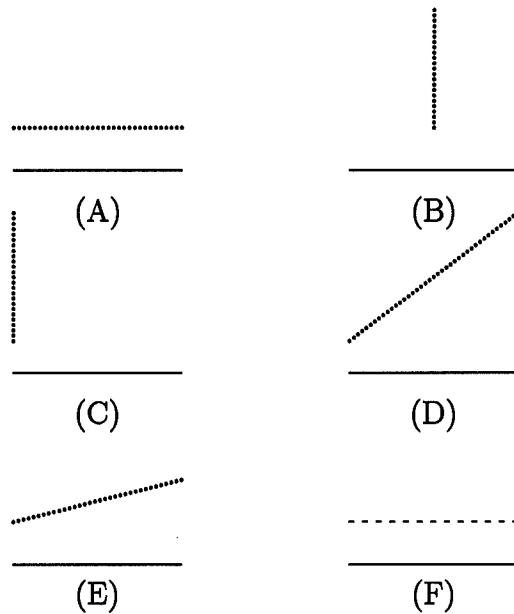


Figure 28 Near-field scatterer orientations.

SNR decreases as the scatterer RCS increases, but tends to flatten out as more scatterers are added. For larger numbers of scatterers, the SNR increases as the size of the scatterers increases. The increase in SNR is due to the larger scatterers reflecting more target energy into the array. Figures 30 through 32 show the SNR as a function of azimuth angle and scatterer RCS for seven, eight, and fifteen scatterers respectively.

The notch at 0° in Fig. 31 is due to the fact that each NFS is directly in front of an antenna element. Since the NFS imposes a 180° phase shift on the signal, the signal from a scatterer to the element directly behind it will be 180° out of phase with the direct path signal. The sum of this scattered signal with the direct path signal reduces the apparent amplitude of the direct path signal entering the element. Because only eight of the fifteen elements are affected, a target at 0° appears to produce a wavefront with an amplitude which varies with position. This effect is shown in Fig. 33. This problem does not occur with 15 scatterers because the signal at each element is reduced by the same amount.

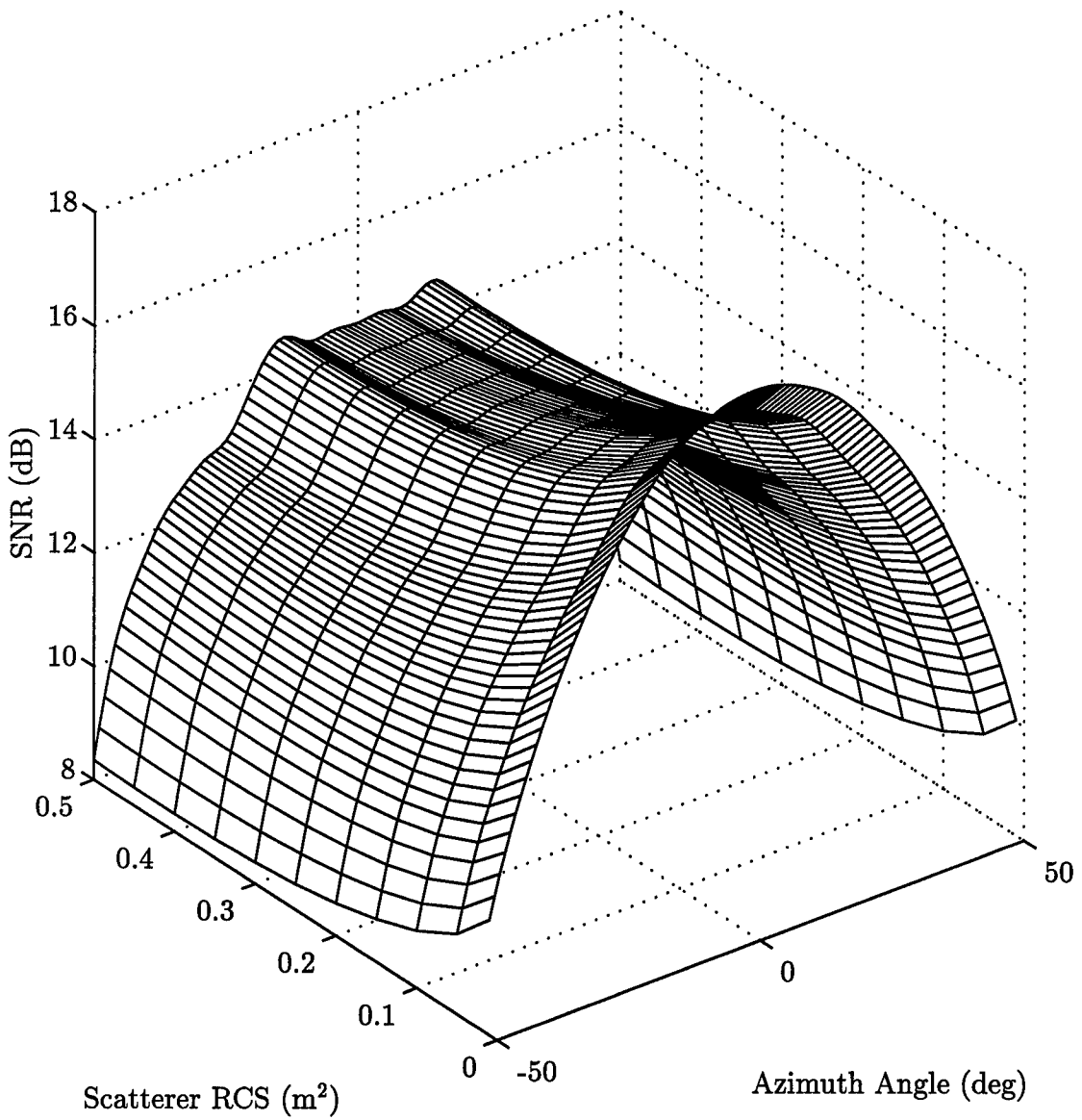


Figure 29 SNR as a function of azimuth angle and scatterer RCS for 5 NFS, orientation A.

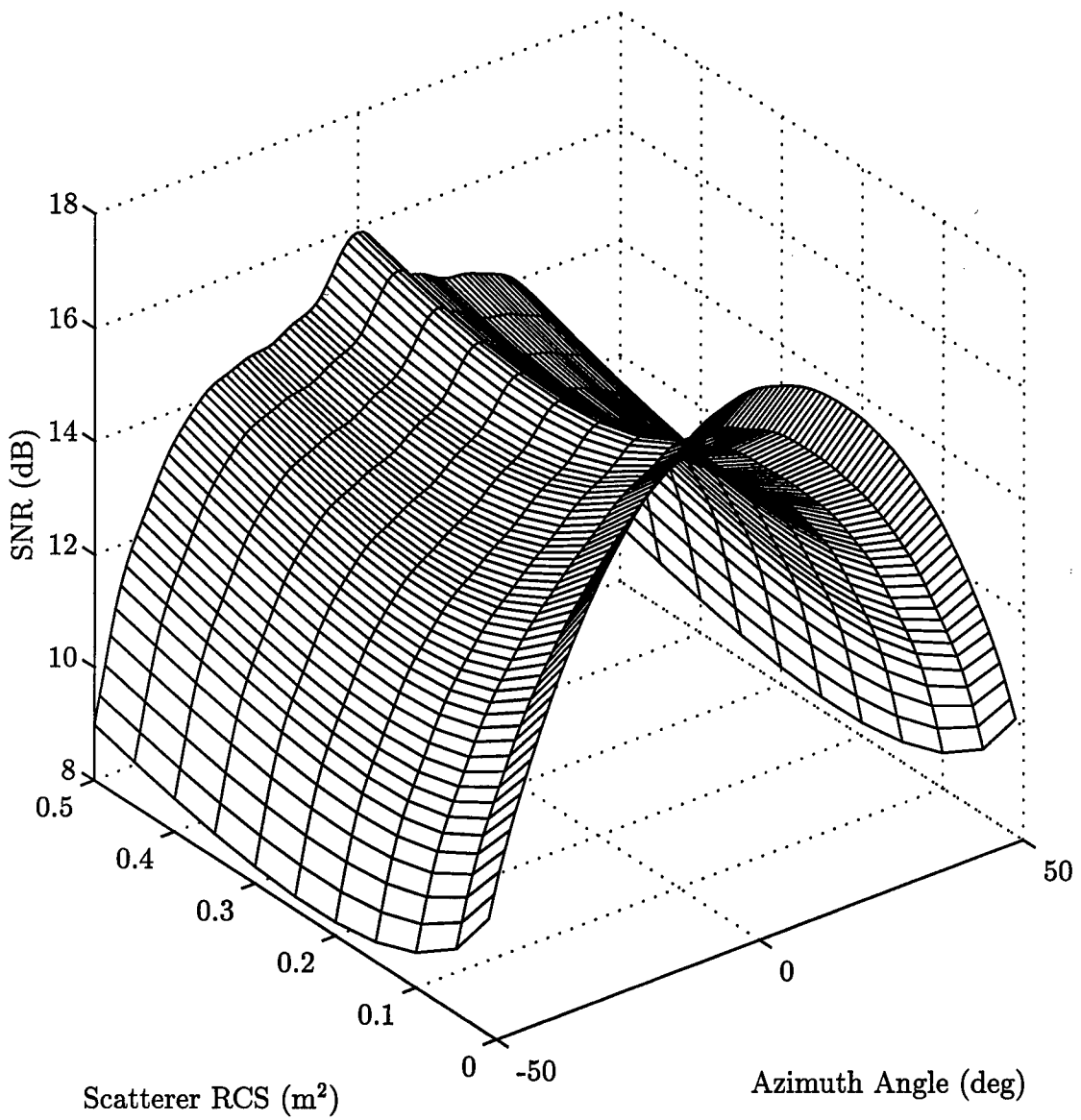


Figure 30 SNR as a function of azimuth angle and scatterer RCS for 7 NFS, orientation A.

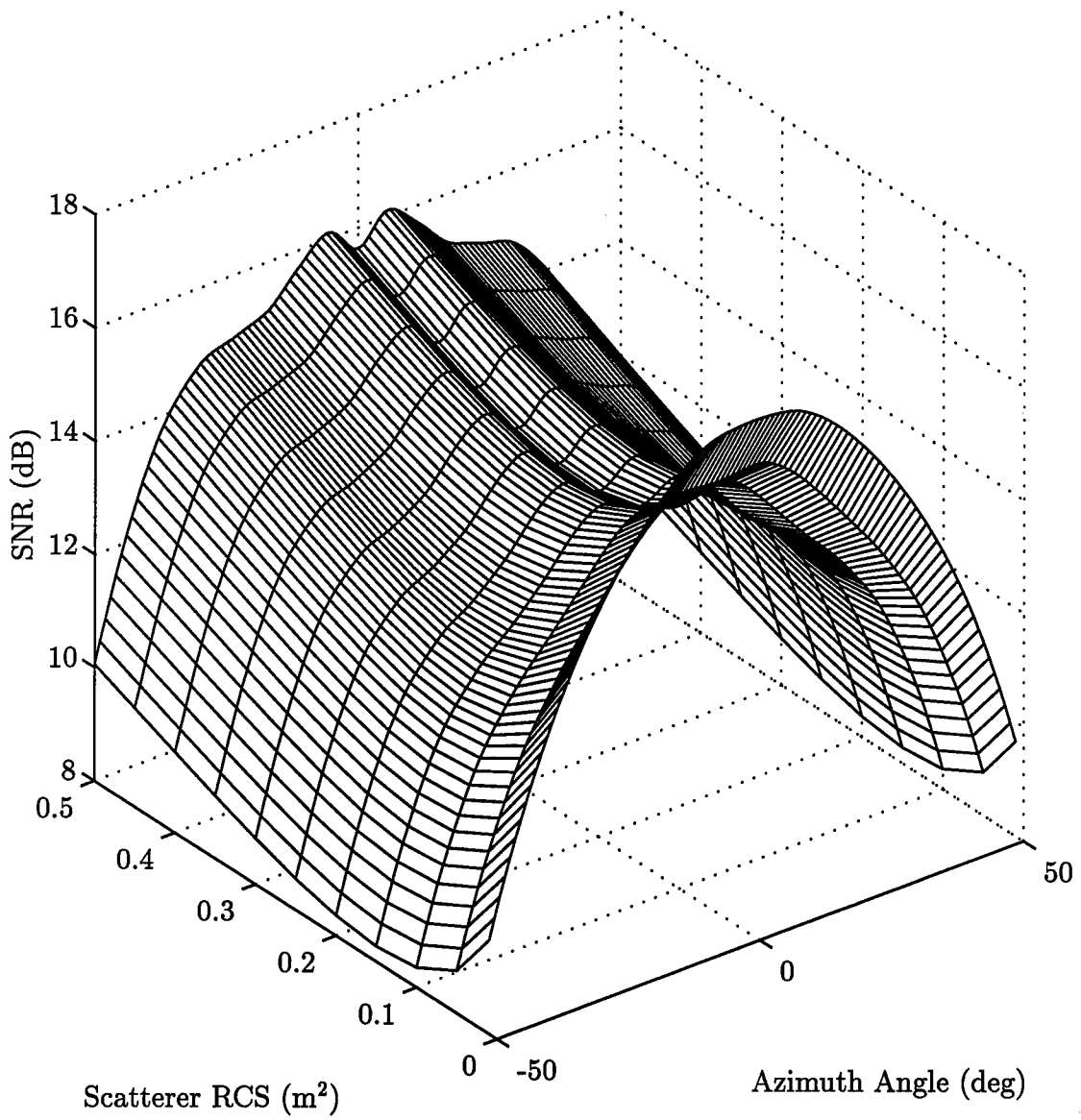


Figure 31 SNR as a function of azimuth angle and scatterer RCS for 8 NFS, orientation A.

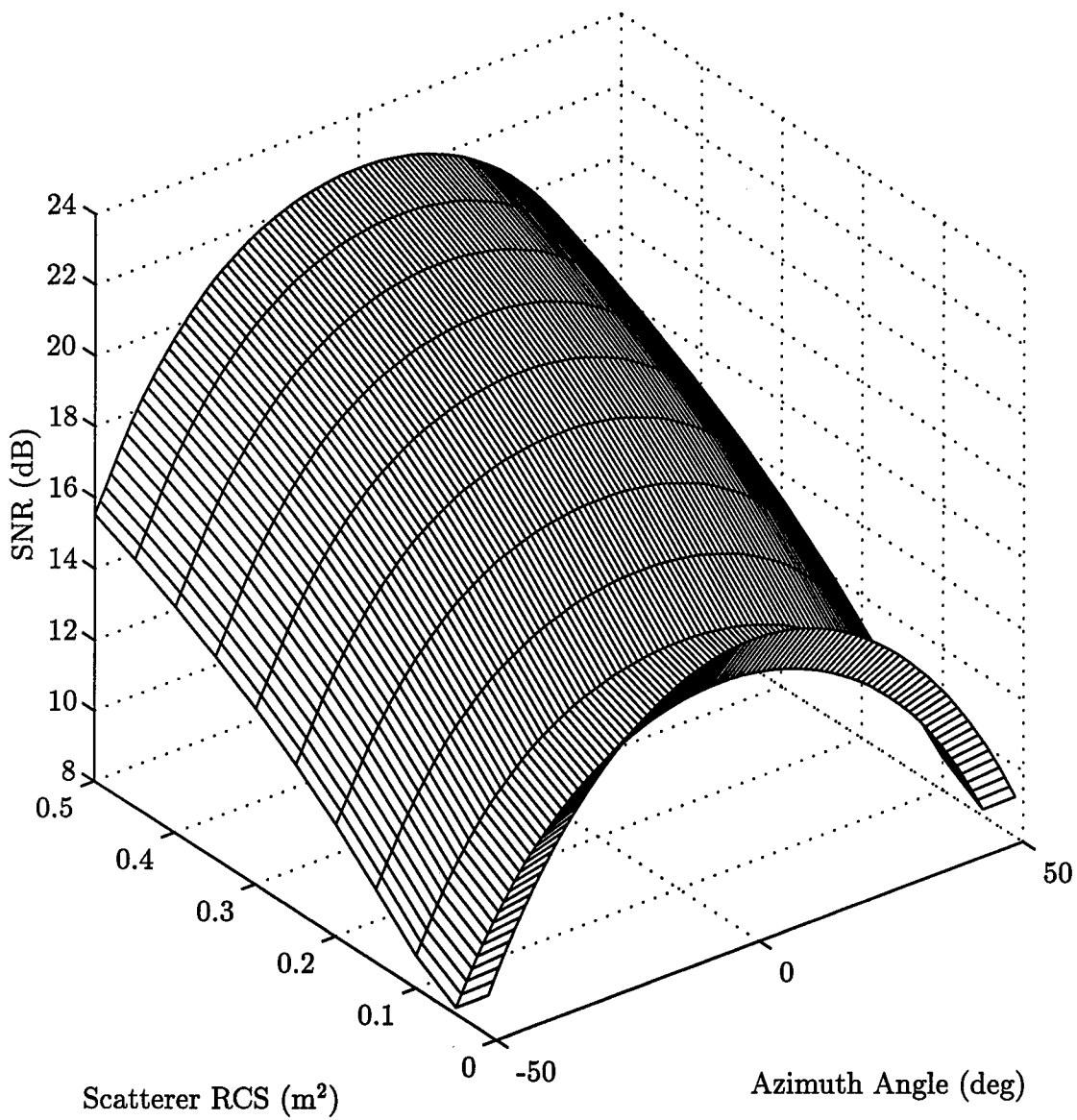


Figure 32 SNR as a function of azimuth angle and scatterer RCS for 15 NFS, orientation A.

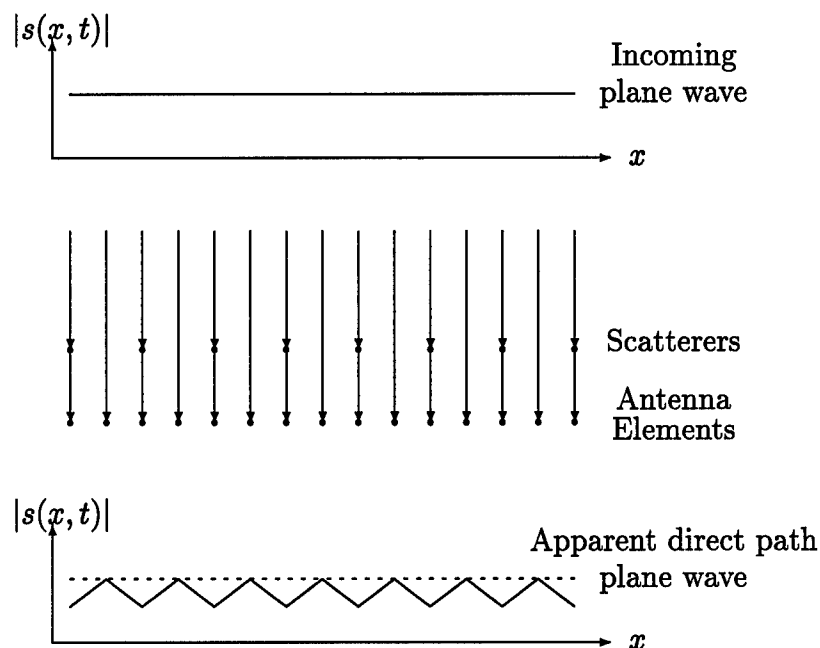


Figure 33 Effect of eight NFS on the direct-path wavefront perceived by a fifteen element array.

Figures 34 through 39 show how changing the number and orientation of the scatterers affects the SNR. For each orientation in Table 4, the target angle was varied from -50° to $+50^\circ$ and the number of scatterers was varied from zero to fifteen. The scatterer RCS was held constant at 0.5 m^2 . For orientation A, shown in Fig. 34, the SNR decreases until the number of scatterers, S , reaches five, at which point the SNR begins to increase. At $S = 10$, the SNR is at the same level as for no scatterers. The SNR for orientation B is shown in Fig. 35. The minimum SNR occurs at $S = 7$, and the SNR returns to the same level as with no scatterers at $S = 13$.

Figure 36 shows the SNR for orientation C. For target angles greater than 20° , the scatterers have almost no effect on the SNR because the scattered waves do not enter the array from the same direction as the direct path wave. For targets to the left of the array, the scatterers affect the SNR in a manner similar to that of

orientation B. The SNR decreases as the number of scatterers increases from zero to seven, then increases as the the number of scatterers continues to increase.

Figures 37 and 38 show the SNR plots for orientations D and E. As the angle between the scatterers and the array decreases, the SNR plot more closely resembles that of Fig. 34 for orientation A. Figure 39 shows the SNR for orientation F. The plot is very similar to Fig. 34, indicating the precise spacing of the scatterers has less effect on the SNR than their number and general configuration.

Figures 40 through 42 show the adapted pattern as a function of azimuth angle at the target Doppler for different numbers of scatterers and a scatterer RCS of 0.5 m^2 . Figure 40 shows the adapted azimuth antenna patterns for a target at 0° , 100 Hz, and various numbers of scatterers. Fig. 41 is for a target at 20° , and Fig. 42 is for a target at 40° . The shape of the mainbeam and first two side lobes is not significantly affected by the scatterers. The remaining side lobes, however, show some significant distortion, especially for the cases of five, seven, eight, and ten scatterers. The scatterers are spaced more than $\lambda/2$ apart, and the criterion to avoid spatial frequency aliasing given in Eqn. (20) is not met. The large grating lobes, such as in Fig. 42 at -20° for eight scatterers, are the result of this spatial undersampling. For $S = 15$, the side lobes are lower than for the case of no scatterers.

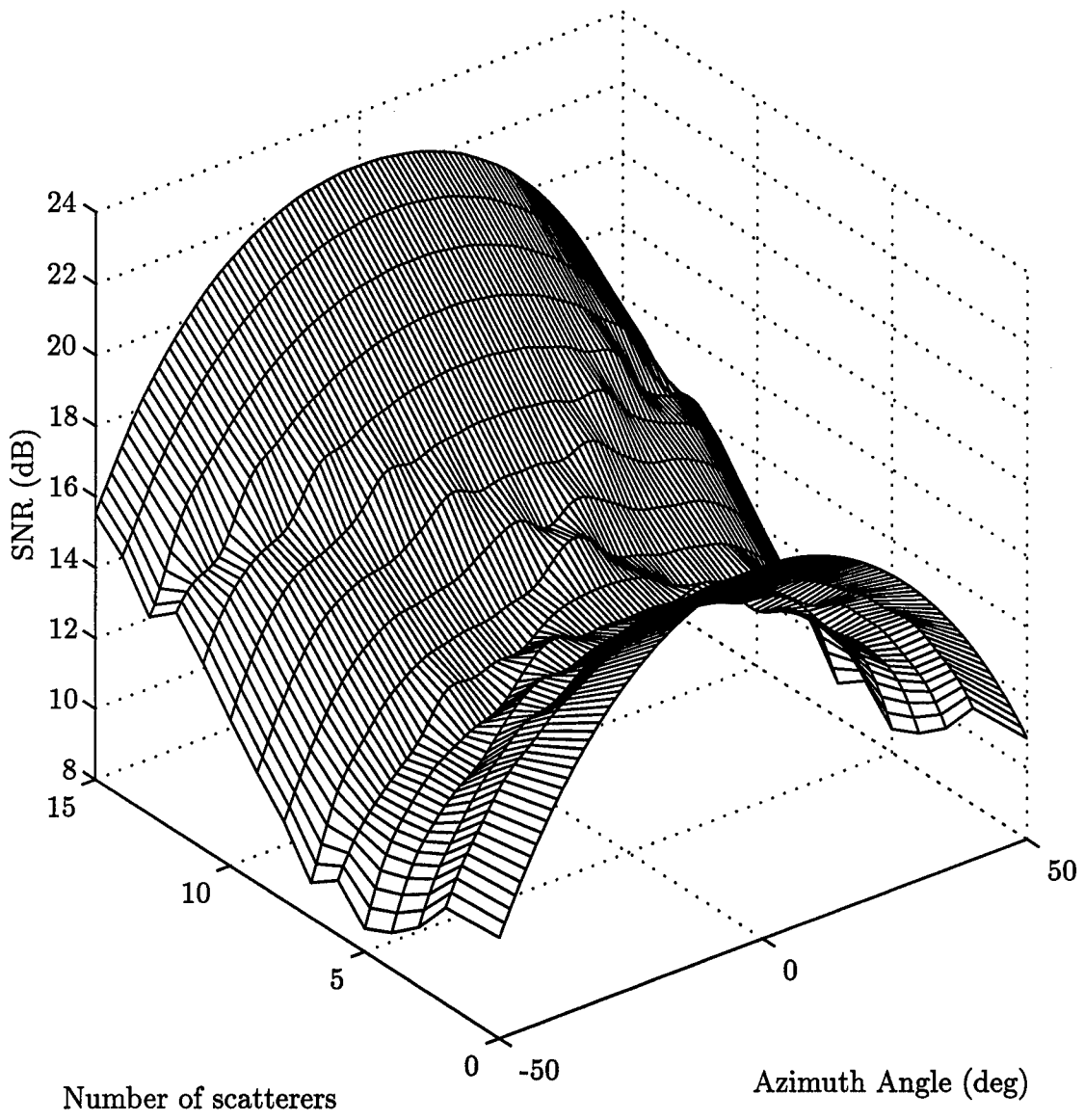


Figure 34 Signal-to-noise ratio as a function of azimuth angle and number of scatterers using orientation A and $\sigma_s = 0.5 \text{ m}^2$.

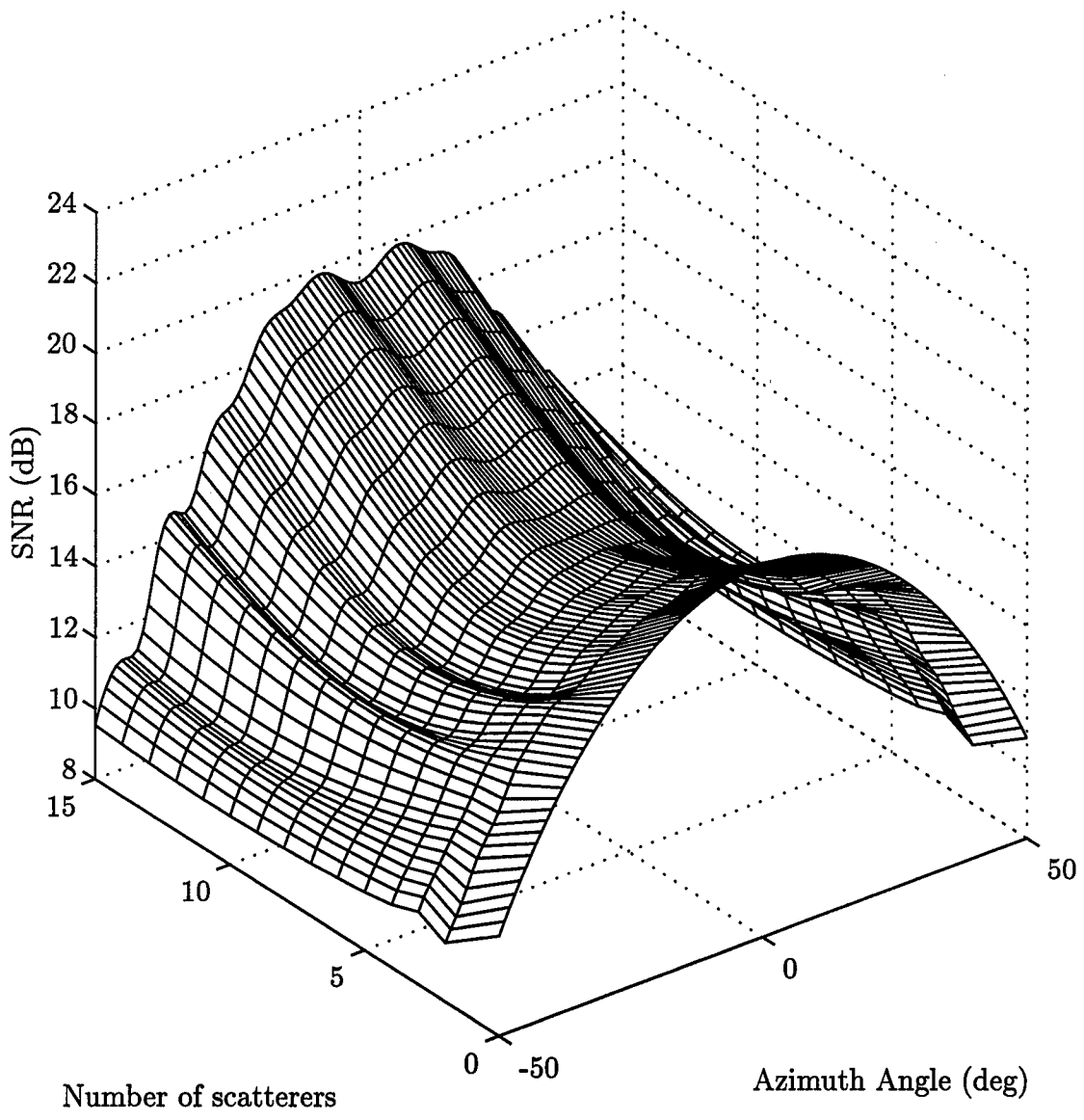


Figure 35 Signal-to-noise ratio as a function of azimuth angle and number of scatterers using orientation B and $\sigma_s = 0.5 \text{ m}^2$.

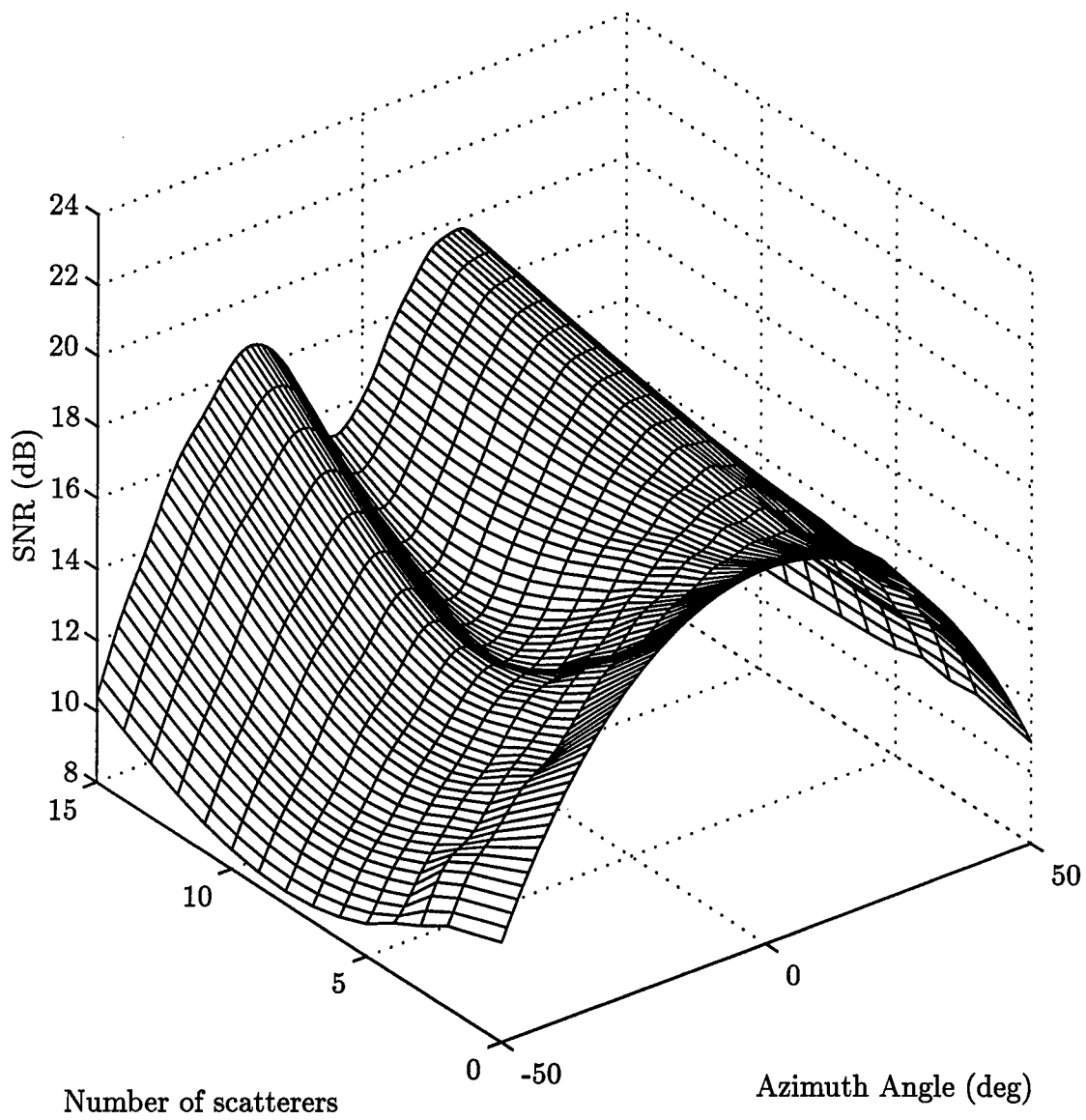


Figure 36 Signal-to-noise ratio as a function of azimuth angle and number of scatterers using orientation C and $\sigma_s = 0.5 \text{ m}^2$.

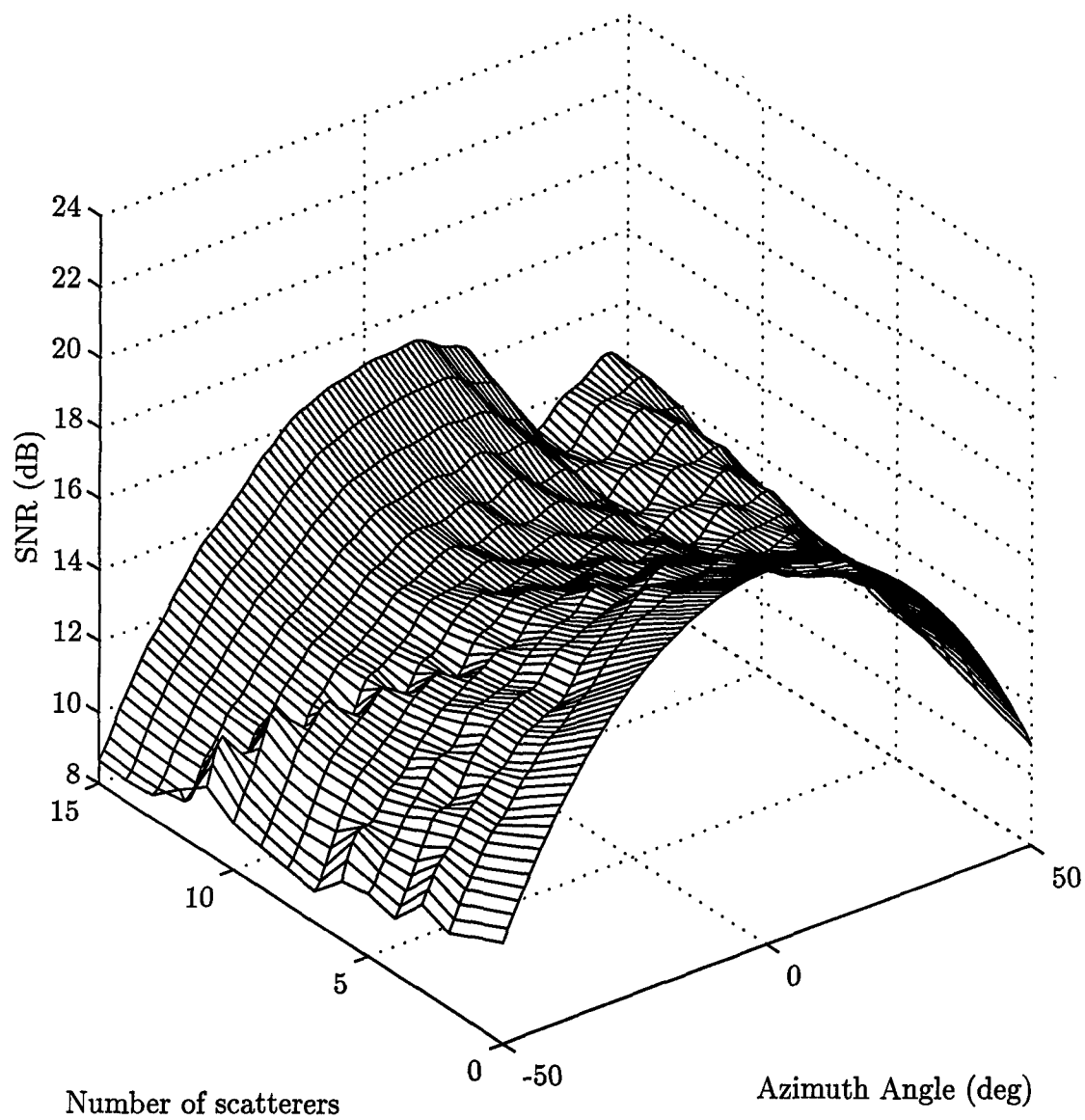


Figure 37 Signal-to-noise ratio as a function of azimuth angle and number of scatterers using orientation D and $\sigma_s = 0.5 \text{ m}^2$.

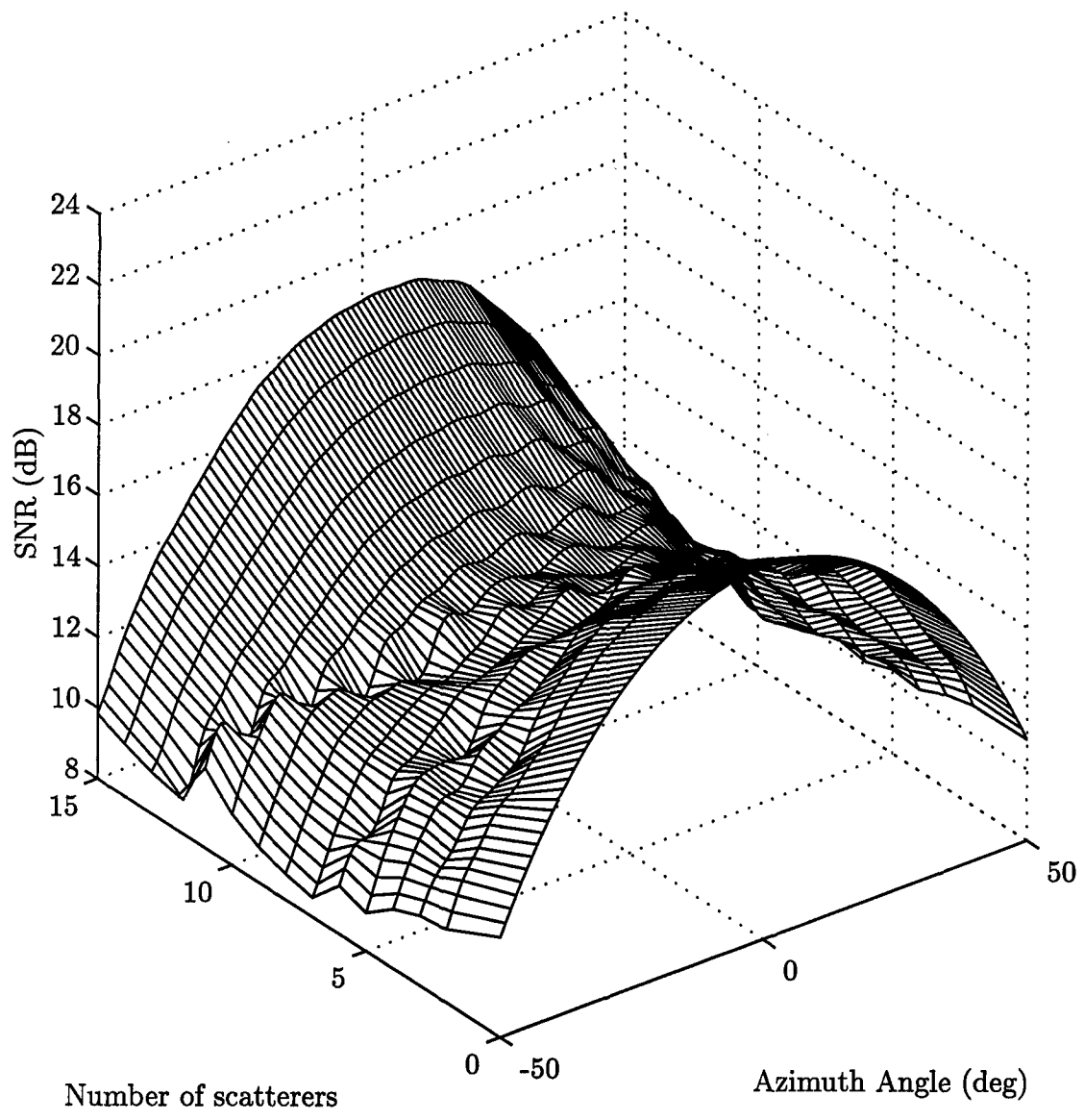


Figure 38 Signal-to-noise ratio as a function of azimuth angle and number of scatterers using orientation E and $\sigma_s = 0.5 \text{ m}^2$.

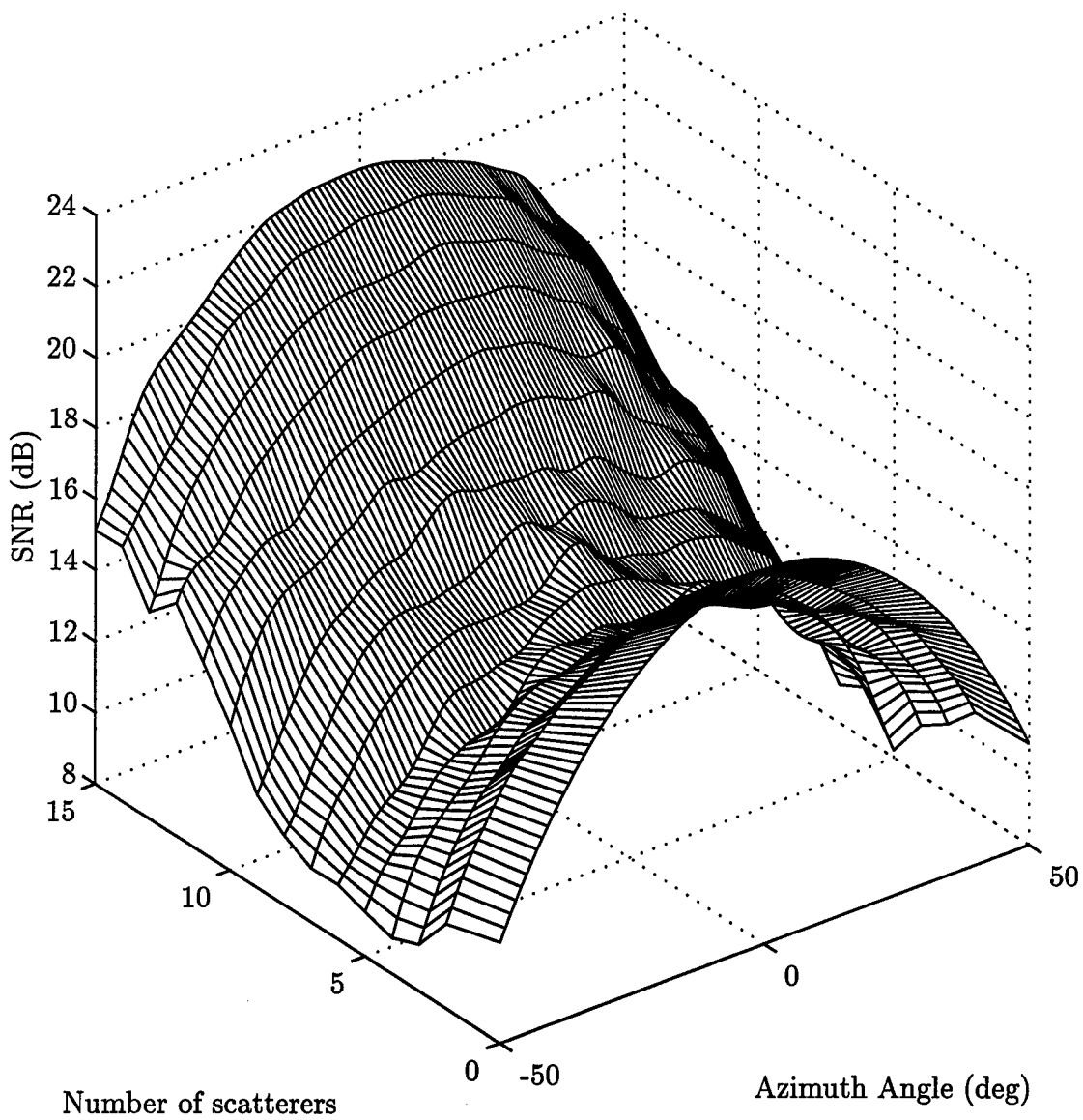


Figure 39 Signal-to-noise ratio as a function of azimuth angle and number of scatterers using orientation F and $\sigma_s = 0.5 \text{ m}^2$.

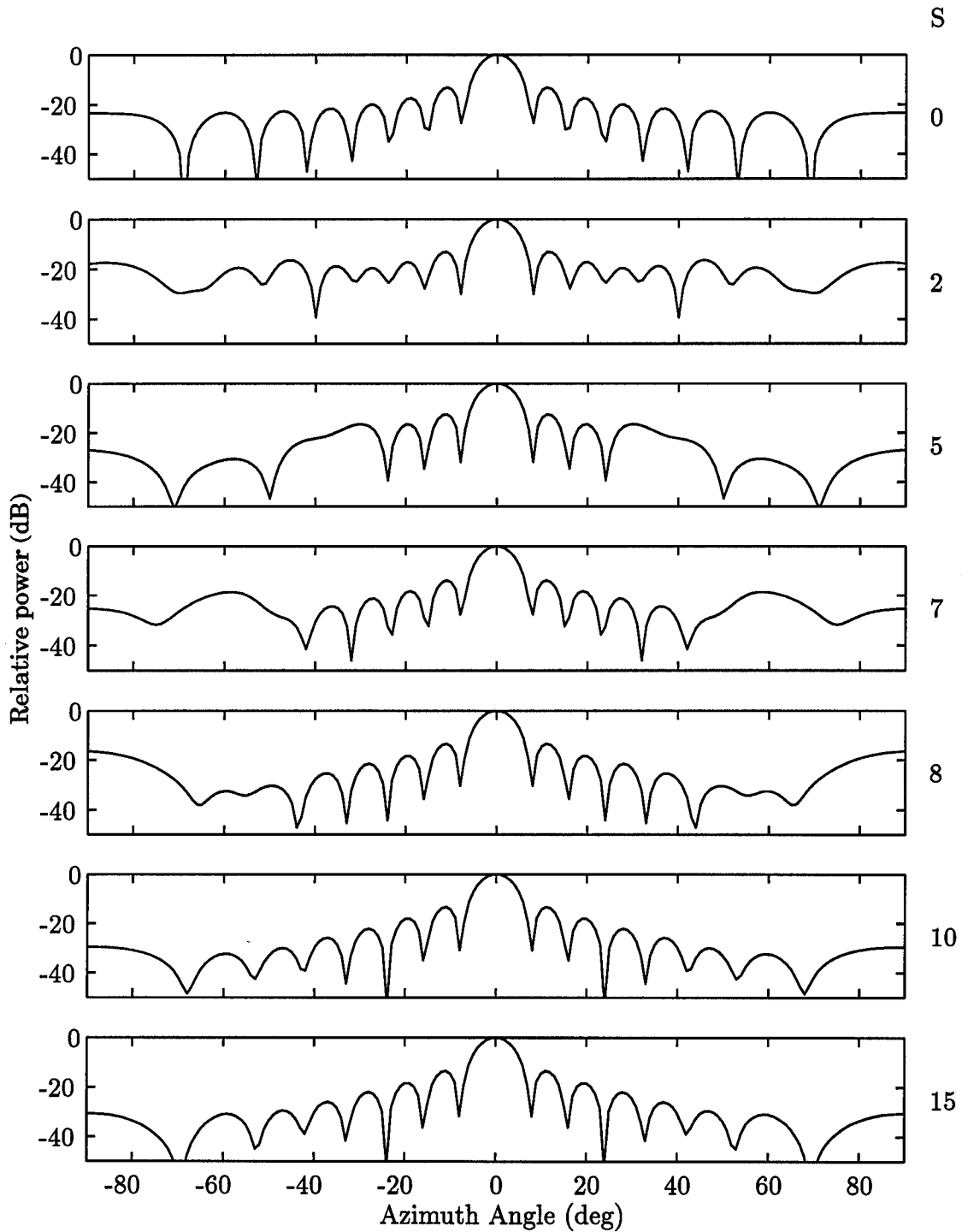


Figure 40 Adapted antenna pattern as a function of azimuth angle for a target at 0° , 100 Hz. The scatterers were placed in orientation A. The number of scatterers, S , is indicated at the right side of the plot.

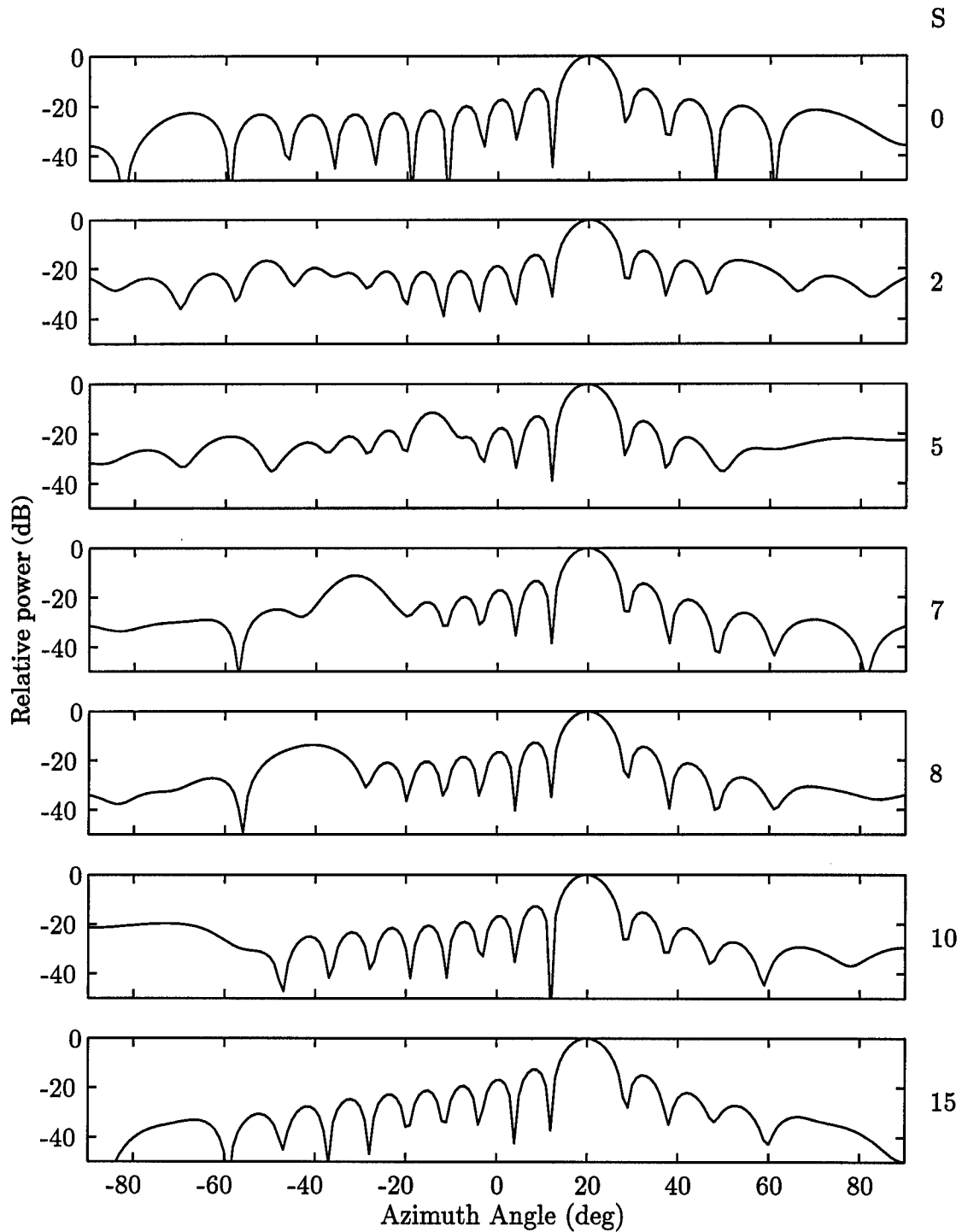


Figure 41 Adapted antenna pattern as a function of azimuth angle for a target at 20° , 100 Hz. The scatterers were placed in orientation A. The number of scatterers, S , is indicated at the right side of the plot.

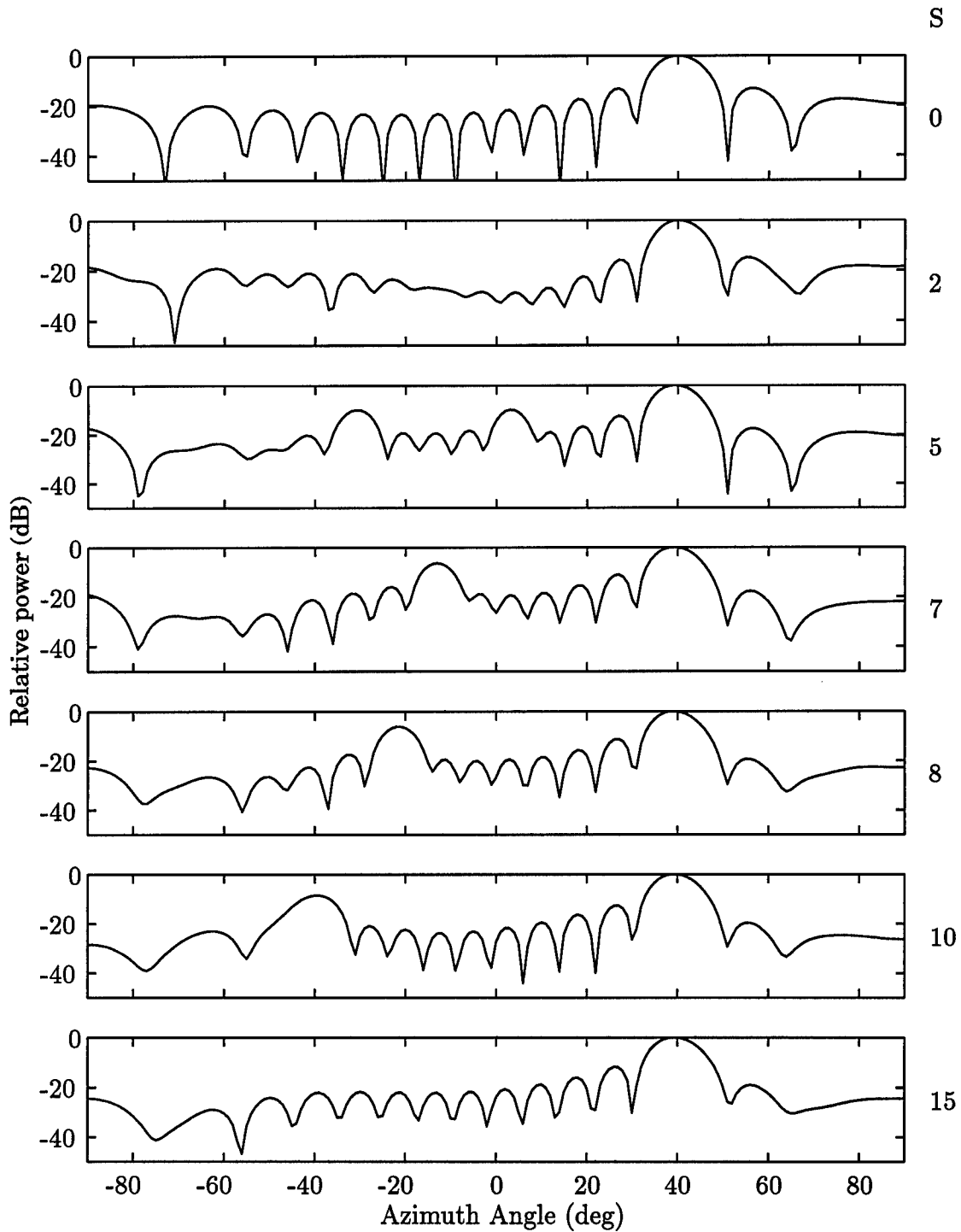


Figure 42 Adapted antenna pattern as a function of azimuth angle for a target at 40° , 100 Hz. The scatterers were placed in orientation A. The number of scatterers, S , is indicated at the right side of the plot.

Table 5 Rank of the clutter covariance matrix for each orientation and number of scatterers S .

S	Scatterer Orientation					
	A	B	C	D	E	F
2	82	83	83	84	84	82
3	83	90	90	92	90	87
4	86	94	93	100	95	91
5	87	96	96	105	99	93
6	87	96	97	108	101	95
7	86	95	97	109	103	95
8	84	94	97	108	102	96
9	87	95	98	111	103	97
10	86	95	97	113	104	98
11	85	95	96	112	104	98
12	85	94	95	110	104	97
13	85	94	95	110	104	97
14	82	93	95	110	103	98
15	79	90	94	108	103	96

5.2.2 *External Interference Present.* The following plots show the effects of the near-field scatterers on the adapted antenna pattern, signal-to-interference-plus-noise ratio (SINR), and the rank and eigenvalues of the clutter covariance matrix. The radar system, jammer, and clutter parameters used are the same as those listed in Table 2.

Table 5 shows the rank of the clutter covariance matrix for a target at 0° and each combination of orientation and number of scatterers. The rank indicates the number of degrees of freedom required to null out the clutter return. The two diagonal orientations, D and E, have the greatest effect on the rank of the clutter covariance matrix. Figure 43 shows the eigenvalues for each orientation with eight scatterers. In most cases, the highest rank occurred with between seven and ten scatterers. For comparison, the rank of the clutter covariance matrix with no near-field scatterers is 29. Increasing the scatterer RCS or the target angle had little effect on the rank.

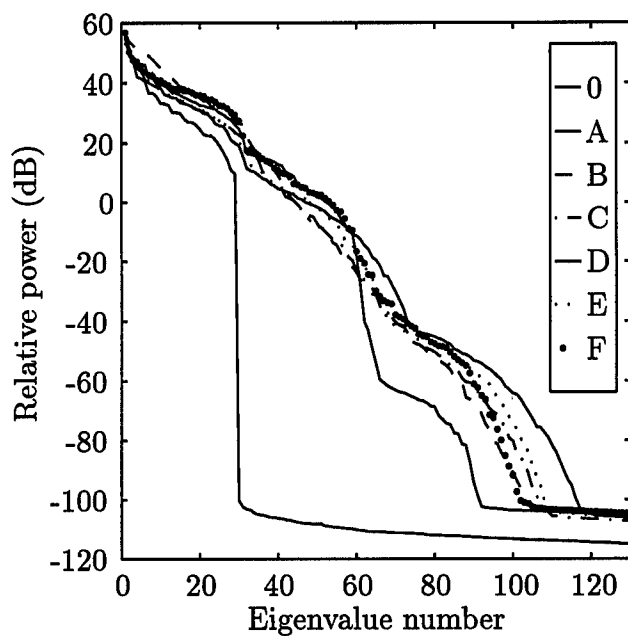


Figure 43 Eigenvalues of the clutter covariance matrix for different orientations of 8 scatterers, target at 0° , $\sigma_s = 0.5 \text{ m}^2$. The first solid line from the left represents the eigenvalues of the clutter covariance matrix with no scatterers, the second solid line is for orientation A, and the last solid line is for orientation D.

Figures 44 through 49 show the azimuth antenna pattern at the target Doppler for different orientations and numbers of scatterers. The target is at 20° , 100 Hz, and the scatterer RCS is $\sigma_s = 0.5 \text{ m}^2$. Appendix B contains the complete angle-Doppler patterns from which these figures were taken. The presence of clutter causes the SINR to be a function of Doppler frequency, as well as azimuth angle. Figures 50 through 55 show the corresponding SINR vs. Doppler plots. The large null at 50 Hz corresponds to the Doppler frequency of clutter at 20° . The smaller nulls, such as the one at -80 Hz for $S=5$ in Fig. 50, correspond to the Doppler frequencies of clutter entering the receiver through the grating lobes.

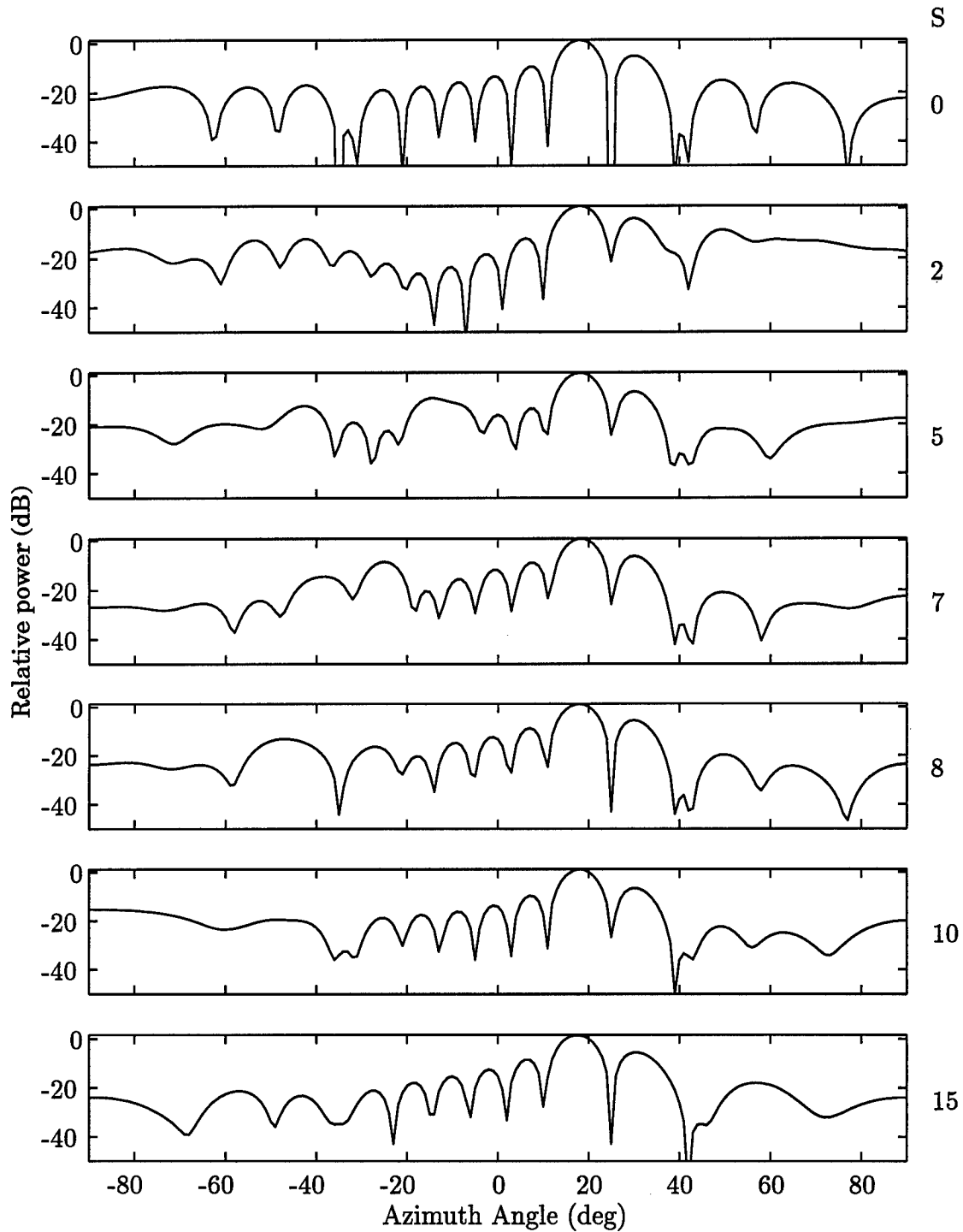


Figure 44 Adapted antenna pattern as a function of azimuth angle for a target at 20° , 100 Hz, scatterer orientation A. The number of scatterers, S , is indicated at the right side of the plot.

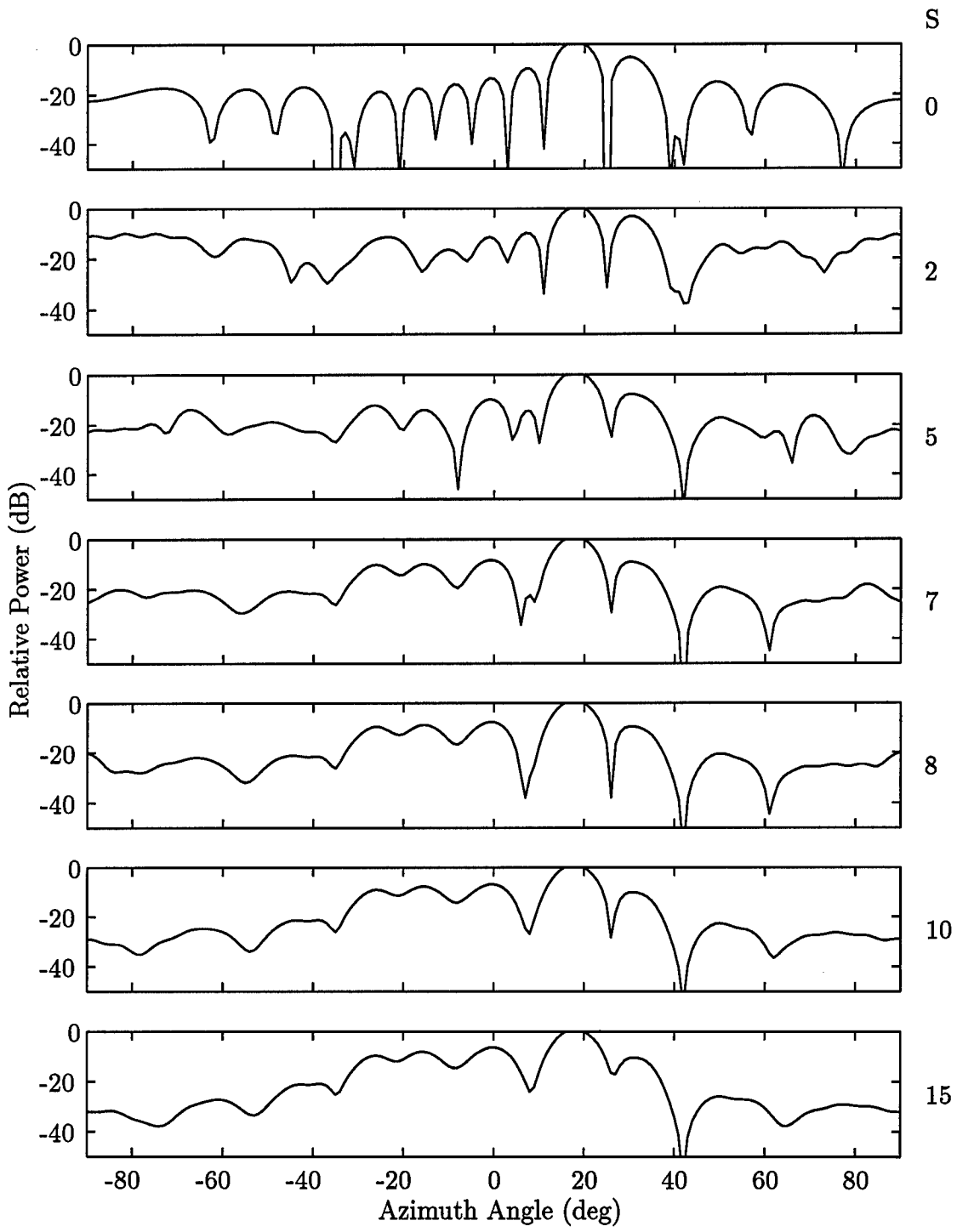


Figure 45 Adapted antenna pattern as a function of azimuth angle for a target at 20°, 100 Hz, scatterer orientation B. The number of scatterers, S , is indicated at the right side of the plot.

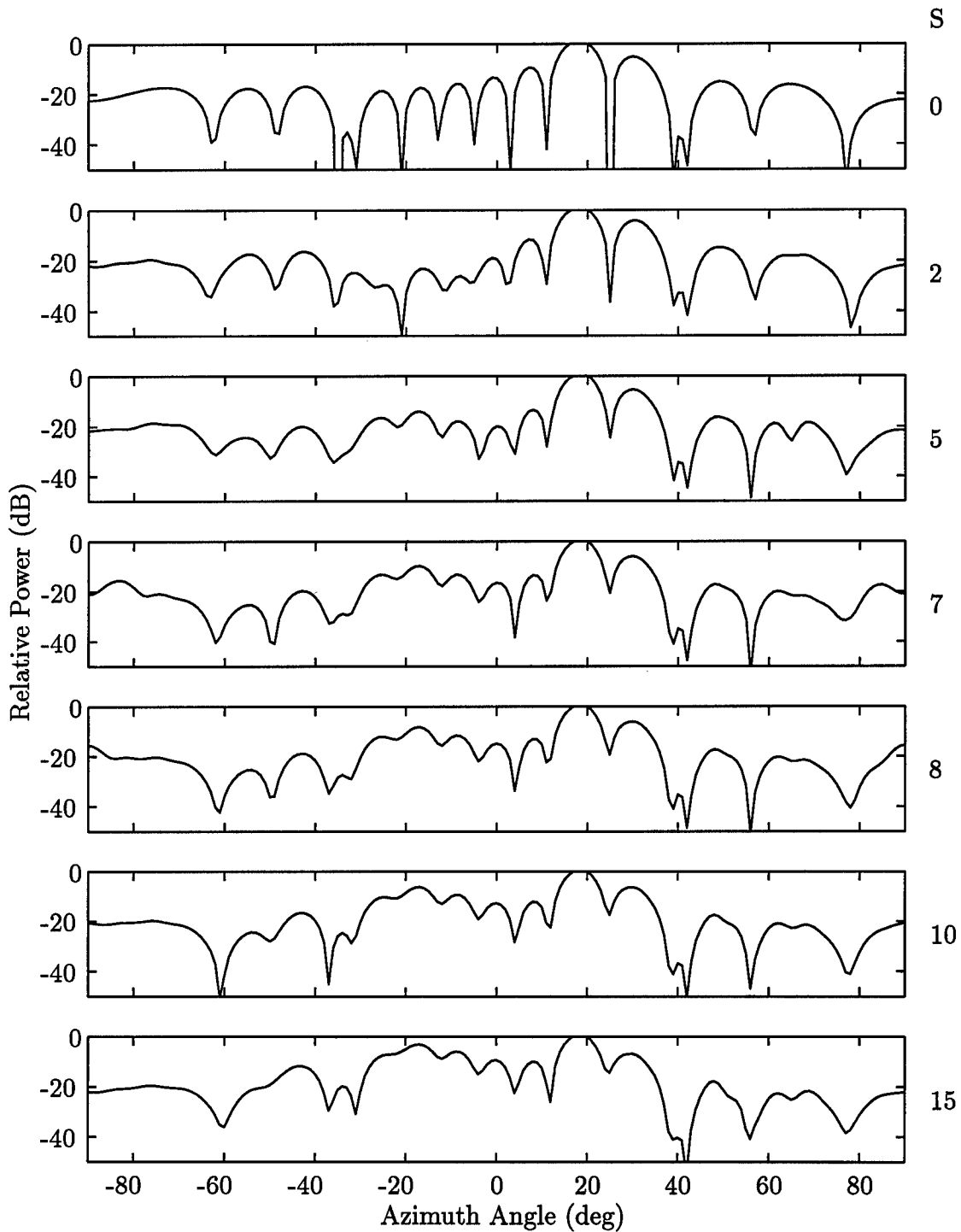


Figure 46 Adapted antenna pattern as a function of azimuth angle for a target at 20° , 100 Hz, scatterer orientation C. The number of scatterers, S , is indicated at the right side of the plot.

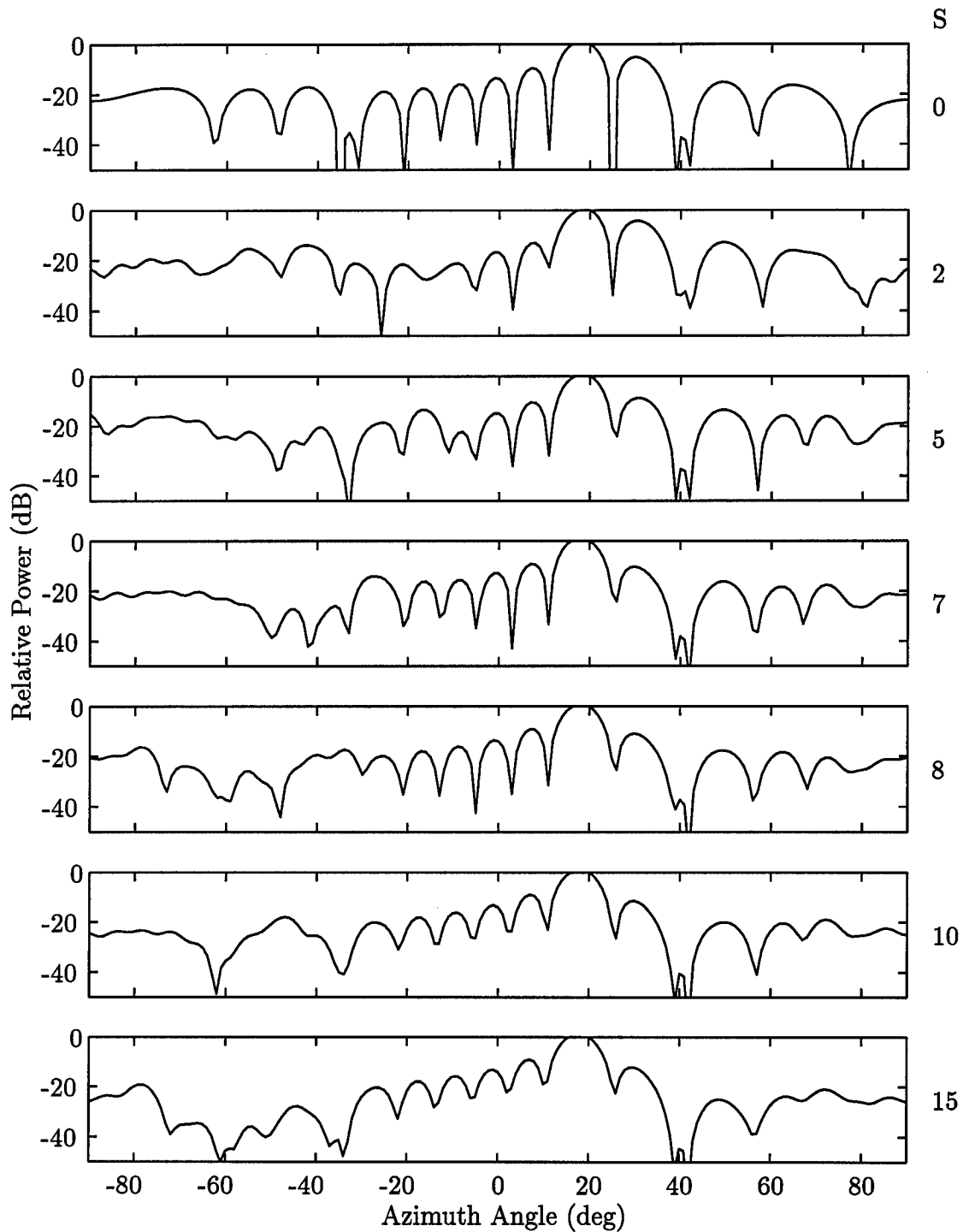


Figure 47 Adapted antenna pattern as a function of azimuth angle for a target at 20° , 100 Hz, scatterer orientation D. The number of scatterers, S , is indicated at the right side of the plot.

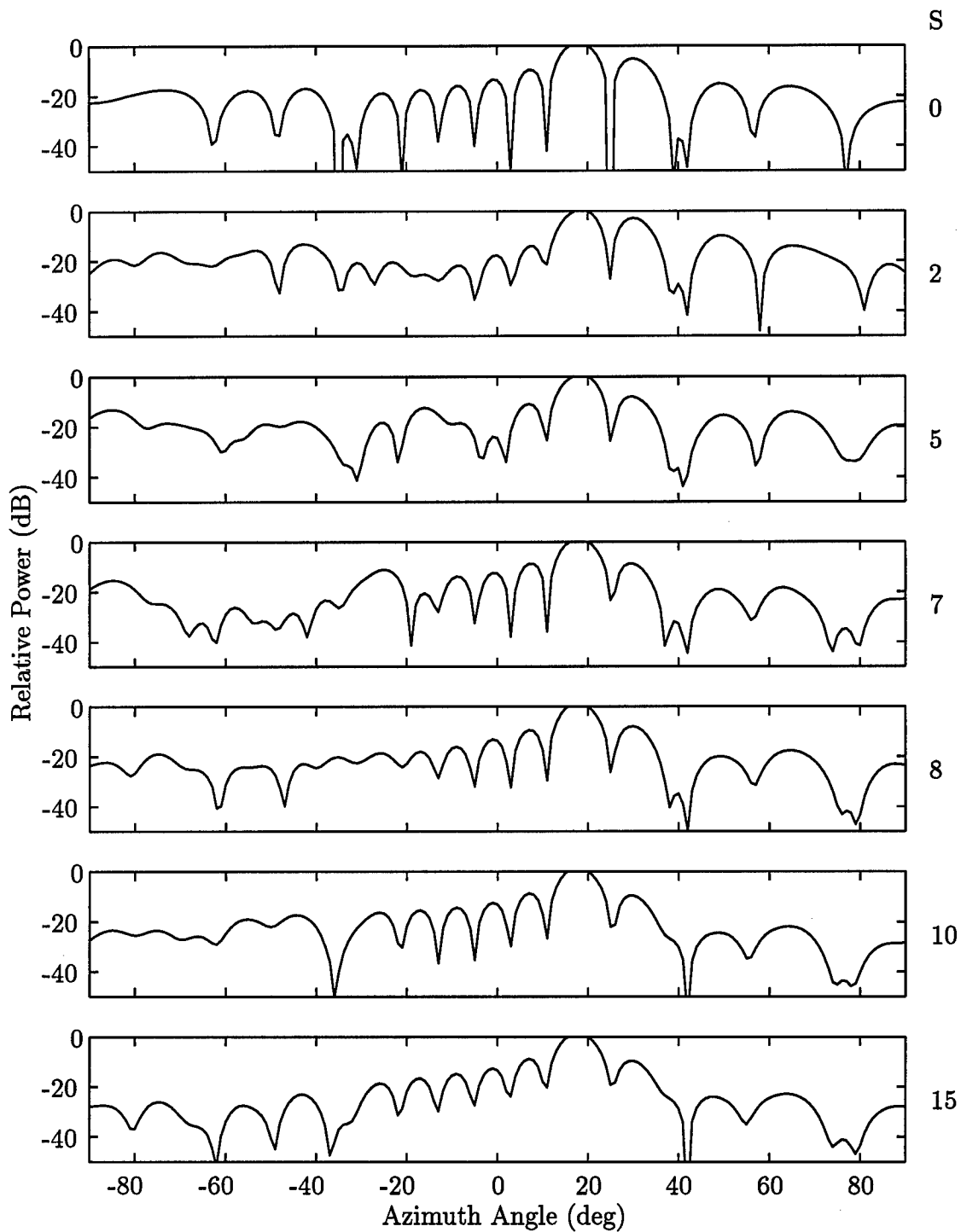


Figure 48 Adapted antenna pattern as a function of azimuth angle for a target at 20° , 100 Hz, scatterer orientation E. The number of scatterers, S , is indicated at the right side of the plot.

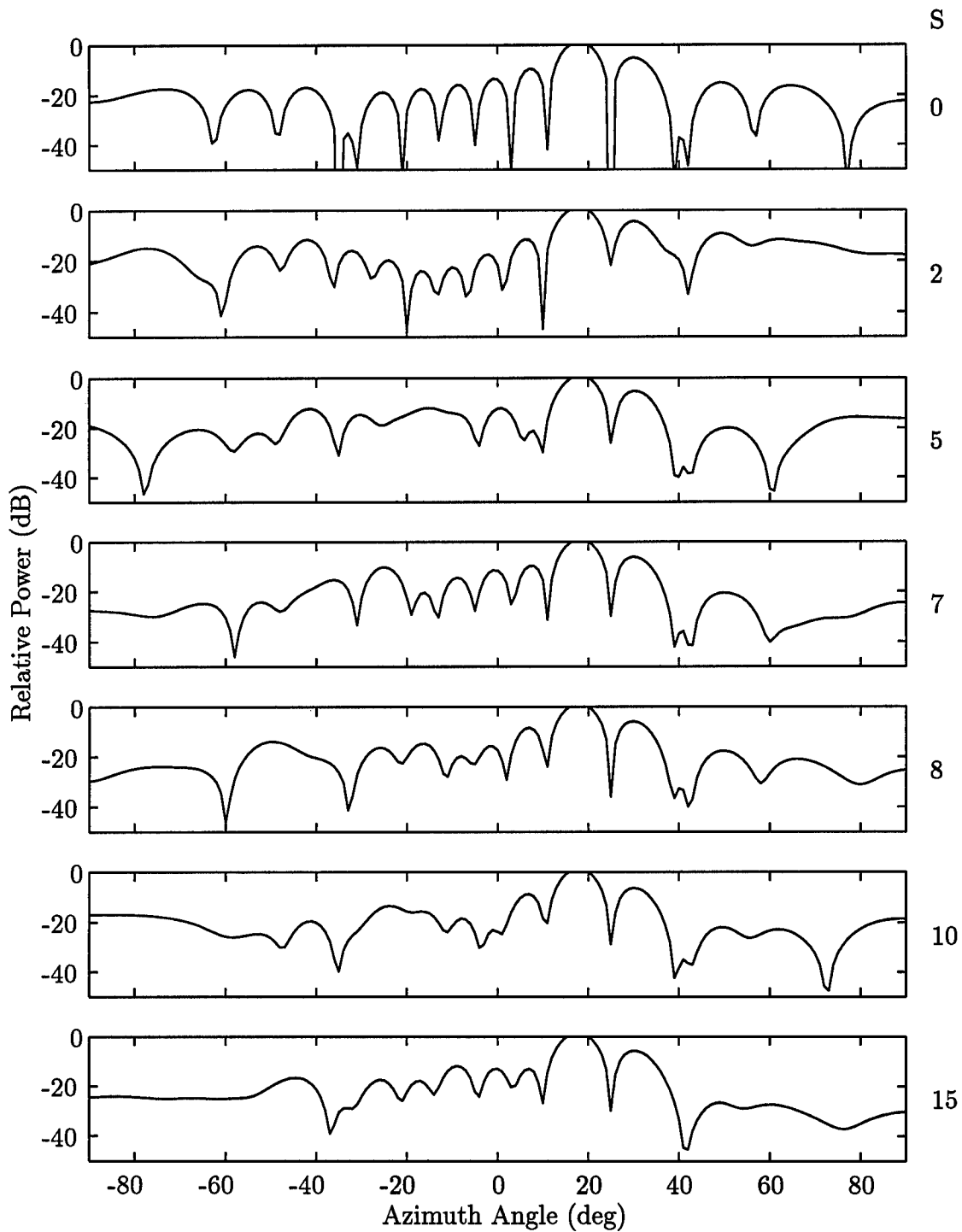


Figure 49 Adapted antenna pattern as a function of azimuth angle for a target at 20° , 100 Hz, scatterer orientation F. The number of scatterers, S , is indicated at the right side of the plot.

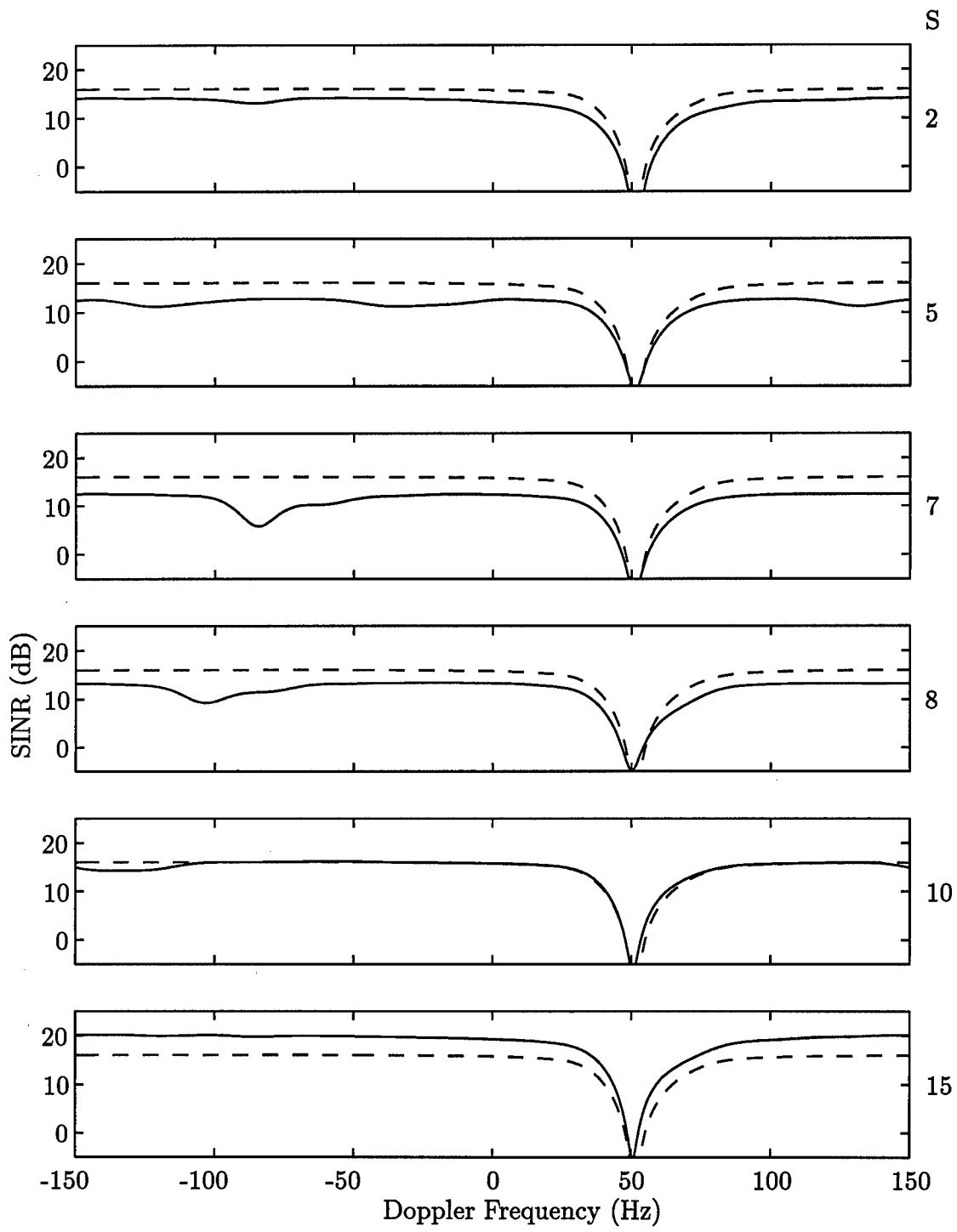


Figure 50 SINR as a function of Doppler frequency for a target at 20° , 100 Hz, scatterer orientation A. The number of scatterers, S , is indicated at the right side of the plot. The dashed line is the SINR with no scatterers.

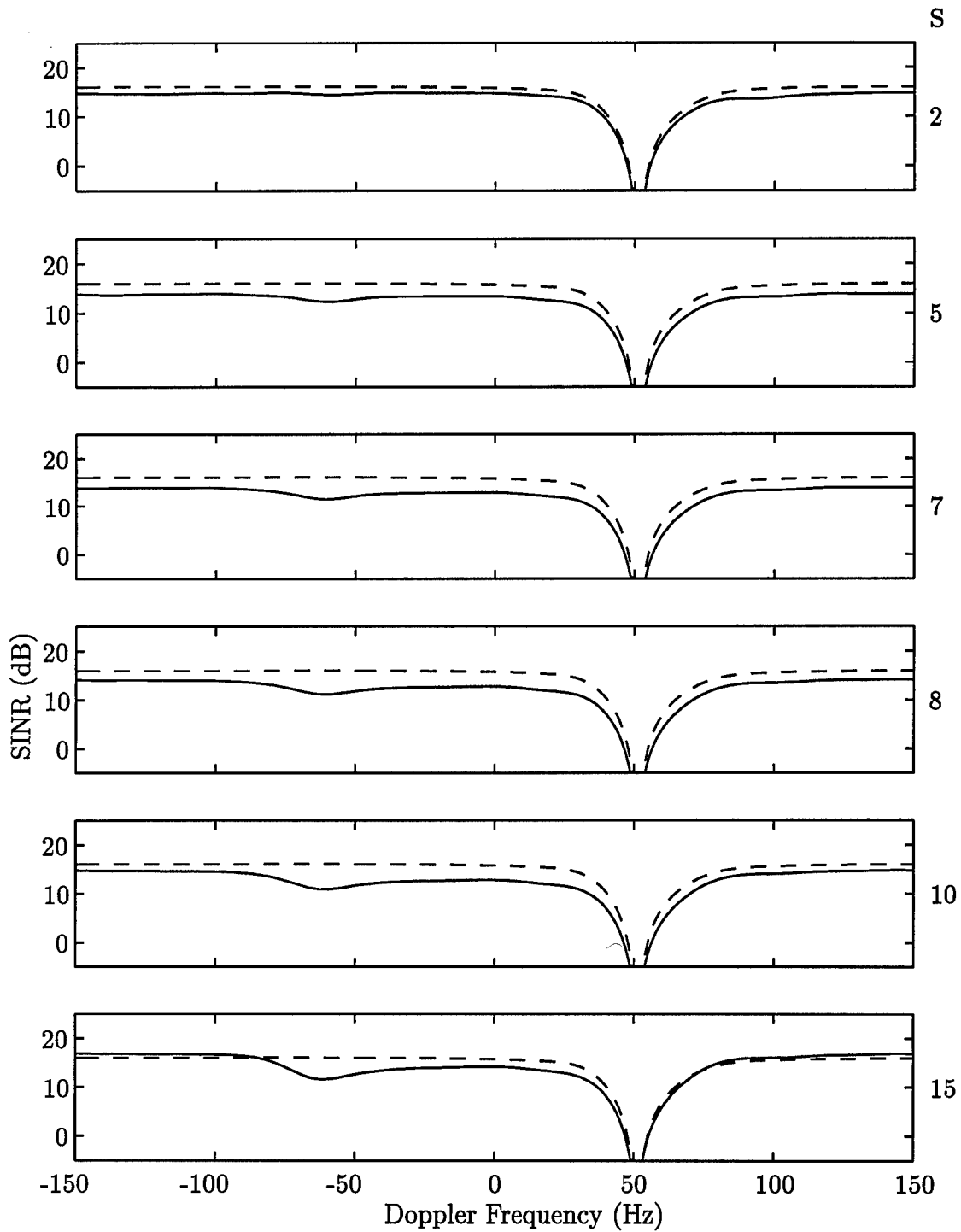


Figure 51 SINR as a function of Doppler frequency for a target at 20° , 100 Hz, scatterer orientation B. The number of scatterers, S , is indicated at the right side of the plot. The dashed line is the SINR with no scatterers.

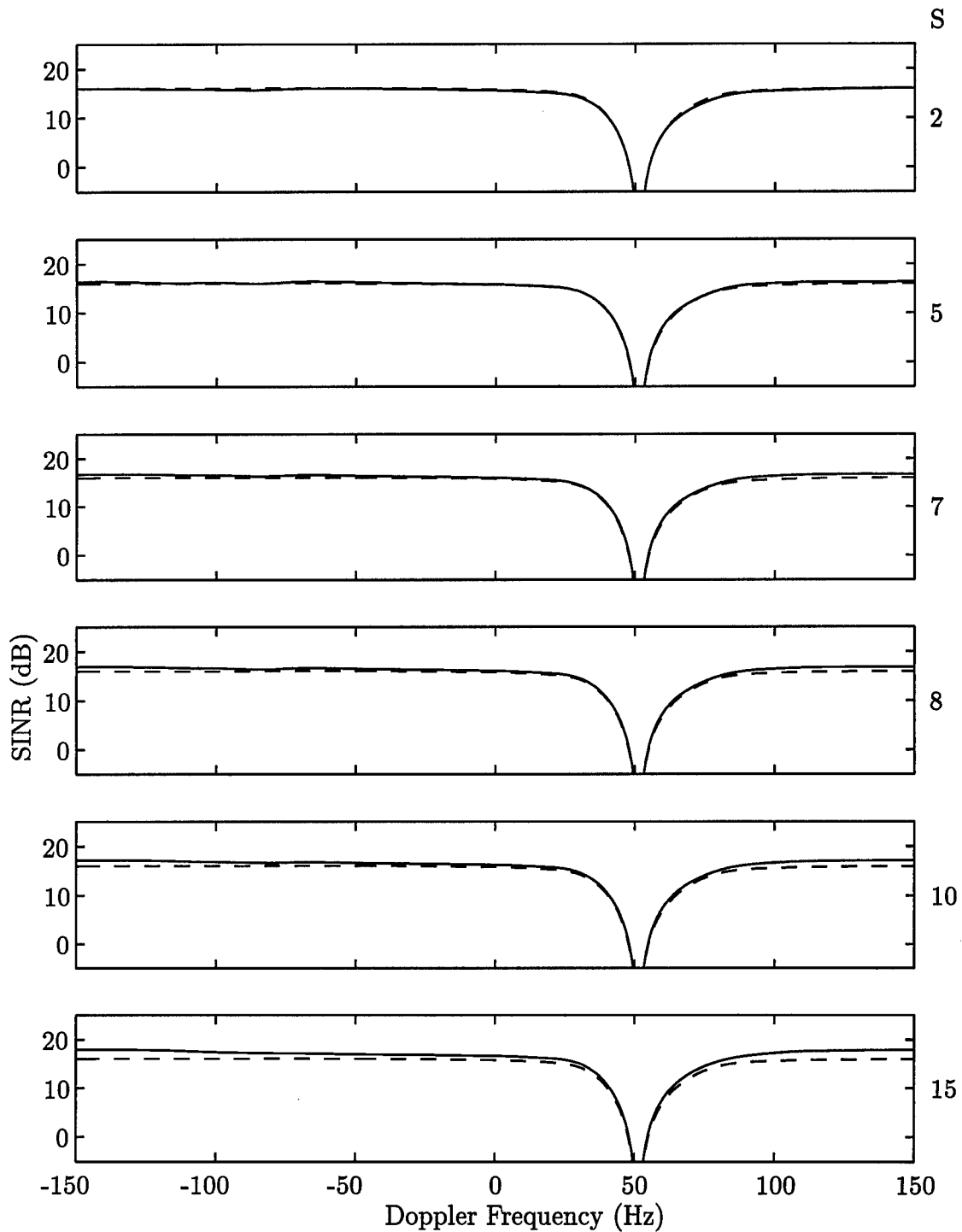


Figure 52 SINR as a function of Doppler frequency for a target at 20° , 100 Hz, scatterer orientation C. The number of scatterers, S , is indicated at the right side of the plot. The dashed line is the SINR with no scatterers.

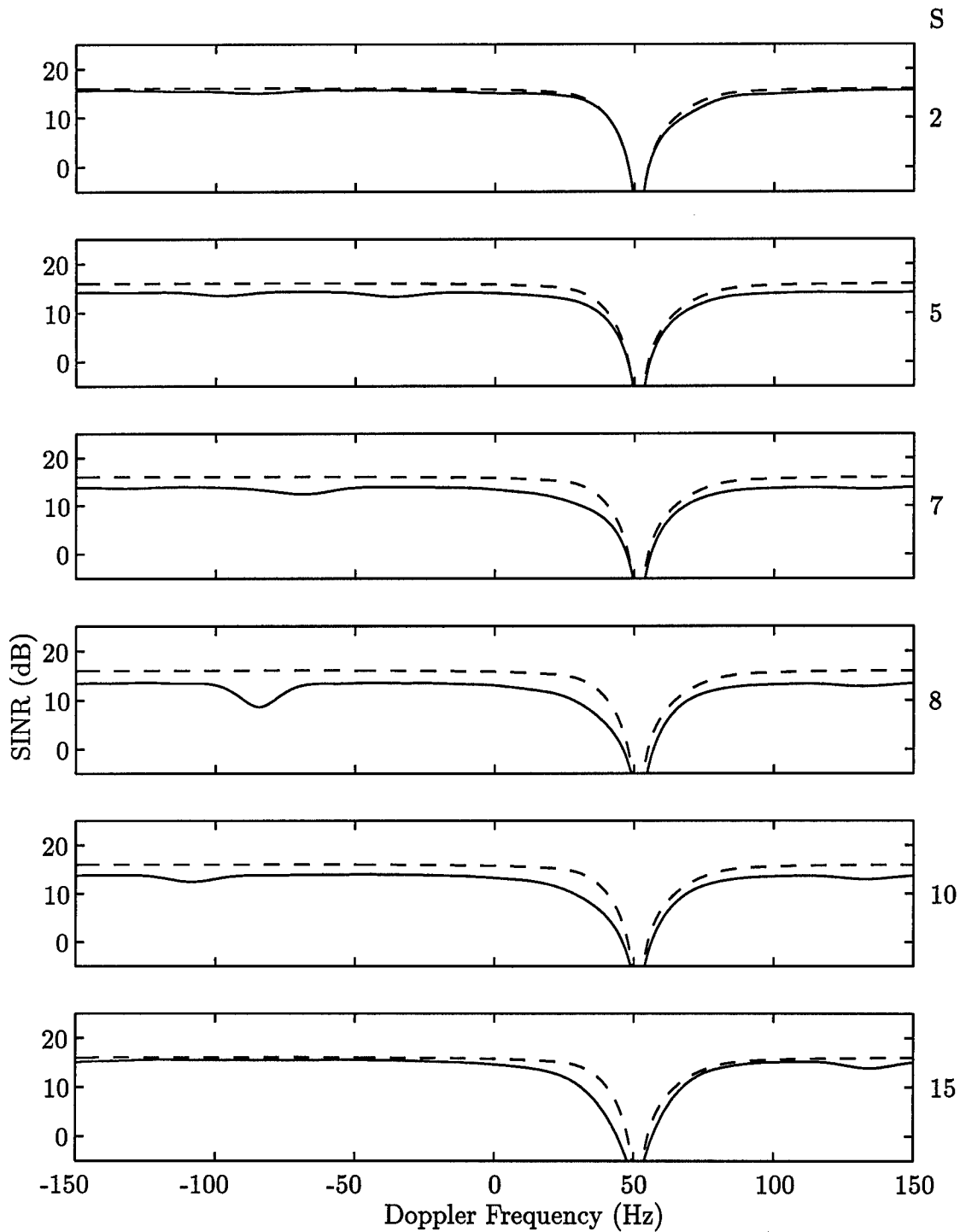


Figure 53 SINR as a function of Doppler frequency for a target at 20° , 100 Hz, scatterer orientation D. The number of scatterers, S , is indicated at the right side of the plot. The dashed line is the SINR with no scatterers.

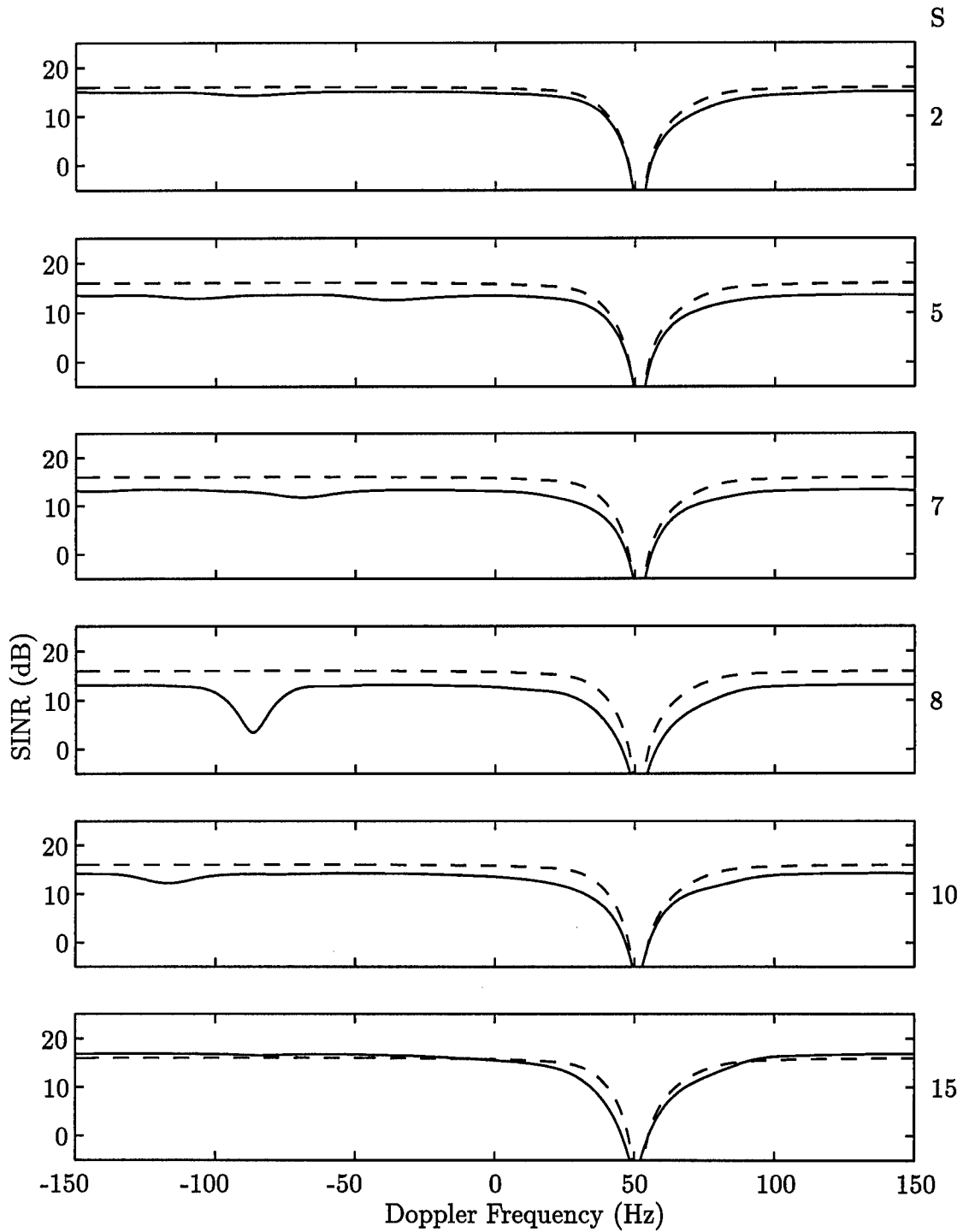


Figure 54 SINR as a function of Doppler frequency for a target at 20° , 100 Hz, scatterer orientation E. The number of scatterers, S , is indicated at the right side of the plot. The dashed line is the SINR with no scatterers.

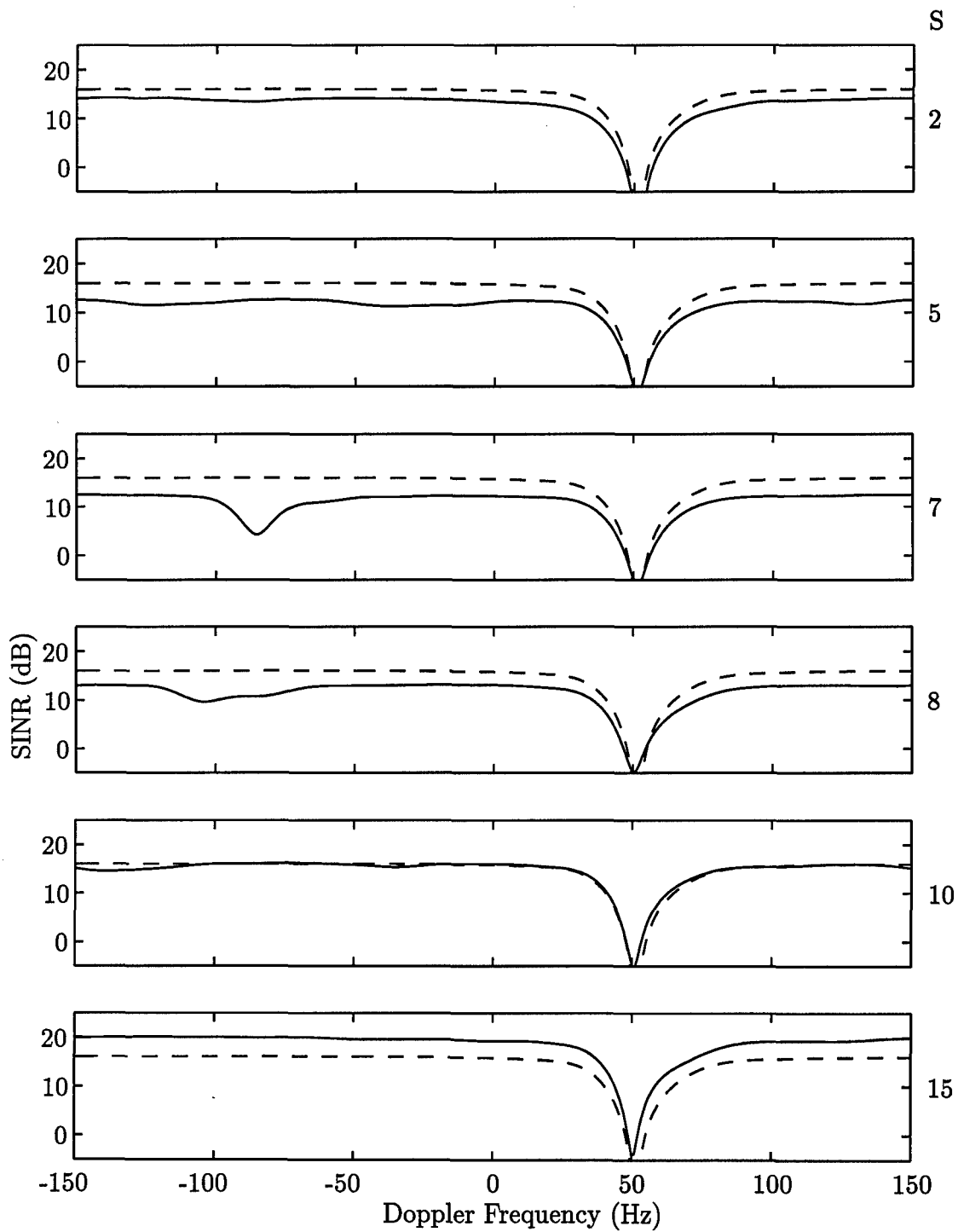


Figure 55 SINR as a function of Doppler frequency for a target at 20° , 100 Hz, scatterer orientation F. The number of scatterers, S , is indicated at the right side of the plot. The dashed line is the SINR with no scatterers.

VI. Conclusions

6.1 Conclusions

This thesis has presented a derivation of space-time adaptive processing in the presence of near-field scatterers. In Chapter 4, we derived an expression for the spatial steering vector of the signal entering the array due to a particular scatterer. Summing this result over all the scattering paths and adding the direct path steering vector gives the steering vector for the combined direct and scattered signals. This total steering vector replaces the direct path steering vector in the computation of the space-time snapshot of the signal, the covariance matrix of the undesired signals, the optimum weight vector, and the adapted pattern and SINR.

The effect of near-field scatterers on the performance of space-time adaptive processing depends on the number and configuration size of the scatterers. The scatterers increase the energy entering the receivers from each signal source. In some cases, the fully adaptive processor is able to suppress the scattered jammer and clutter energy while using the scattered target energy to increase the SINR. When the number of scatterers is small and the spacing between them is more than a half wavelength, the scatterers create grating lobes in the adapted pattern. The grating lobes allow undesired signals to enter the receiver, reducing the SINR by as much as 6 dB in some situations. As the number of scatterers increases, the grating lobes vanish.

Changing the orientation of the scatterers had the most dramatic effect on the shape of the adapted antenna pattern. Arranging the scatterers normal to the array, as in orientations B and C, caused the greatest disruption of the sidelobe pattern, in some cases elevating the sidelobes by 10 dB or more, as seen in Figs. 45 and 46. Although the elevated sidelobes allow additional undesired signals to enter the receiver, the adaptive processor is able to maintain good SINR performance,

experiencing only a 2-3 dB loss for orientation B (Fig. 51) and a achieving a slight gain for orientation C (Fig. 52).

The rank of the clutter covariance matrix when the near-field scatterers are present is significantly higher than without the scatterers. In Section 3.6.2, the return from a clutter patch was assumed to remain constant from pulse to pulse. With the near-field scatterers, this assumption does not hold. The scattered signals entering one element will be different from the scattered signals entering the next element when the array is shifted, as in Fig. 19. The maximum values for the rank for each orientation occurs with between eight and twelve scatterers. Increasing the number of scatterers beyond 5 has relatively little effect on the rank when compared to the increase in rank when the first two scatterers are introduced.

6.2 Suggestions for Future Research

In every case considered in this thesis, the target, jammer, and scatterers were all in the same plane. The effect of placing the scatterers in different arrangements in three dimensions should be studied. The extension of the derivation presented here is straightforward, requiring only the antenna pattern and spatial frequency to be calculated as a function of elevation.

The effects of signals bouncing off multiple scatterers also needs to be investigated. Multiple scattering will probably have the greatest impact at angles approaching $\pm 90^\circ$, since the direct path gain is nearly zero at these angles.

Appendix A. Notational Conventions and Matrix Operations

This Appendix defines the notation conventions which will be used in this paper.

Vectors (defined to be column vectors): lower-case bold letters: $\mathbf{x}, \boldsymbol{\alpha}$.

When the elements of a vector are given explicitly, a semicolon (;) between elements indicates a column vector, and a comma (,) or no punctuation between elements indicates a row vector.

$$\begin{aligned}\text{RowVector } \mathbf{b} &= [a_1, a_2, \dots, a_n] \\ &= [a_1 \ a_2 \ \dots \ a_n]\end{aligned}$$

$$\begin{aligned}\text{ColumnVector } \mathbf{a} &= [a_1; a_2; \dots; a_n] \\ \mathbf{b}^T &= \mathbf{a}\end{aligned}$$

Matrices: upper-case bold letters: $\mathbf{R}, \boldsymbol{\Xi}$.

Element of matrix $\mathbf{A} = a_{k,l}$

Scalars: unbold characters: α, N .

Complex conjugate: $(\cdot)^*$

Transform of a vector or matrix: $(\cdot)^T$

Conjugate Transform: $(\cdot)^H$

$M \times M$ Identity matrix: \mathbf{I}_M

$M \times 1$ vector of ones: $\mathbf{1}_M = [1; 1; \dots; 1]$

Toeplitz matrix: a matrix in which all diagonal elements are equal. The vectors \mathbf{x} and \mathbf{y} represent the first row and first column respectively. (In this example,

$M = N$, but this is not necessary.)

$$\text{Toeplitz}(\mathbf{x}, \mathbf{y}) = \begin{pmatrix} x_1 & x_2 & x_3 & \cdots & x_N \\ y_2 & x_1 & x_2 & \cdots & x_{N-1} \\ y_3 & y_2 & x_1 & \cdots & x_{N-2} \\ \vdots & \vdots & \vdots & & \vdots \\ y_M & y_{M-1} & y_{M-2} & \cdots & x_1 \end{pmatrix}$$

Toeplitz(\mathbf{x}) the same vector is used for the first row and first column, and therefore the resulting matrix is symmetric.

Inner product of \mathbf{x} and \mathbf{y} , each of length M : $z = \mathbf{x}^T \mathbf{y} = \mathbf{x} \cdot \mathbf{y} = a_1 b_1 + a_2 b_2 + \cdots + a_M b_M$.

Outer product of \mathbf{x} and \mathbf{y} of lengths M and N respectively:

$$\mathbf{Z} = \mathbf{xy}^T = \begin{bmatrix} a_1 b_1 & a_1 b_2 & \cdots & a_1 b_N \\ a_2 b_1 & a_2 b_2 & \cdots & a_2 b_N \\ \vdots & \vdots & & \vdots \\ a_M b_1 & a_M b_2 & \cdots & a_M b_N \end{bmatrix}$$

Kronecker Product: for \mathbf{A} ($M \times N$) and \mathbf{B} ($K \times L$). The resulting matrix \mathbf{Z} is $MK \times NL$.

$$\mathbf{Z} = \mathbf{A} \otimes \mathbf{B} = \begin{bmatrix} a_{1,1} \mathbf{B} & a_{1,2} \mathbf{B} & \cdots & a_{1,N} \mathbf{B} \\ a_{2,1} \mathbf{B} & a_{2,2} \mathbf{B} & \cdots & a_{2,N} \mathbf{B} \\ \vdots & \vdots & & \vdots \\ a_{M,1} \mathbf{B} & a_{M,2} \mathbf{B} & \cdots & a_{M,N} \mathbf{B} \end{bmatrix}$$

Hadamard Product: A and B must both be $M \times N$

$$\mathbf{Z} = \mathbf{A} \odot \mathbf{B} = \begin{bmatrix} a_{1,1}b_{1,1} & a_{1,2}b_{1,2} & \cdots & a_{1,N}b_{1,N} \\ a_{2,1}b_{2,1} & a_{2,2}b_{2,2} & \cdots & a_{2,N}b_{2,N} \\ \vdots & \vdots & & \vdots \\ a_{M,1}b_{M,1} & a_{M,2}b_{M,2} & \cdots & a_{M,N}b_{M,N} \end{bmatrix}$$

Vandermonde Matrix: given an $M \times N$, each x_m will be unique.

$$\begin{bmatrix} 1 & x_1 & x_1^2 & \cdots & x_1^{N-1} \\ 1 & x_2 & x_2^2 & \cdots & x_2^{N-1} \\ \vdots & \vdots & \vdots & & \vdots \\ 1 & x_M & x_M^2 & \cdots & x_M^{N-1} \end{bmatrix}$$

Appendix B. Supplemental Figures

The following figures show the full adapted angle-Doppler pattern for a target at 20° , 100 Hz, and each scatterer orientation.

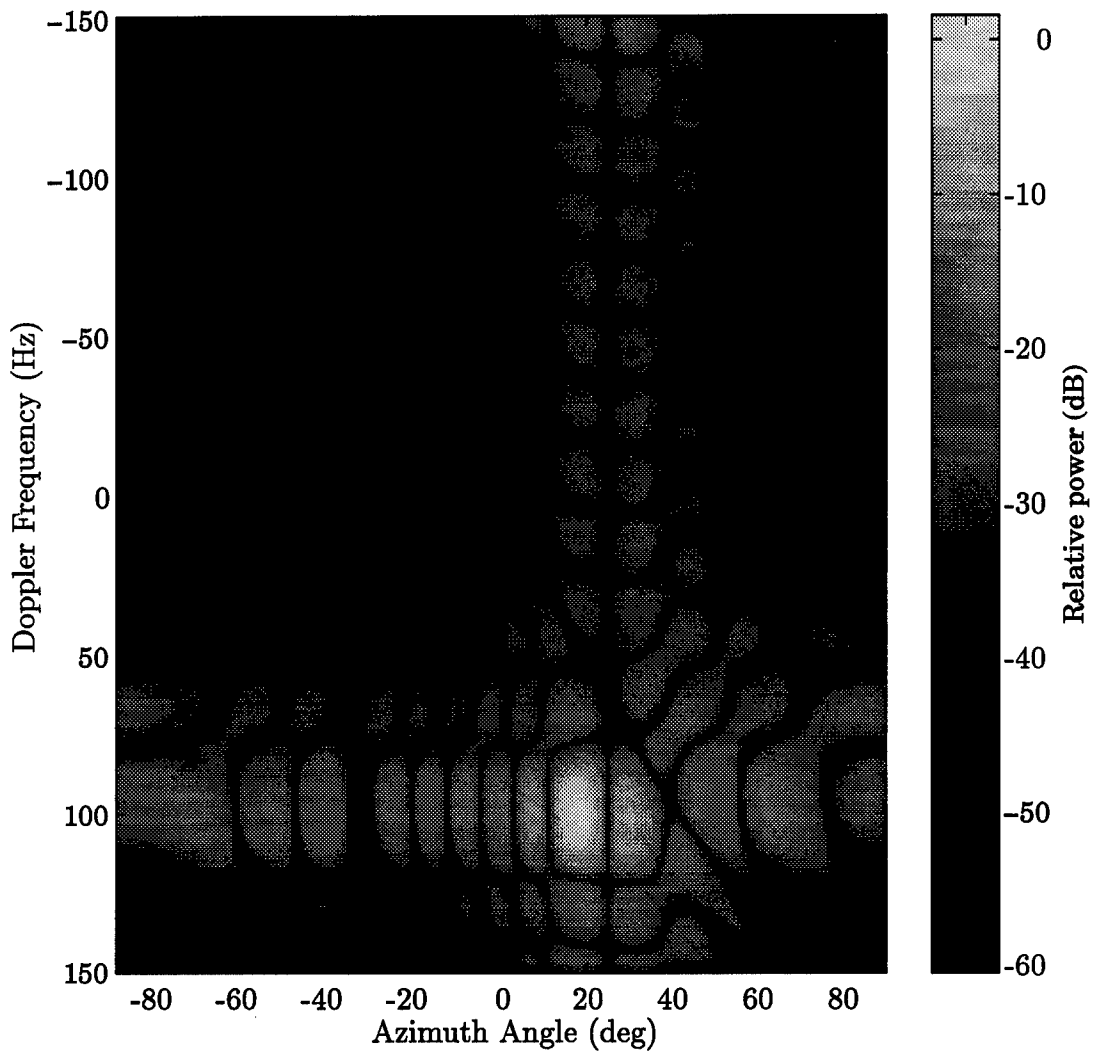


Figure 56 Angle-Doppler pattern for a target at 20°, 100 Hz, with no scatterers.

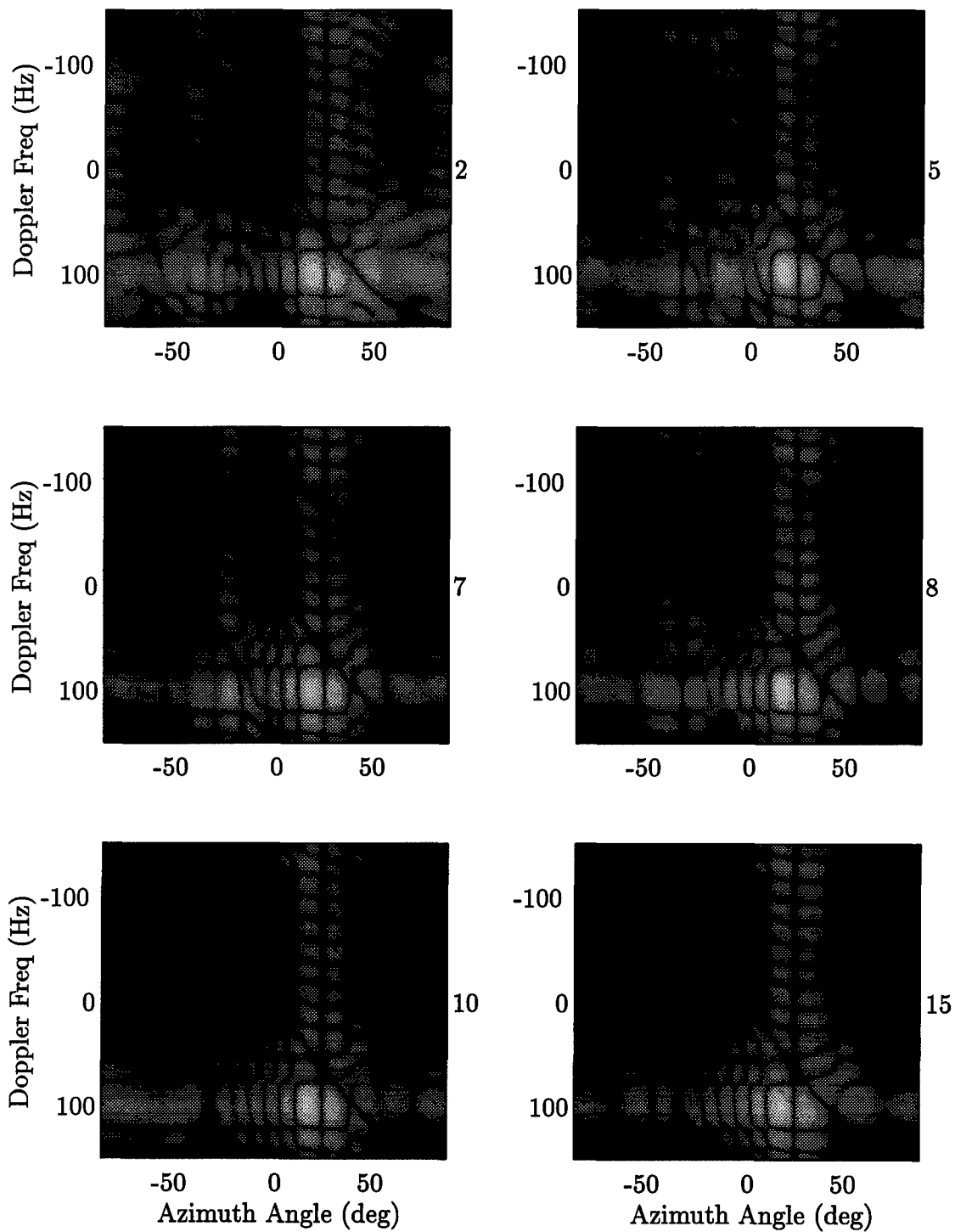


Figure 57 Angle-Doppler pattern for a target at 20° , 100 Hz, with scatterers with $\sigma_s = 0.5 \text{ m}^2$ placed in orientation A. The number of scatterers is indicated to the right of each figure.

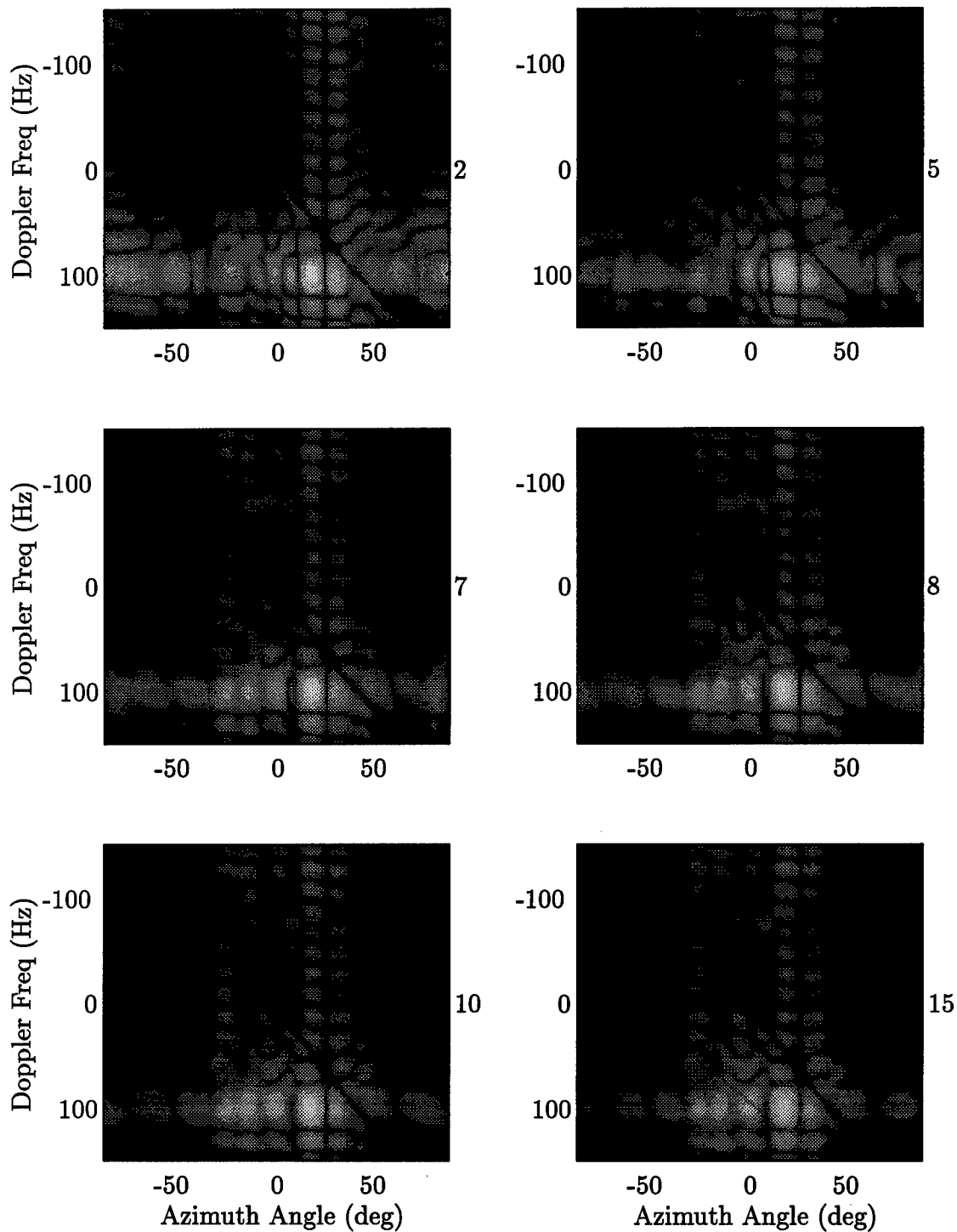


Figure 58 Angle-Doppler pattern for a target at 20° , 100 Hz, with scatterers with $\sigma_s = 0.5 \text{ m}^2$ placed in orientation B. The number of scatterers is indicated to the right of each figure.

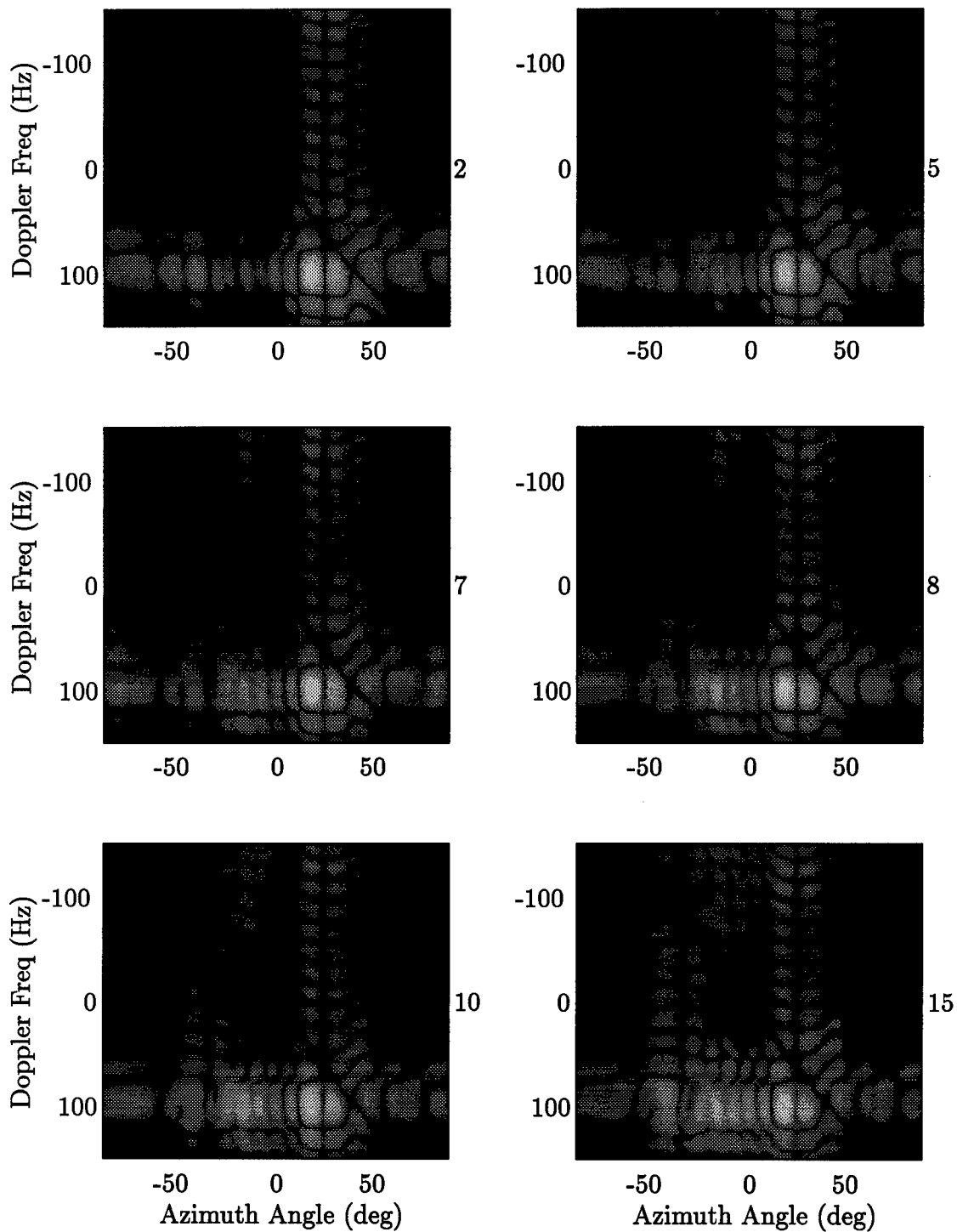


Figure 59 Angle-Doppler pattern for a target at 20° , 100 Hz, with scatterers with $\sigma_s = 0.5 \text{ m}^2$ placed in orientation C. The number of scatterers is indicated to the right of each figure.

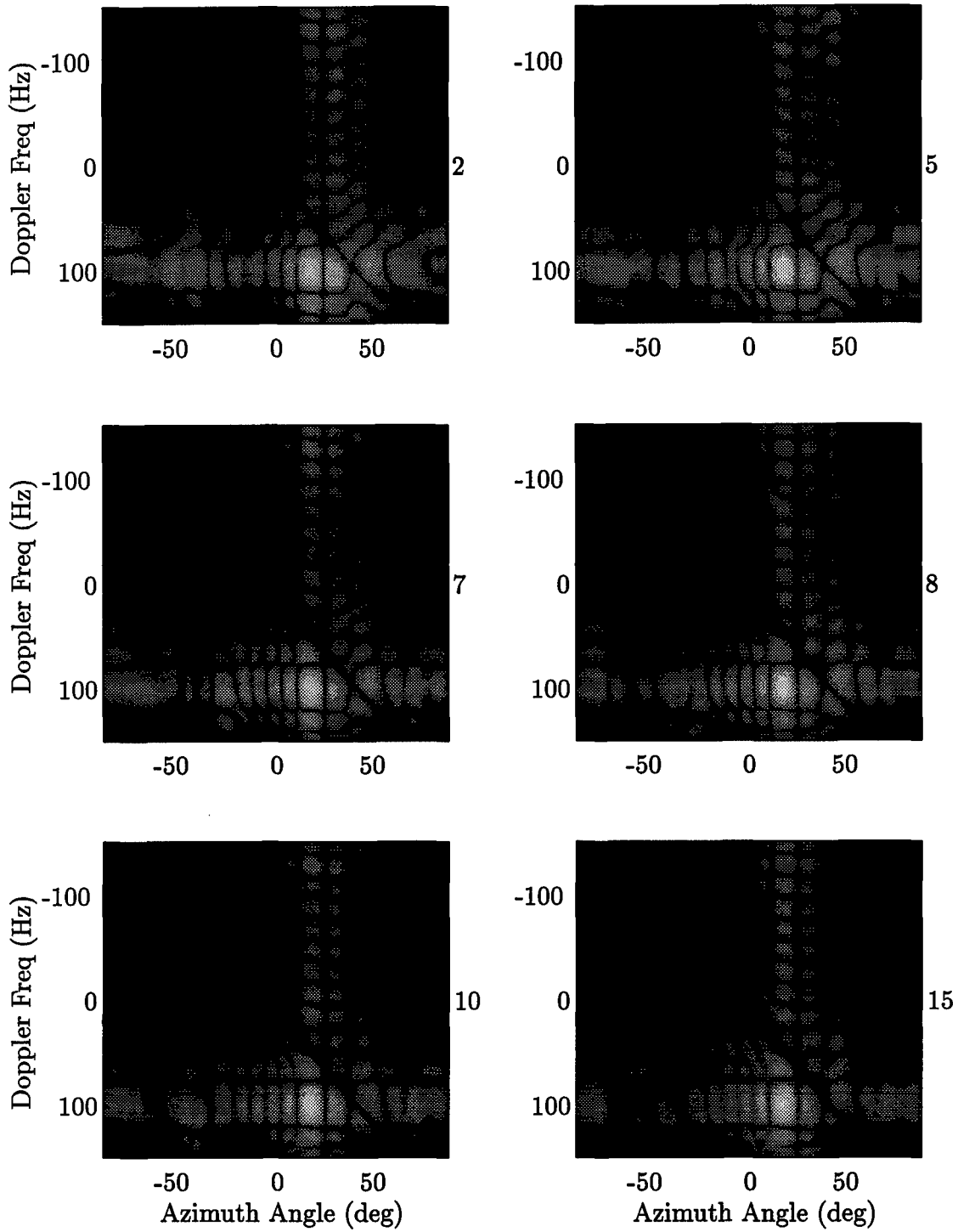


Figure 60 Angle-Doppler pattern for a target at 20° , 100 Hz, with scatterers with $\sigma_s = 0.5 \text{ m}^2$ placed in orientation D. The number of scatterers is indicated to the right of each figure.

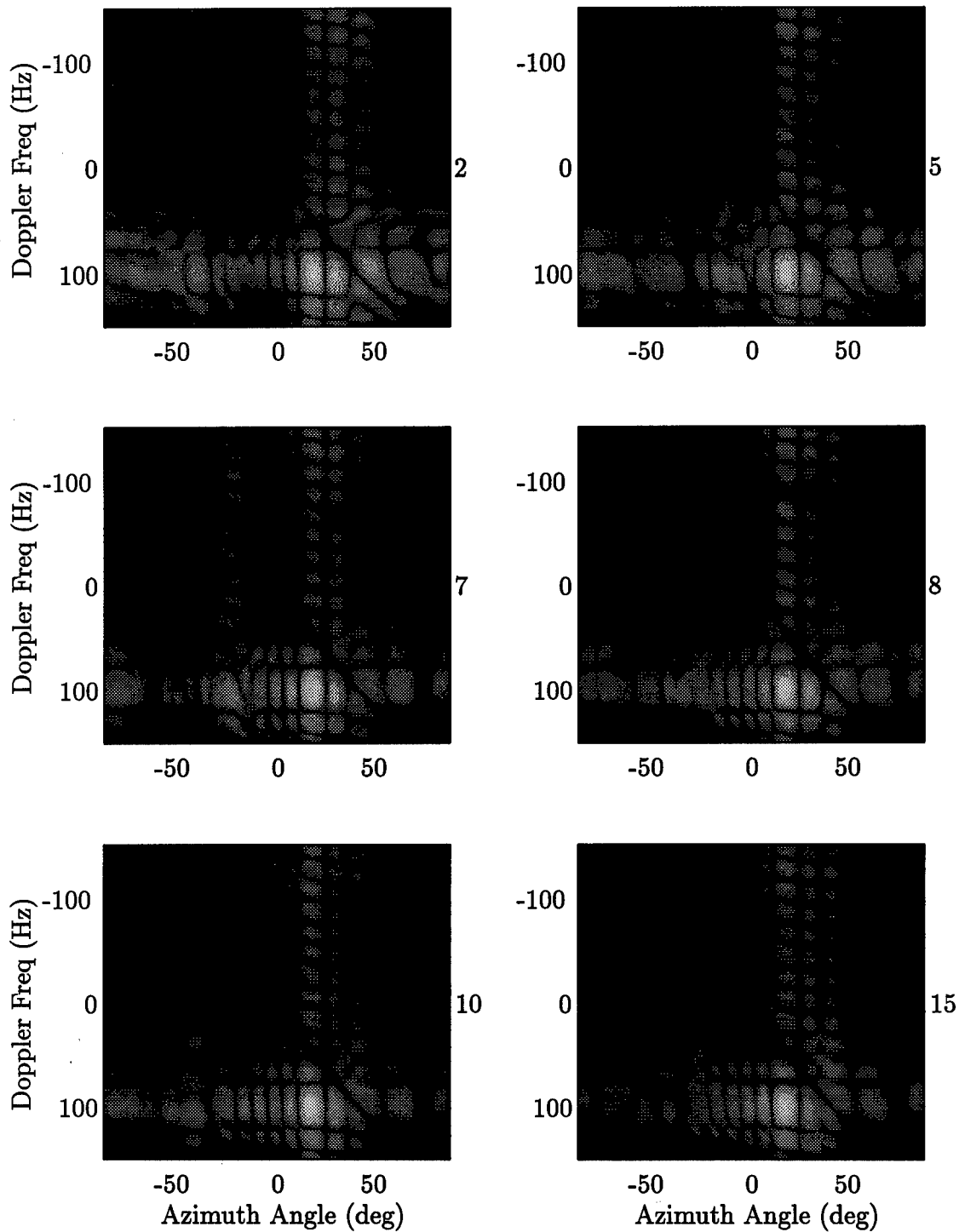


Figure 61 Angle-Doppler pattern for a target at 20°, 100 Hz, with scatterers with $\sigma_s = 0.5 \text{ m}^2$ placed in orientation E. The number of scatterers is indicated to the right of each figure.

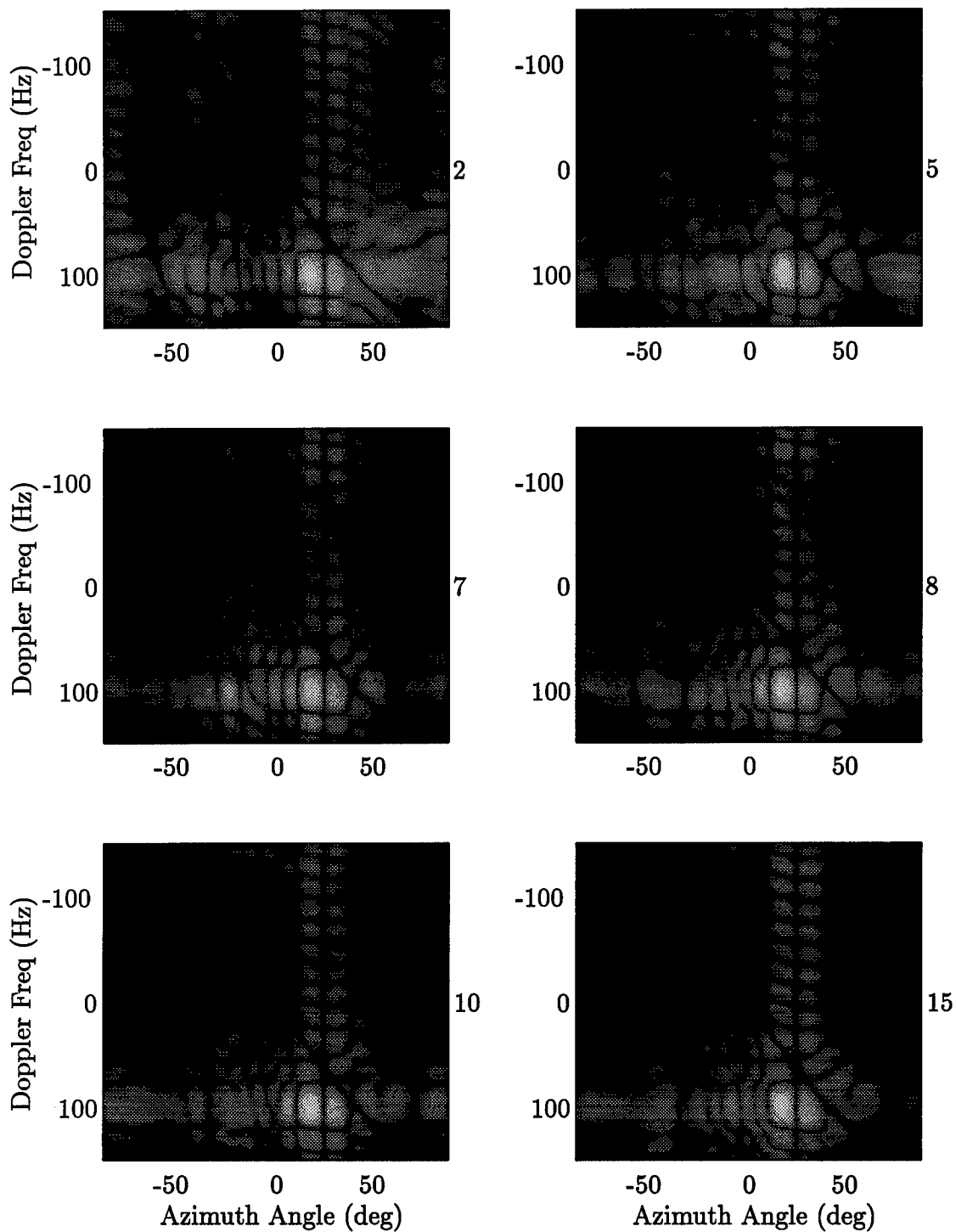


Figure 62 Angle-Doppler pattern for a target at 20°, 100 Hz, with scatterers with $\sigma_s = 0.5 \text{ m}^2$ placed in orientation F. The number of scatterers is indicated to the right of each figure.

Bibliography

1. Applebaum, Sidney P. "Adaptive Arrays," *IEEE Transactions on Antennas and Propagation*, AP-24(5):585 (September 1976).
2. Balanis, Constantine A. *Antenna Theory*. John Wiley & Sons, Inc., 1997.
3. Barile, Edward C., et al. "Some Limitations on the Effectiveness of Airborne Adaptive Radar," *IEEE Transactions on Aerospace and Electronic Systems*, 28(4):1015-1031 (October 1992).
4. Barile, Edward C., et al. "Adaptive Antenna Space-Time Processing Techniques to Suppress Platform Scattered Clutter for Airborne Radar," *IEEE Transactions on Aerospace and Electronic Systems*, 31(1):382-389 (January 1995).
5. Brennan, Lawrence E. and Irving S. Reed. "Theory of Adaptive Radar," *IEEE Transactions on Aerospace and Electronic Systems*, AES-9(4):607-615 (March 1973).
6. Dudgeon, Dan E. and Russell M. Mersereau. *Multidimensional Digital Signal Processing*. Prentice Hall, Inc., 1984.
7. Skolnik, Merrill I. *Introduction to Radar Systems* (Second Edition). McGraw-Hill, 1980.
8. Ward, James. *Space-Time Adaptive Processing for Airborne Radar*. Technical Report ESC-TR-94-109, Advanced Research Projects Agency, December 1994 (AD-A293032).
9. Widrow, Bernard., et al. "Adaptive Antenna Systems," *Proceedings of the IEEE*, 55 (December 1967).
10. Yu, C. L., et al. "Volumetric Pattern Analysis of Airborne Antennas," *IEEE Transactions on Antennas and Propagation*, AP-26(2):636-641 (September 1978).

Vita

Jonathan W. Fitton was born in Lancaster, PA on January 13, 1969. He received his B.S.E.E degree from Lehigh University, Bethlehem, PA and was commissioned as a Second Lieutenant in the U.S. Air Force in June, 1991. From 1992 to 1996 he worked in the Air-to-Air Missile Test Flight at Eglin Air Force Base, Fort Walton Beach, FL. Since 1996, he has been pursuing his M.S.E.E. degree at the Air Force Institute of Technology, Wright-Patterson AFB, Dayton, OH. In January, 1998, he will begin working at the Air Force Information Warfare Center, Kelly AFB, San Antonio, TX.

Capt. Fitton is a member of Eta Kappa Nu.

Permanent address: 25 Vista Rd.
Wyomissing, PA 19610

REPORT DOCUMENTATION PAGE

Form Approved
OMB No. 0704-0188

Public reporting burden for this collection of information is estimated to average 1 hour per response, including the time for reviewing instructions, searching existing data sources, gathering and maintaining the data needed, and completing and reviewing the collection of information. Send comments regarding this burden estimate or any other aspect of this collection of information, including suggestions for reducing this burden, to Washington Headquarters Services, Directorate for Information Operations and Reports, 1215 Jefferson Davis Highway, Suite 1204, Arlington, VA 22202-4302, and to the Office of Management and Budget, Paperwork Reduction Project (0704-0188), Washington, DC 20503.

1. AGENCY USE ONLY (Leave blank)		2. REPORT DATE December 1997	3. REPORT TYPE AND DATES COVERED Master's Thesis	
4. TITLE AND SUBTITLE EFFECTS OF NEAR-FIELD SCATTERERS ON SPACE-TIME ADAPTIVE PROCESSING			5. FUNDING NUMBERS	
6. AUTHOR(S) Jonathan W. Fitton				
7. PERFORMING ORGANIZATION NAME(S) AND ADDRESS(ES) Air Force Institute of Technology, WPAFB OH 45433-6583				
9. SPONSORING / MONITORING AGENCY NAME(S) AND ADDRESS(ES) Capt. William L. Melvin, Jr. USAF Rome Labs/OCSS Signal Processing Branch 26 Electronics Pkwy. Rome, NY 13441-4514			8. PERFORMING ORGANIZATION REPORT NUMBER AFIT/GE/ENG/97D-12	
10. SPONSORING / MONITORING AGENCY REPORT NUMBER				
11. SUPPLEMENTARY NOTES				
12a. DISTRIBUTION / AVAILABILITY STATEMENT Distribution Unlimited			12b. DISTRIBUTION CODE	
13. ABSTRACT (Maximum 200 words) Near-field scatterers, such as the wing of an airplane, can affect the ability of the processor to null out clutter and jammer signals. The target, clutter, and jammer signals will reflect off the near-field scatterers into the array and appear to be coming from a direction different from their true sources. This thesis develops a theoretical model for the direct path and scattered path signals from the target, clutter, and jamming signals. The optimum weight vector, normally computed using the steering vector to the target and the covariance matrix of the undesired signals, must now include the effects of the scattered signals as well. This thesis shows that the space-time steering vector for the scattered signal can be written in a form similar to the direct path signal. The total space-time steering vector of a signal is the sum of the direct path and scattered path steering vectors associated with that signal.				
14. SUBJECT TERMS Space-Time Adaptive Processing, STAP, Near-field Scatterers, Adaptive Array Processing			15. NUMBER OF PAGES 129	
			16. PRICE CODE	
17. SECURITY CLASSIFICATION OF REPORT UNCLASSIFIED	18. SECURITY CLASSIFICATION OF THIS PAGE UNCLASSIFIED	19. SECURITY CLASSIFICATION OF ABSTRACT UNCLASSIFIED	20. LIMITATION OF ABSTRACT UL	